Proceedings of the Tenth Asian Congress of Fluid Mechanics
17-21 May 2004, Peradenia, Sri Lanka

VORTEX AND STRUCTURE OF TURBULENT BOUNDARY LAYER

Y. Kobashi
Hokkaido Institute of Technology, Teine, Sapporo, Japan

M. Hayakawa
Dept. Eng., Hokkaido University, N13 W8 Sapporo, Japan

ABSTRACT: Based on the idea that turbulence is the flow phenomenon caused by the movement of vortices, the structures of turbulent boundary layer are discussed. The circulation is the most important factor to characterize the flow structures of inner and outer layers. The large-scale motions such as the bulge in the outer layer and the burst in the inner layer can be explained by the mutual interactions between vortices.

1 INTRODUCTION

The real fluid is known to bear the velocity gradient by producing vorticity inside the fluid itself. This is the viscosity. If we call the fluid elements which carry vorticity as the eddies, their effects are expressed by the circulation $p r^2 w$ which is equivalent to kinematic viscosity. Here r is the radius of the fluid element of a cylindrical shape which contains vorticity w. This fluid element forms the nucleus or the core of eddy to sustain the velocity gradient by its rotation.

The vortex is the assemblage of eddies, which has enough energy and power to govern the flow patterns. The velocity distributions and the unique coherency of the boundary layer turbulence can be explained by the mutual interactions between vortices.

2 TURBULENCE AND VORTEX

In the laminar flow, the viscosity m is defined by

$$m = r\, v = r\, p\, r^2 w \qquad (1)$$

where n is the kinematic viscosity.

Because the vorticity is nothing but the velocity gradient du/dy, the shear stress t is given by

$$t = mw = r\, p\, r^2 w^2 \qquad (2)$$

Eq.(1) shows that the size of the core increases according to the decrease of the velocity gradient because the viscosity of fluid is constant under given environmental conditions.

Eq.(2) shows that the viscous stress increases proportionally to the velocity gradient, but this trend ceases to be applicable if t exceeds some critical value t_{cri} intrinsic to the flow condition, probably its ratio to the mean flow energy, and the vortex nuclei which contain energy per unit mass

$$p\, r^2 w^2 = t_{\mathrm{cri}} / r \qquad (3)$$

are released into the flow. These nuclei take the surrounding fluid inside and grow in size with keeping the same energy. This is the birth of turbulence.

Because the interacting activity between vortices or the vortex potential is determined by their rotary moment or the circulation

$$p r^2 w \sim (t_{\mathrm{cri}} / r) / w \qquad (4)$$

the vortices which pass through the region of smaller velocity gradient interact more powerfully. The integration of vortices near the outer edge of the boundary layer certifies the manifest mentioned above.

Usually turbulence is accepted as the irregular motions of the flow. The idea to treat the turbulent flow as the ensemble of various waves is most popular, and the concept of frequency or spectrum of turbulence has been derived from this approach. This approach is favorable for the mathematical description of turbulence especially of its outbreak (transition) from laminar flow. The numerical calculus by computer and the mathematical approach from a statistical point of view also seem to be attractive to describe the turbulence phenomena.

But for those who want to explore the flow phenomena as the substantial motion of the fluid, these are not so welcome.

To grasp the turbulent motion of the fluid substance, it is necessary to follow the flow pattern caused by the movement of fluid elements in the Lagrangian way. This can be performed by representing the vorticity-containing fluid elements by the Rankin vortices which are composed of the rotating core and the surrounding circulating fluid. When multiple vortices exist, they interact mutually and move out from their own courses. Their paths can be determined decisively, but if the number of vortices becomes large their motions become very complicated and look to be very random. This is our turbulence.

3 VELOCITY DISTRIBUTIONS OF TURBULENT BOUNDARY LAYER

The turbulent boundary layers are known to be composed of two layers, the outer layer and the inner layer. For the inner layer, the logarithmic law velocity distribution has been established. It assumes that the wall shear stress prevails through the inner layer. As to the outer layer velocity distribution, many theories are offered, among which "The Law of the Wake" proposed by Coles(1956)[1] is the most popular. It divides the layer into two parts, the inner layer dependent part and the residual part, and treats the latter as the wake type flow. But we are rather suspicious to this approach because the outer layer turbulence is strong enough to destroy the wall effects and accepts the free shear layer type flow pattern to prevail whole through the boundary layer except a narrow transient region adjacent to the wall layer. The power law velocity distribution has been found to be applied with reasonable accuracy[2]. The inner layer is the region where the vortices produced at the wall prevail and the effects of the wall predominate, from which the logarithmic velocity distribution was derived.

In Fig 1a three cases of velocity distributions picked up from more than forty experiments are shown, in which the junction between the inner and outer layer is marked by YM. From the figure we can accept the validity of the power law and log law for a wide range of Reynolds number. Both the power index 'Nw' and the friction velocity 'u_t' which characterizes the log law distribution decrease with Reynolds number as are shown in Fig 1b. It shows that the velocity distributions in the outer layer Y>YM become more and more flat suggesting the decrease of turbulent energy production.

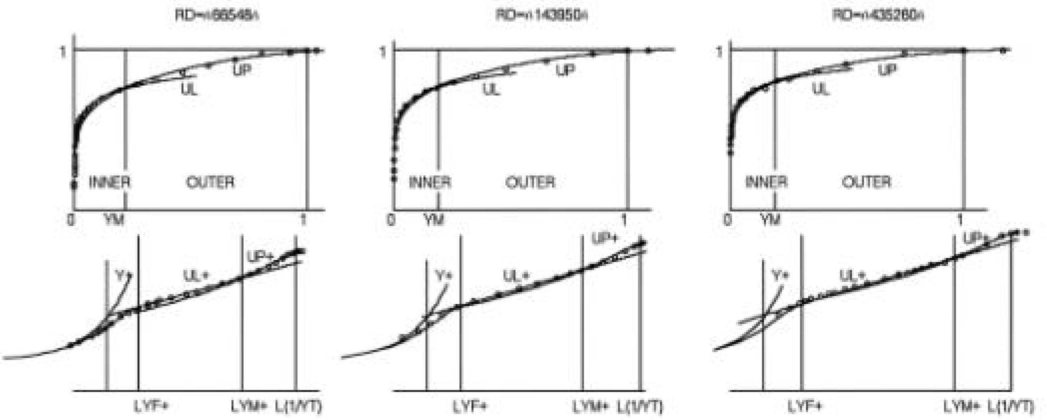

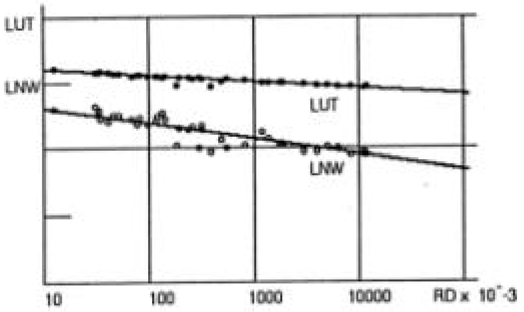

Fig 1a Velocity distributions
UL: log law profile
Up: power law profile

Fig 1b Characteristic quantities
u_τ : friction velocity
NW: power index

If turbulence is the flow phenomenon caused by vortex motions, the velocity distributions of the turbulent boundary layer must be derived from the vortex mechanism.

Outer Layer Velocity Distribution

Because the outer layer is covered by free shear layer type turbulence, we employed three rows of vortices to relate them to the velocity distributions[3]. The reason we employed three rows of turbulent vortices is because a single vortex, which probably appears at the beginning, undergoes stretching due to the velocity difference and can no longer sustain the group of vorticity-containing particles and breaks down into three. The calculated distributions are satisfactory as shown in Fig 2.

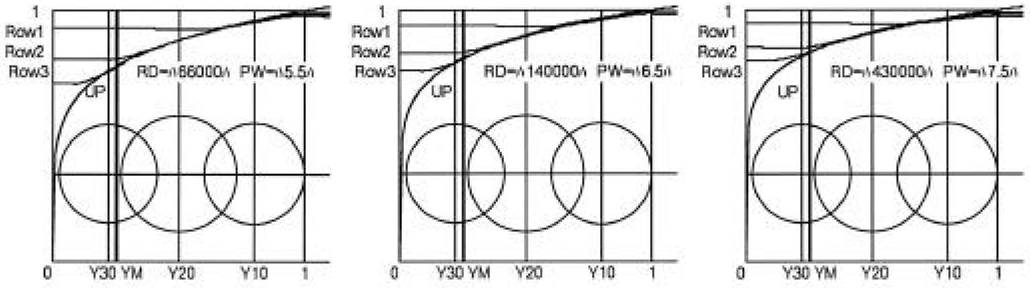

Fig 2: Velocity distribution of vortex rows

Inner Layer Velocity Distribution

The inner layer is the region where the vortices produced at the wall prevail and the effects of the wall predominate. These vortices are supposed to increase its size linearly with the distance from the wall y keeping the same intensity r^2w^2. Using the relations $w = du/dy$ and $r \quad y$, we can derive the following equation

$$du/dy \sim \quad u_t / y \qquad (5)$$

where $$u_t = (t_{wall} / r)^{1/2} \qquad (6)$$

is the friction velocity. Eq.(5) leads to the logarithmic velocity distribution with 'u_t' as the characteristic constant.

The decrease of 'u_t' shown in Fig 1b suggests the decrease of the production of turbulent energy with Reynolds number. The same tendency is found in the boundary layer of the accelerated flows in which the relaminarization problem is the most essential[4].

4 STRUCTURE OF BOUNDARY LAYER TURBULENCE

The boundary layer turbulence can be classified into two types, the free shear layer type and the wall layer type. Because the turbulence is induced by the movement of the vorticity-containing particles, its flow phenomena are dependent on the vortical power or circulation of the particles (Eq. 3). If it is large, the particles become active and turbulence is rough, but if not, turbulence is quiet and ordered. The free shear layer turbulence is the former type and the wall turbulence is the latter. The active particles interact with the neighboring particles to cause large-scale turbulence and give birth the turbulent vortices or the coherent structures.

Outer Layer Turbulence

The outer layer turbulence is the free shear layer type. It is composed of rough vortices, which have a tendency to make groups called as the coherent or the bulge structures. In our turbulence model, three rows of turbulent vortices were employed to fit the velocity distribution accurately. These rows interact one after another when they move downwards and exhibit periodical or intermittent patterns. The mean period of the coherent structures, given by $TUe/d \quad 5$, is the interval of overlapping between row 1 and row 2 vortices. The schematic drawing of the overlapping process is given in Fig.3.

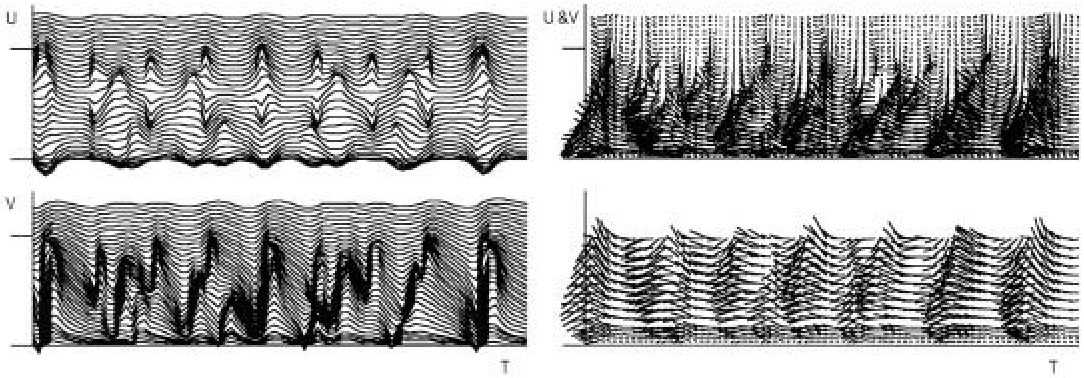

Fig 3: Time dependent velocity components and flow patterns

Inner Layer Turbulence (Wall Turbulence)

The inner layer is covered by vortices which are borne at the wall. They grow linearly in size with the distance from the wall keeping the same strength. Because of the steep velocity gradient their size is still small, and therefore their power or the interacting activity is weak and the resulting turbulence is calm and quiet.

The burst structures which appear in the basically quiet inner layer and are known to be the source of turbulent energy of the whole boundary layer, are supposed to be brought by the interactions between vortex groups of the outer layer, probably of row 2 and row 3.

The burst has a three dimensional structure which cannot be explained by the two-dimensional vortex analysis. The Goertler type hairpin vortex caused by the pressure gradient near the wall may be helpful to understand this three-dimensionality.

Energy Cycle of Turbulent Boundary Layer

The energy of the outer layer is supplied from the burst, which is promoted by the interaction between the vortices of the outer layer. This process makes the energy cycle of the turbulent boundary layer from outer layer to inner layer and from inner layer to outer layer. If the turbulence of the outer layer decreases, the promotion of the burst reduces, which in turn pushes the decrease of the energy supply to the outer layer. The relaminarization of the accelerated flow boundary layer is the model of this energy cycle. This may give the answer to the question about the problem “what happens in the uniform flow boundary layer at infinitely high Reynolds number ?”.

5 CONCLUSIONS

Based on the idea that turbulence is the flow phenomena associated with the movement of vortices, the structure of the turbulent boundary layer has been discussed. These vortices are characterized by their strength r (r^2w^2) and power r (r^2w), the former of which corresponds to the turbulent intensity, and the latter to the turbulent viscosity.

The difference between the outer layer turbulence and inner layer turbulence is brought by the difference of their power. The former is very active in the sense that the fluid particles crowd to make groups, but the latter is very calm and makes ordered flow patterns. Both are tied up through the burst structures which appear in the inner layer periodically and supply energy to keep whole layer turbulent. The appearance of the burst structure in the inner layer which otherwise quiet is brought by the interactions between the outer layer vortices. This feed back system seems to cease when Reynolds number or when the streamwise pressure gradient (negative) exceeds some critical value.

References:

[1] Coles,D. : The Law of the Wake in the Turbulent Boundary Layer; J.Fluid Mech 1, 1956.

[2] Kobashi,Y and Hayakawa,M.: Structure of a Turbulent Boundary Layer and its Dependence on Reynolds Number; 8th ACFM, 1999.

[3] Kobashi,Y. and Hayakawa,M.: The Vortex Row Model of a Turbulent Boundary Layer; 13th Australasian FMC, 1998.

[4] Kobashi,Y. and Hayakawa,M.: Relaminarization Mechanism of Turbulent Boundary Layer in Accelerated Flow; 9th ACFM, 2001.

Proceeding of Tenth Asian Congress of Fluid Mechanics
17-21 May 2004, Peradeniya, Sri Lanka

EXPERIMENTAL INVESTIGATION ON WAKE BEHIND A SINUSOIDAL CYLINDER

Anh-Tuan Nguyen and Sang-Joon Lee

Dept. of Mechanical Engineering

Pohang University of Science and Technology, Pohang, 790-784, Korea

ABSTRACT: The near wake behind a sinusoidal cylinder has been investigated experimentally using hot-wire anemometer and flow visualization. The sinusoidal cylinder with $\lambda/D = 2$ gives the maximum 22% drag reduction at $Re = 10^4$. The wake structure shows periodic variation along the spanwise direction. The near wake in saddle plane has wider wake width and larger velocity deficit, compared with the nodal plane. The elongated vortex formation region of sinusoidal cylinder seems to be related with drag reduction. The visualized flow shows the 3-D vortex structure in the near wake behind the sinusoidal cylinders.

1. INTRODUCTION

Vortex shedding from a bluff body has been a challenging area for fluid dynamic researches. For example, the large drag forces and possible vortex-induced vibration of pipes and long slender tubular should be considered in design of offshore structures. There are several passive flow control techniques to reduce drag force and suppress regular vortex shedding. These techniques employ some forms of three-dimensional geometric disturbance to the nominally 2-D bluff body, for instance, helical strakes, grooves, ribbons, bump …etc.

Tombazis and Bearman (1993, 1997)[4,8] obtained 34% maximum drag reduction by introducing a blunt-based model with wavy trailing edge at Reynolds number of 40,000. They mentioned that the introduction of a spanwise waviness at the trailing edge could fix the position of vortex dislocation, resulting in drag reduction. Bearman and Owen (1998)[3] investigated the influence of spanwise waviness on flow around a rectangular cylinder with sinusoidal shape both in front and rear face. They obtained about 30% drag reduction, compared with equivalent straight simple body and found the optimal ratio of peak-to-peak wave height divided by wavelength is between 0.06 and 0.09. Ahmed (1993)[1] investigated experimentally the wake behind a wavy cylinder having cross-sectional variation along the span. He focused on the topology of boundary separation and turbulence structure. However, he did not mentioned about drag reduction and suppression of vibration. Recently Lam et al. (2003)[7] investigated the near wake of a wavy cylinder using LDV measurement and preliminary numerical simulation. The wavy geometry played an important role on vortex formation length variation and drag reduction and vortex shedding suppression.

In this study, we investigated the effects of sinusoidal variation of cylinder cross-section on drag reduction and modification of wake structure as a passive flow control method. Two models of sinusoidal cylinders with the mean diameter $D_m = 20$mm and $\lambda/D = 1$ and 2 were tested. The mean velocity and turbulence intensity profiles in the near wake behind the wavy cylinders were measured by using a hot-wire anemometer. In addition, flow structure around the cylinders was visualized using the particle-tracing method and the smoke-wire technique. The results were compared with those for a smooth circular cylinder having the same equivalent diameter $D = D_m$.

2. EXPERIMENTAL APPARATUS AND METHOD

2.1 Experimental model

One circular cylinder and two sinusoidal cylinders were tested in a wind tunnel. The coordinate and terminology used for the sinusoidal cylinder are shown in Fig 1. The axial location of maximum diameter is termed "geometric node" and that of minimum diameter is termed "geometric saddle". The geometry of the sinusoidal cylinder can be described by the following equation:

$$D = D_m + 2W\cos(2\pi y/\lambda) \qquad (1)$$

$$\frac{dD(y)}{dy} = -\frac{4W\pi}{\lambda}\sin\left(\frac{2\pi y}{\lambda}\right) \qquad (2)$$

where D is the local diameter of sinusoidal cylinder, D_m = 20mm is the mean diameter of sinusoidal cylinder. In this study, two sinusoidal cylinders having different wave lengths of λ = D and 2D have the same wave height W = 4m. The wave steepness (W/λ) plays important role in finding the optimal shape of sinusoidal cylinder, especially in computational analysis[2].

2.2 Experimental methods

Drag force, mean velocity and turbulence intensity profile were measured in a closed-return type subsonic wind tunnel with a test section of 0.72 m x 0.60 m. The free stream turbulence intensity is less than 0.06 % at U_0 = 10m/s. The flow structures around the cylinders were measured at Reynolds numbers which based on D_m Re = 5.3×10^3 and Re = 2.1×10^4. Wake velocity profiles were measured using an I-type hot-wire probe (DANTEC 55P11) and Pitot tube. Hot-wire probe was traversed using a 3-D traverse system with an accuracy of 0.01 mm over the range z/D = –3 ~ 3 with an interval of Δz =0.15D. The aerodynamic forces were measured using a 3-component load-cell (Nissho LMC-3502). The load-cell was connected to a high-gain DC strain amplifier (DSA-100). The output signals were digitized with a DT2838 A/D converter. The drag coefficient C_D was calculated by dividing the drag force with the dynamics pressure based on the effective frontal area A and free stream velocity U_o:

$$C_D = \frac{2\times Drag}{\rho {U_0}^2 A} \qquad (3)$$

The effective frontal area A shape of sinusoidal cylinders was the same as that of the smooth cylinder.

Flow visualization tests were performed in a water channel at various Reynolds numbers in order to observe flow patterns of wake behind the sinusoidal cylinders. The particle tracing method was performed in a circulating water channel with a test section of 0.30 m x 0.25 m. Poly-vinyl-chloride particles with an average diameter of 200μm were used as tracer particles. The particles were illuminated by a thin cold light-sheet supplied from a 150W halogen lamp. Two-dimensional slices of the wake behind the nodal, saddle and middle planes were visualized. In order to see the 3-D structure of near wake behind the sinusoidal surface geometry, the top views were also visualized. All flow visualization tests using particle tracing method were carried out at Re = 3000 and 10,000.

3. EXPERIMENTAL RESULTS AND DISCUSSTION

3.1 Quantitative analyze

Total drag coefficients of two sinusoidal cylinders (λ/D = 1, 2) and one smooth circular cylinder are shown in Fig. 2. The maximum drag reduction is about 22% at λ/D = 2 and Re = 10^4. It is interesting to note that the drag reduction of model 1 is lager compared with model 2 and smooth cylinder. It may be attributed to the modification of flow structure due to three-dimensional geometry of experimental models. How does it make such change? For this, we investigated flow structure behind the sinusoidal cylinder, especially the modification of the wake structure.

Fig. 3 shows variation of the mean streamwise velocity profiles measured at the downstream locations X/D = 4, 6 and 8 for the free stream velocity of U_0 = 4 m/s (Re = 5333). The location of X/D = 4 is just outside of the vortex formation region which was predicted about 3 times of diameter for the case smooth cylinder [5]. Because the near wake shows periodic flow pattern along the span of the sinusoidal cylinders, velocity measurements were preformed for one period of the model. The mean streamwise velocity profiles show a larger velocity deficit in the saddle plane, compared with that at other measurement planes. As the flow goes downstream, variation of the mean streamwise velocity between different spanwise locations (Y = 0 mm, 10 mm and 20 mm) is decreased and smaller than that of smooth cylinder. At further downstream location, the velocity deficit is decreased and the wake width variation is also reduced. This implies that the smooth cylinder causes more momentum loss than the sinusoidal cylinder at further downstream. From this we can conjecture that vortex shedding in the saddle plane entrains larger amount of inviscid fluid from the outer free stream, compared with that in the nodal plane. These results explain why the vortex formation length and the drag coefficient of two models are different.

The turbulence intensity distributions of streamwise velocity component measured along the wake centerline are shown in Fig. 4. Measurements were preformed at two Reynolds numbers, Re = 5333 and Re = 21600. Along the spanwise direction, the peak location of streamwise turbulence intensity shifts downstream. In addition, the turbulence intensity decreases with the increase of Re. There are several definitions of the vortex formation region. For example, Bloor (1963) [5] defined the end of the vortex formation region as the location after which oscillating wake characteristics are observed. Gerrad (1966)[6] determined the end of vortex formation region at which fluid from outside of the wake first cross the wake axis. The vortex formation region is influenced by two vortices, one from the upper side of the cylinder and the other from the lower side. Therefore, at the end of the vortex formation region, the velocity fluctuations, i.e. turbulence intensity, have a maximum value at the vortex shedding frequency. In this study, we measured the length of the vortex formation region by measuring streamwise turbulence intensity along the wake centerline with an I-type hot-wire probe. The lengths of the vortex formation region are summarized in Table 1.

Table. 1 Vortex formation length L_f

Re	**Circular cylinder**	**Sinusoidal Cylinder (λ/D = 2)**			**Sinusoidal Cylinder (λ/D = 1)**		
		Node	**Middle**	**Saddle**	**Node**	**Middle**	**Saddle**
		Y = 0 mm	Y= 10 mm	Y = 20 mm	Y = 0 mm	Y = 5 mm	Y = 10 mm
5333	2.20	2.85	3.00	3.20	2.00	2.20	2.30
10600	1.30	1.30	1.4	1.55	1.30	1.35	1.40
21600	1.20	1.20	1.35	1.50	1.35	1.35	1.40

Compared with smooth cylinder, the vortex formation region of the wake behind sinusoidal cylinder is elongated. The model 1 (λ/D = 2) has larger values than the model 2 (λ/D = 1). Along the span of wavy cylinder, the formation region length shows some variation. As point out by Bearman (1965)[3], the formation length is inversely proportional to the base pressure coefficient C_{pb}. The drag coefficient C_D mainly results from pressure difference acting on the upstream and downstream sides of the cylinder. In the subcritical regime C_D is proportional to C_{pb}. The elongation of vortex formation region brings high-pressure in the region near the rear side of the cylinder; hence the drag coefficient is decreased. In addition, the extension of the vortex formation region shifts downstream the vortices shed from the cylinder. The alternate shedding of vortices induces pressure fluctuations on the opposite side of the cylinder and brings about fluctuating lift coefficient C_L. The elongated vortex formation region in the near wake of wavy cylinder would cause drag reduction and the suppression of vortex-induced vibration.

3.2 Flow visualization

Visualized flow images of wake in the nodal and saddle planes at Re = 3000 and Re = 10,000 using the particle tracing method are shown in Fig. 5. The development of shear layer behind the geometric node resembles the results of the smooth cylinder. In the saddle plane, the wake becomes wider and small-size spanwise vortices appear inside the formation region. In the nodal plane, however, the wake is relatively narrower and the rolling up of the separated boundary layer into spanwise vortices seems to suppress or delay the development of spanwise vortices in the near wake region.

Fig. 6 shows the top views of the wakes behind two wavy cylinders (λ /D = 1 and 2) at Re = 3000 and Re = 10,000. At Re = 3000, a low-energy slow-moving region exists between the trailing edge of cylinder and the vortices shed from the cylinder. The size of this dead zone is decreased as Re increases. The streamwire vortices start to appear at about 1D downstream. For the sinusoidal cylinder of λ/D = 2, the streamwise vortices are more clearly seen, compared with those for the model of λ/D = 1 and the smooth cylinder.

Lam et al. (2003)[7] mentioned that there is significant spanwise flow from the saddle planes toward the nodal planes and depicted surface streamlines of 3-D flow near the separation line. At separation points, except nodes and saddles, the approaching flow moves along the separation line and leaves it tangentially into the wake flow. Consequently, the shear layers shed from the region near the saddles considerably extend along the spanwise direction. On the other hand, the shear layer near the nodes shrinks and the separated shear layer is accelerated as the flow goes downstream. It is reasonable to predict the existence of spanwise vortices between the saddle and nodal planes. In order to determine the influence of geometric shape on the streamwise vortex formation and near wake turbulent structure, more experiments on the 3-D separation in the boundary layer is needed.

4. CONCLUSIONS

Three dimensional flow structures of wake behind two sinusoidal cylinders were experimentally investigated. The sinusoidal cylinders reduce drag coefficient, compared with the smooth cylinder. The sinusoidal cylinder with λ/D = 2 shows the maximum 22% drag reduction at Re = 10^4. The wake structure varies significantly along the spanwise direction. In the saddle plane, the wake has larger velocity deficit and wider wake width, compared with the nodal plane. As the flow goes downstream, the flow in the saddle plane expands with entraining large amount of ambient fluid. However, the flow shrinks and accelerates in the nodal plane. The vortex formation length formed behind the sinusoidal cylinders is longer than that for the smooth cylinder. The elongations of vortex formation length also lead to drag reduction and suppression of flow induced vibration. The flow visualization results show clearly the 3-D vortex structure in the near wake region behind the sinusoidal cylinders.

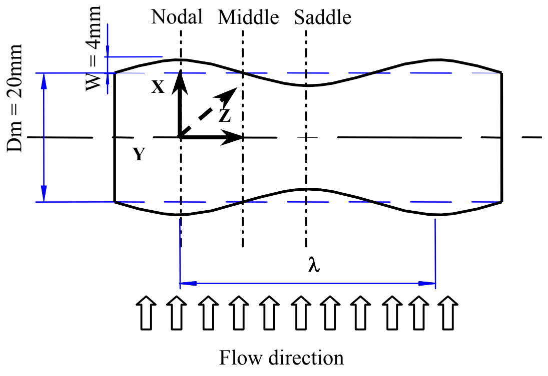

Fig. 1 Geometric and terminology of sinusoidal cylinder

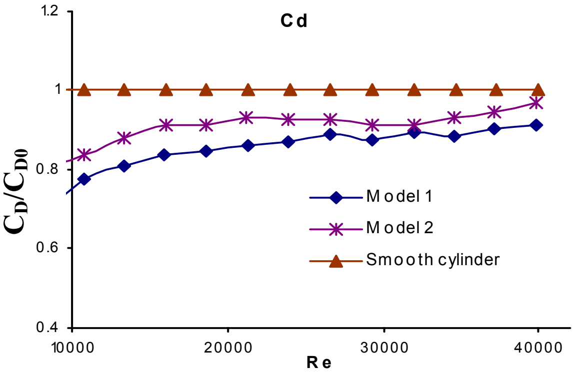

Fig. 2 Variation of drag coefficient

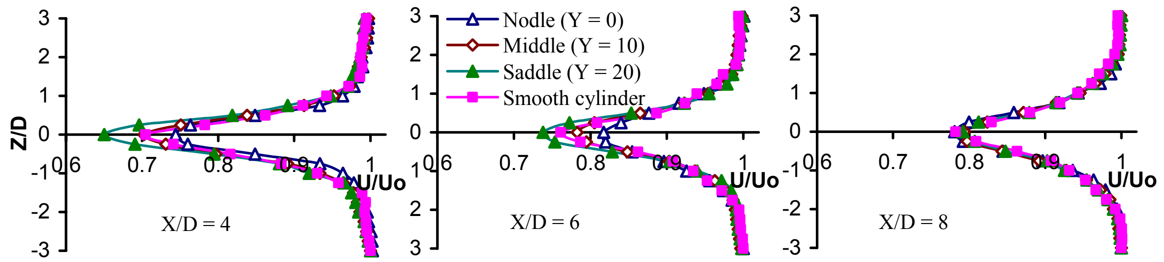

Fig. 3 Variation of mean streamwise velocity profiles for U_o = 4m/s (model 1)

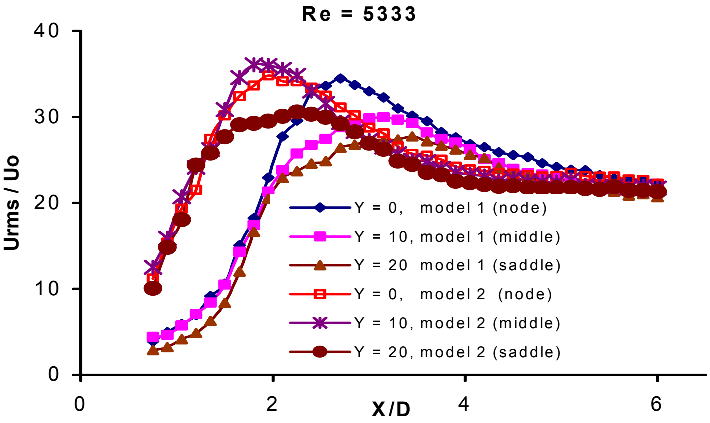

Fig. 4 Streamwise turbulence intensity distributions

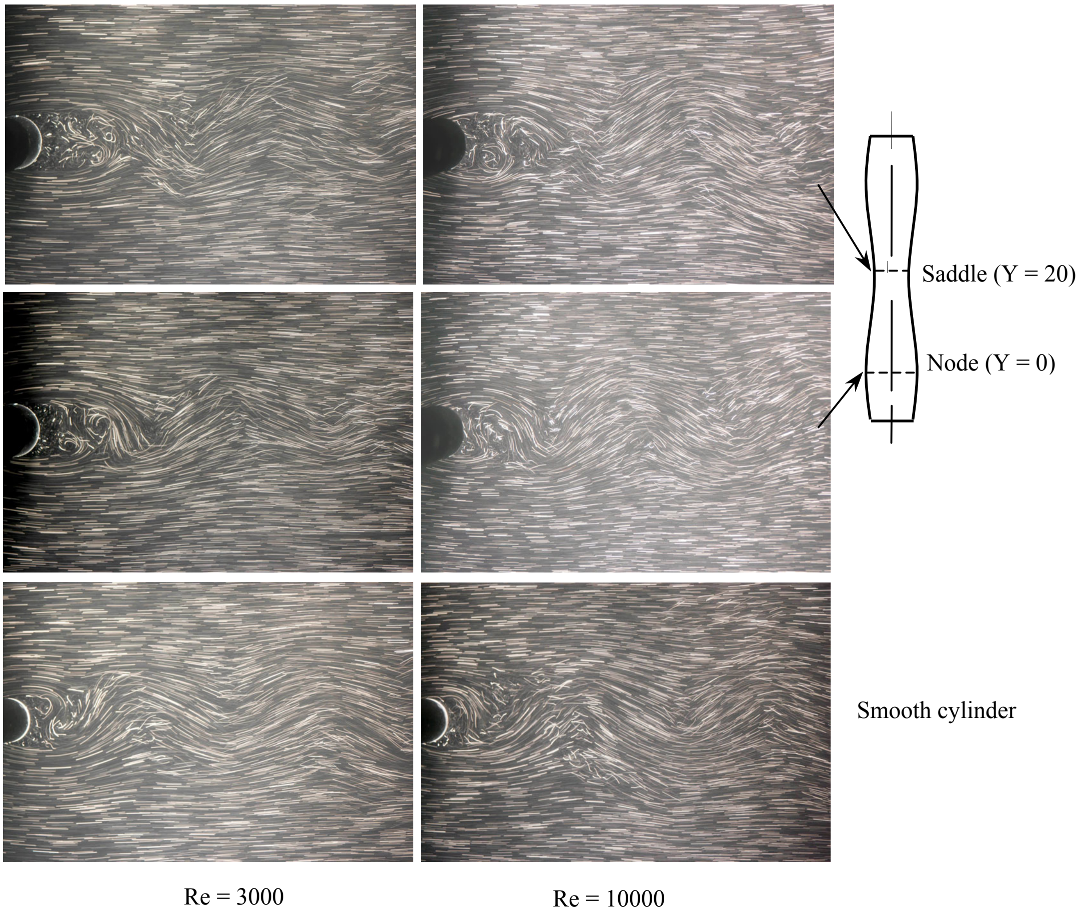

Fig. 5 Visualized flow behind the sinusoidal cylinder of λ/D = 2 in vertical cross-sections

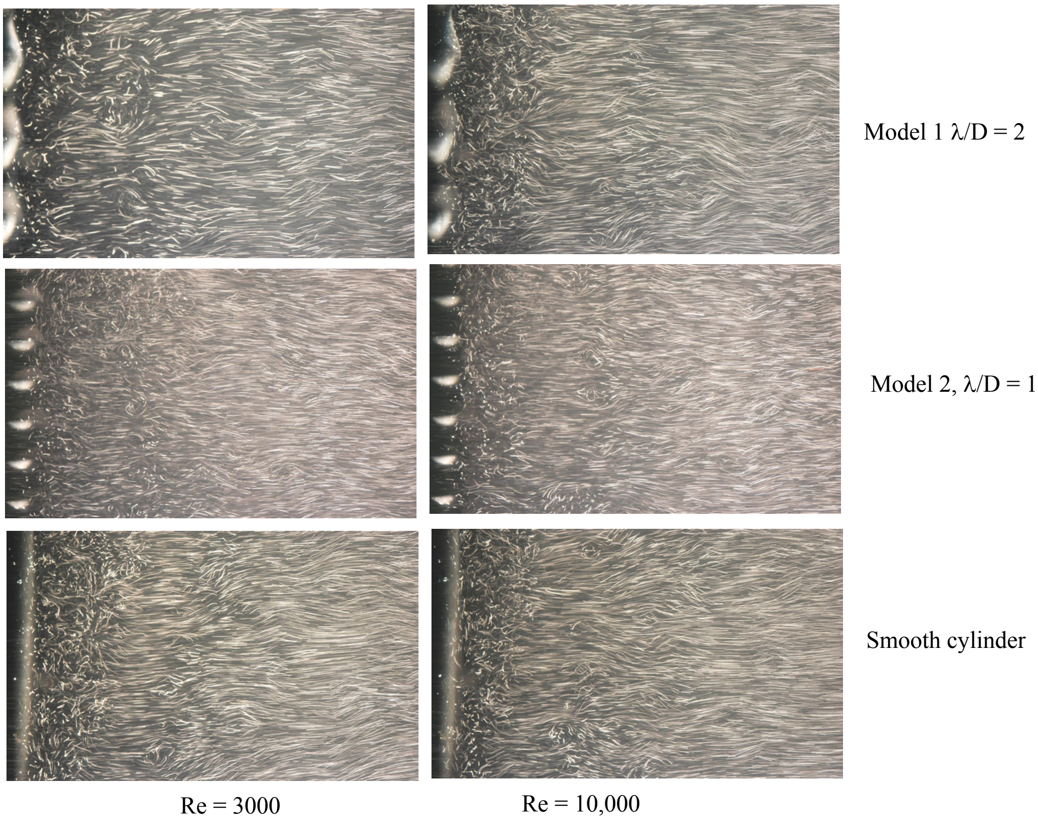

Fig. 6 Side view of the wake behind sinusoidal cylinders (λ/D = 1 and 2)

ACKNOWLEDGEMENTS

This work was financially supported by NRL (National Research Laboratory) program of the Ministry of Science and Technology, Korea.

REFERENCES

[1] Ahmed, A., Khan, M. J. and Bays-Muschmore, B. "Experimental investigation of a three-dimensional bluff body wake", *AIAA Journal*, Vol. 31, No 3,pp. 559-563 1993.

[2] Bearman, P.W. " Investigation of the flow behind a two-dimensional model with a blunt trailing edge an fitted with splitter plates. *J. of Fluid Mech*. Vol. 21, pp. 214-255, 1965.

[3] Bearman, P.W. and Owen, J. C. "Reduction of bluff-body drag and suppression of vortex shedding by the introduction of wavy separation line", *J. of Fluids and Structures*, Vol. 12, pp123-130, 1998.

[4] Bearman, P.W. and Tombazis, N. " The effect of three dimensional imposed disturbances on bluff body near wake flows, *J. of Wind Eng. & Industrial Aerodyn* Vol. 49, pp. 339-350, 1993.

[5] Bloor, M. S. "The transition to the turbulence in the wake of a circular cylinder", *J. Fluid Mech.* Vol. 19. pp. 291-304, 1964.

[6] Gerrad, J. H. "The mechanics of the formation region of vortices behind bluff bodies", *J. Fluid Mech.* Vol. 25. pp. 401-413, 1966.

[7] Lam, K., Wang, F. H., Jiang, G. D. and So, R. M. C. "Mean and fluctuating velocity fields in the near wake of wavy cylinder", *7th Int Symposium on Fluid Control, Meas. & Visualization*, 2003

[8] Tombazis, N. and Bearman, P. W. "A study of three-dimensional aspects of vortex shedding from a bluff body with a mid geometric disturbance", *J. Fluid. Mech.* Vol. 330 pp. 85-112, 1997

Proceedings of the Tenth Asian Congress of Fluid Mechanics
17-21 May 2004, Peradeniya, Sri Lanka

VORTEX SHEDDING IN THREE-DIMENSIONAL WAKES AT LOW REYNOLDS NUMBERS AND CONTROL

O.N.Ramesh_ & R.S.Chopde
(Department of Aerospace Engineering, Indian Institute of Science, Bangalore-560012, India)

ABSTRACT: In this experimental investigation, we study the control methodology to suppress the vortex shedding behind three-dimensional geometries. The 3D flow configurations investigated are (a) uniform flow over a tapered circular cylinder (b) linear shear flow over a straight circular cylinder and (c) Uniform flow over a straight circular cylinder with a step change in the diameter. Such three-dimensional vortex shedding patterns are in general dominated by the so-called cellular shedding patterns wherein the shedding is organised in spanwise localised cells of constant frequency as there is a lack of coherence all across the span. The control methodology used is similar to that of Strykowski & Sreenivasan [1] who used a small (circular) control cylinder just outside the wake in the near wake region of a larger cylinder which resulted in a complete suppression of vortex shedding of the larger diameter cylinder. In the case of [1], both the main cylinder as well as the control cylinder is two-dimensional and it was argued by them that the presence of the control cylinder resulted in reduced growth rates of disturbance in an otherwise absolutely unstable wake in the absence of any control cylinder. In the present case, it is found that the vortex shedding pattern behind three-dimensional situations as in (a) – (c) above could be likewise be completely suppressed by placing a small control cylinder just outside the wakes at certain locations. This is a very interesting result considering that the wake to be controlled is very strongly three-dimensional whereas the control cylinder is two-dimensional in geometry.

1. INTRODUCTION

Vortex shedding over 3D geometries such as a cone are known to be complex involving as they do the so-called cellular vortex shedding phenomenon, wherein vortex shedding is known to occur in cells of constant frequency. This can be easily be understood by the local dimensional argument $f \sim \frac{U}{D}$, where f is the frequency of shedding, U is the velocity of the fluid stream and D is the local diameter. Now if there is a spanwise variation of the diameter along the span as in 3D geometries such as a cone, it is conceivable that the frequency will continuously vary along the span of the cylinder with the shedding more frequent near the thinner end than the thicker end of the span. However, Helmholtz's theorem requires that the vortex tubes cannot end abruptly in the fluid. This means the shed vortices that are varying continuously in number (in a unit time) will have to connect among themselves in some fashion across the span and this leads to the so-called cellular shedding (see [2]). Another variant of this three-dimensional vortex shedding configuration is a linear shear flow over a straight circular cylinder. In terms of finer details there are some differences between a uniform flow over the cone and shear flow over a uniform cylinder; for example the shear has non-zero vorticity in the oncoming stream whereas the uniform flow over a tapered cylinder does not contain any vorticity in the oncoming stream. But in terms of the wake dynamics, these two situations tend to be treated as somewhat equivalent from the point of view of the wake structure – a local dimensional argument such as $f \sim \frac{U}{D}$ mentioned above would lead us to the conclusion that both of these flows involve cellular shedding and the number of cells across the span would depend on the taper ratio of the cylinder or an equivalent shear parameter to describe the upstream velocity gradient in the shear flow. In the present work, we will study the vortex shedding phenomena behind both these flows and seek to suppress the unsteady shedding by using a control methodology.

For the control, we follow the lead of Strykowski & Sreenivasan [1] who showed in their classic experiment that the vortex shedding behind a straight uniform cylinder could be suppressed by placing a much smaller control cylinder downstream of the main cylinder and slightly outside the wake. It was suggested by them that the control cylinder reduced the growth rates of the absolute instability/global modes of the wake and in some cases effectively suppressed the shedding. Physically, this meant that the control rod diverted a part of the fluid from the wake of the main fluid and this resulted in the vorticity smearing and, when the conditions were 'right', complete suppression of unsteady shedding also. We extend the same methodology of control to flow over cones in this study. But the main difference between the present study and that of [1] is that the present study seeks to control a very strongly 3D vortex shedding phenomenon but still with a 2D control cylinder as in [1]; in the case of [1], the frequency of shedding all across the span is a constant. i.e., a (nominally) 2D vortex shedding phenomenon was quenched by a 2D control cylinder. For our three dimensional flows under consideration, one could then expect the 2D control cylinder to alter the growth rates by different amounts along the span since the local Reynolds number is continually changing across the span. As a consequence one could perhaps expect partial quenching over part of the span whereas there is still shedding over the remaining part of the span due to the control rod. This expectation turns out to be over conservative in that for certain values of Reynolds numbers (based on the mean diameter or mean velocity as the case may be), vortex shedding over the whole span is quenched in a dramatic fashion. The possible reason is that the control rod works on the global instability modes and alter their growth rates all across the span even when the gap between the cone and the control cylinder varies along the span; a naïve local Reynolds number argument such as above does not take the global nature of the instability modes into account and as a result leads to modest expectations from the control methodology.

In the present work, we have investigated the vortex shedding and its control for the following configurations: (a) uniform flow over a tapered circular cylinder (b) linear shear flow over a straight circular cylinder (c) Uniform flow over a straight circular cylinder with a step change in the diameter. The last configuration (c) is meant to be a simplified picture of the wake flow in configuration (a) as envisaged by the investigations of Lewis and Gharib [3].

In the next section we will describe the results of the experiments done on the configurations (a)-(c). Finally, concluding remarks are made in the last section.

2. DESCRIPTION OF EXPERIMENTAL RESULTS AND DISCUSSION

The experiments were conducted in an open circuit wind tunnel, which has a test section of 300mm×300mm cross section and 3.2m long. Two end plates were used to arrest the meandering of the vortex tubes in the tunnel wall boundary layers. The oncoming freestream velocity was typically of the order of 0.5 m/s. This was measured by placing a uniform cylinder downstream and measuring the shedding frequency in its wake by using single component hotwire anemometry; the freestream velocity was then calculated by using the universal relation $St = 0.212 - 4.5/Re$, where $Re = Ud/\nu$, $St = fd/U$, with U and d being the freestream velocity and diameter respectively (see [4]).

The velocity fluctuation in the wake was measured by using a single component constant temperature hotwire anemometry.

The linear shear of the oncoming flow in configuration (b) is produced by placing a curved gauze upstream of the main cylinder; since the pressure drop across the gauze changes with the height, the resulting velocity in the wake downstream resulted in a shear flow and by a judicious choice of the gauze curvature along the height, a linear shear flow of any desired shear rate can be generated [5].

Flow visualisations in the wake were done with smoke flow released from a rake (which is encased in an aerofoil so that the rake does not produce its own vortex shedding) upstream of the main cylinder for cases (a) and (c). Smoke from incense stick (*agar bathi*) was collected in a container and passed through the rake and this resulted in a homogeneous good quality smoke visualisation. For case (b), the presence of the gauze presented certain difficulties with flow visualisation using this technique. Hence smoke flow visualisation using paraffin oil over a heated nichrome wire was used for this case. However, this technique of flow visualisation is especially plagued with problems of buoyancy due to low speeds of convection involved. As a result, the quality of flow visualisation picture is not as impressive as that obtained by using the first technique (using a smoke rake encased in an aerofoil shape).

In the following, some typical results for cases (a) – (c) are presented.

Case (a): Tapered Cylinder in a uniform flow.

The dimensions of the cone are: spanwise length (l) is 266 mm, smallest diameter (d_s) is 4 mm, largest diameter (d_l) is 9 mm and the taper ratio ($\frac{l}{d_l - d_s}$) is 53 – a fairly steep cone. The Reynolds number of the flow (based on the mid span diameter) is about 72. When there is no control cylinder the vortex shedding is present as can be seen from the smoke flow visualisations below. Figure 1a shows the top view and figure 1b shows the spanwise view of the phenomenon of low Reynolds number vortex shedding over the cone. It can be seen from figure 1b that this is a very complex flow when compared to a vortex shedding behind a straight circular cylinder. For the cone case, there is a dramatic variation of frequency across the span with cross-stream linkages of vorticity in conformity with Helmholtz's theorem. (As compared to the cone case, where there are many cells of shedding, a straight circular cylinder in a uniform flow case there will be just one cell, ignoring the end effects).

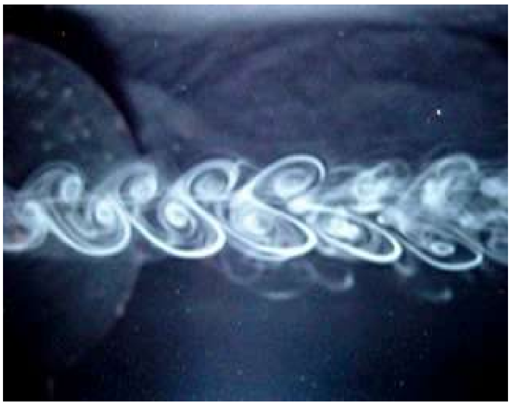

Figure 1a Shedding – Top view

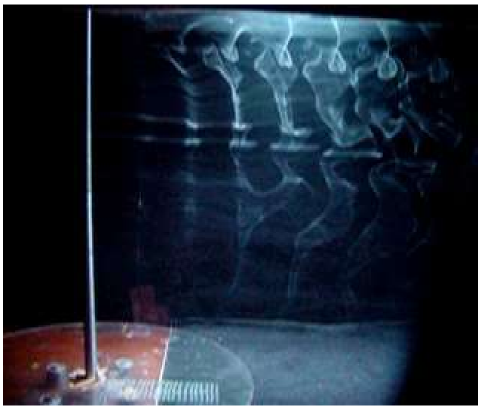

Figure1b Shedding – Spanwise view

Now following the lead of Strkowski & Sreenivasan[1], we introduce a much smaller control cylinder outside the wake of the main cylinder. The control cylinder has a constant diameter (=1.2 mm) all across the span (=266 mm) – i.e., it is 2D. The control cylinder is placed outside the wake such that its streamwise location $x = 2d$ times the mean diameter of the cone and the normal distance $y = 1.5d$, where d is the mean diameter of the cone. Figures 2a & 2b below respectively show the top view and the spanwise view of the resulting flow pattern with the introduction of a control cylinder. It can be very clearly seen that there is complete quenching of the vortex shedding phenomenon all across the span.

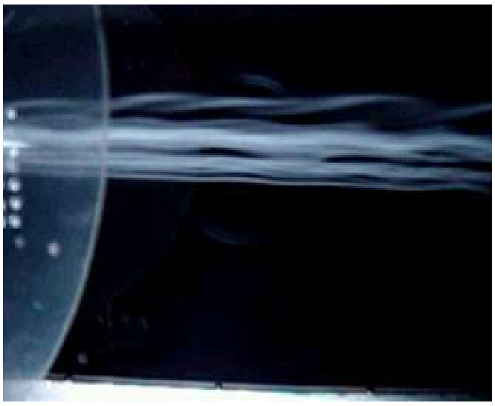

Figure 2a: Quenching – Top view

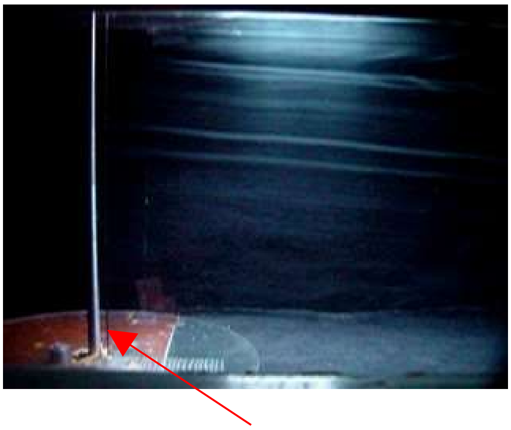

Figure 2b: Quenching – Spanwise view

The hotwire measurements corresponding to the above were also performed and the spectra of the steamwise velocity fluctuation component for various spanwise positions are presented below in figs 3a –b for the uncontrolled and controlled cases respectively. It can be seen from figure 3a from the power spectra of the streamwise velocity fluctuations that the dominant frequency (due to shedding) varies continually along the span in conformity with the picture depicted by figure 1b. When the control rod is introduced in the wake, there were absolutely no peaks in the spectra confirming complete quenching of vortex shedding all over the span and this is shown in figure 3b below.

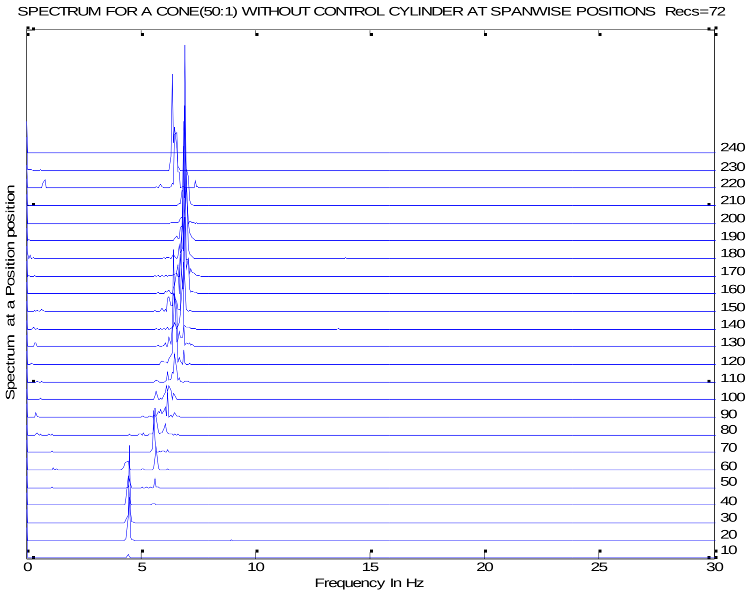

Figure 3a: Spectra of cone wake - Shedding

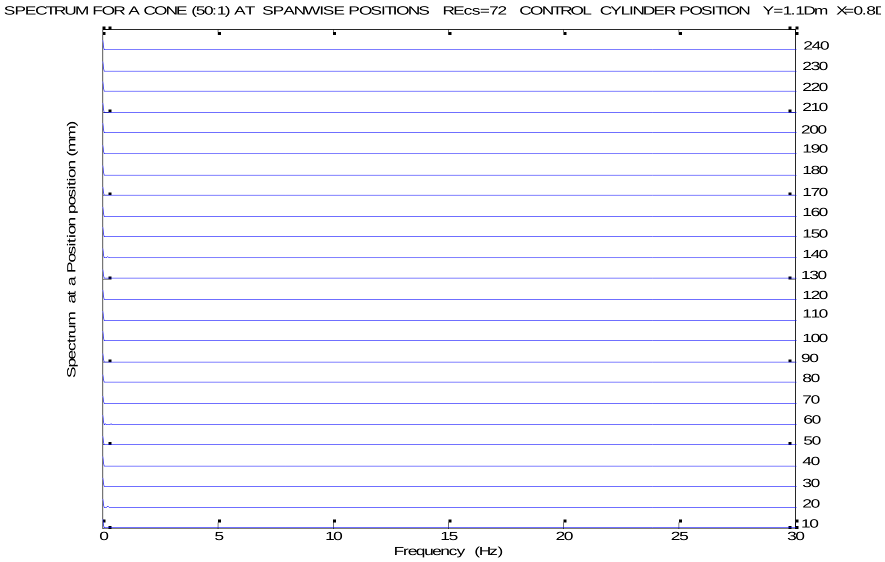

Figure3b: Spectra of cone wake -Quenching

The control methodology was successful in completely quenching the shedding in the main cylinder wake over a range of the control rod positions but the measurements at other locations or the domain of influence of the control rod are not presented here for lack of space.

Case (b): Linear Shear flow over a straight circular Cylinder

As mentioned earlier, an oncoming linear shear flow was produced by using a curved gauze and a typical

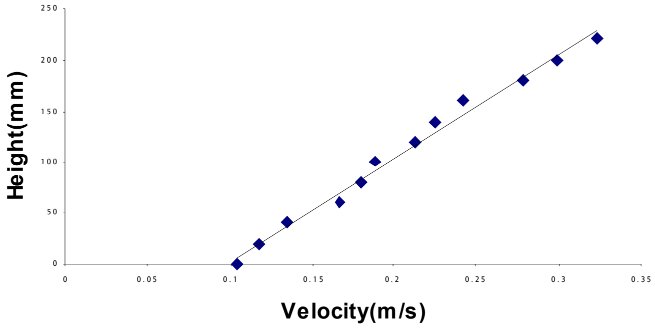

Figure 4: Linear shear flow – velocity variation with height

measured profile of velocity is shown in figure 4. The shear rate, defined as $\beta = \frac{1}{U_{ave}}\left(\frac{du}{dz}\right)$, was 0.016 for this case. The velocity was measured using an improvised vortex shedding meter and the details of this method will be published elsewhere.

The spanwise view of flow visualisation of the wake of a circular cylinder in this shear flow is presented below in figures 5a and 5b for the uncontrolled and controlled cases respectively. From figure 5a it can be seen that in the uncontrolled case, the vortex shedding is organised in cells similar to that in flow over cone. The control rod was placed at the location $x = 1.5d$, $y = 0.5d$, where d is the diameter of the main cylinder. It can be seen that yet again for this 3D case also there is complete quenching of shedding due to the control rod placement. The spectra of streamwise velocity component in the wake at different spanwise positions is shown in figure 6 by way of corroborating the cellular shedding structure shown if figure 5a.

Figure 5a: Shear flow wake - Shedding

Figure 5b Shear flow wake wake-Quenching

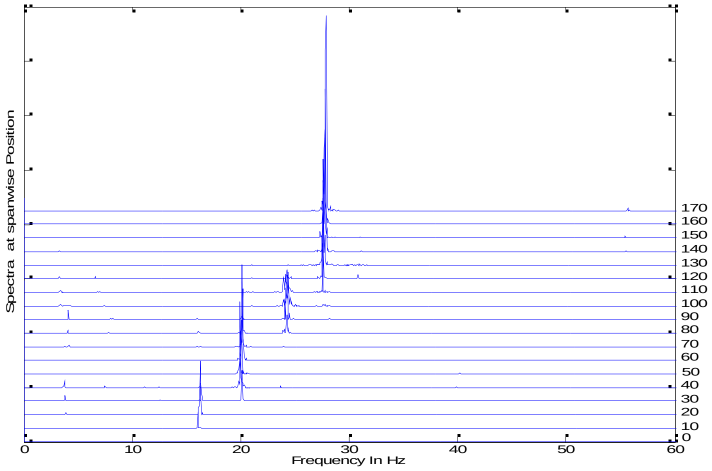

Figure 6. Spectra of streamwise velocity component in shear flow wake at various spanwise locations

Case (c): Uniform flow over a straight circular cylinder with a step change in diameter

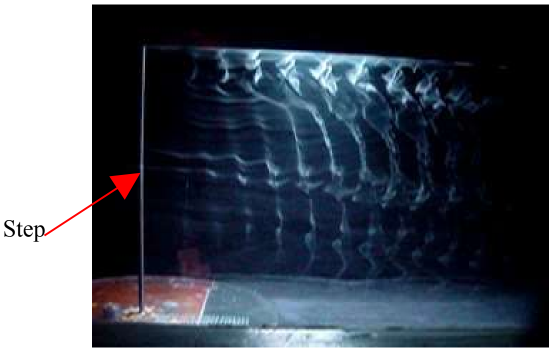

Figure 7a: Stepped cylinder wake - Shedding

Figure7b Stepped cylinder -Quenching

As a final case, we present the spanwise view of the wake of a stepped cylinder in a uniform flow for the uncontrolled and controlled cases respectively in figures (7a) and (7b) above. The diameter ratio is 1.1. The control rod was placed at $x = 1.8d_2$ and $y = 1.1d_2$, where d_2 is the diameter of the larger side of the stepped cylinder. The Reynolds number based on the larger diameter is about 72. Again the results are similar to those in cases (a) and (b) viz., presence of cellular vortex shedding in the absence of any control and complete quenching of shedding with control.

Discussion

The success of this control methodology in the 2D experiments of Strykowski and Sreenivasan [1] was attributed by them to the quenching of the growth rates by the control rod in the otherwise absolutely unstable modes of the wake.

For the 3D experiments as in the present study it may at first sight appear surprising that a 2D control cylinder should be successful in suppressing a very complex 3D shedding phenomenon as vorticity smearing due to the control rod (envisaged in the 2D scenario in [1]) may be expected to be non-uniform all over the span in a 3D geometry. However, a vortex shedding phenomenon in a 2D flow is known to be dominated by the so-called global modes – these are instability modes with a zero group velocity and the same frequency all over the wake. It is also well known from studies which use model equations (such as Ginzburg Landau equation) to study the vortex shedding phenomenon with spanwise variations in geometry [6], that a spanwise shear weakens the global mode structure. Hence the presence of a control rod in a three-dimensional wake perhaps damps the growth rate in an already weakened instability mode. This might perhaps explain the success of a 2D control cylinder in suppressing a 3D vortex shedding as in cases (a) –(c) discussed above.

3. CONCLUSIONS

A 2D control rod placed in the wake of a three dimensional vortex shedding configuration was found to completely suppress the unsteady shedding pattern. This is attributed to the weakening of the so-called global instability modes (which are already weakened by an imposed shear due to the 3D geometry) further by the control rod and when the conditions are just 'right' leading to complete curbing of growth rates thereby resulting in suppression of shedding altogether.

REFERENCES

[1] Strykowski P and Sreenivasan KR. On the formation and suppression of vortex shedding at low Reynolds numbers. J Fluid Mech., 1989, 218:71-107.
[2] Gaster M. Vortex shedding from slender cones at low Reynolds numbers. J. Fluid Mech., 1969, 38 (3):564-576
[3] Lewis C and Gharib M. An exploration of wake three dimensionalities caused by a local discontinuity in cylinder diameter. Phys. Fluids, 1992, A4 (1):104-117
[4] Gaster M. Vortex shedding from circular cylinders at low Reynolds numbers. J. Fluid Mech., 1971, 46(4):749-756
[5] Maull DJ and Young RA. Vortex shedding from bluffs bodies in shear flow. J Fluid Mech , 1973;60:401-409.
[6] Park DS and Redekopp LG. A model for pattern selction in wake flows, Phys Fluids, A, 1992, Vol 4 (8), 1697-1705

Proceedings of the Tenth Asian Congress of Fluid Mechanics
17-21 May 2004, Paradeniya, Sri Lanka

Non-linear Development of Forced Wavelength Görtler Vortex Flow

H. Mitsudharmadi*, S.H. Winoto, and D.A. Shah
Department of Mechanical Engineering, National University of Singapore
10 Kent Ridge Crescent, Singapore 119260, SINGAPORE
*Corresponding Author: E-mail: engp2489@nus.edu.sg

ABSTRACT: The development of forced wavelength Görtler vortex flow was investigated in the boundary layer of a concave surface of 2.0 m radius of curvature. The wavelength of the vortex flow was forced by the presence of 13 vertical perturbation wires located upstream of the concave surface leading edge. The measured streamwise velocity contours reveal the spanwise structure in the streamwise region in which the mushroom shape structures are coherent and dominating the flow. The growth of the secondary instability that is associated with the inflectional profiles in the spanwise directions which produce the temporal velocity fluctuations, can be seen in the contours of u'_{rms} that has been normalized by the free-stream velocity U_∞ in the y-z plane. It is found that two-peaks in the u'_{rms} distribution are located at the sides of low speed regions at all streamwise locations. This implies that the vortices are vulnerable to a secondary instability which is governed by the inflectional velocity profiles in the spanwise direction.

1. INTRODUCTION

Counter-rotating streamwise vortices is one of the most prevalent eddy structure found in both transitional and turbulent bounded shear flows. The development and breakdown of counter-rotating streamwise vortices generated via a Görtler instability mechanism has been used to experimentally model the eddy structures found in transitional and turbulent flat-plate boundary layers.

The growth of the disturbance velocity generated by Görtler instability mechanism is used to categorize the linear or the non-linear region of the flow field. As the disturbance velocities grow above a few percent of the free-stream velocity U_∞, nonlinear effects become important and the linear equations no longer accurately predict the disturbance evolution. [1] Accordingly the flow is considered in the nonlinear region. It is indicated by the formation of the horseshoe vortices that are formed from the wavy shape structure observed in the iso-velocity structure at the y-z plane. Further downstream these horseshoe vortices will form the mushroomlike structures. These coherent structures will be destroyed farther downstream by secondary instabilities and fine-scale turbulence development. [2] However, there will be a finite region in which the mushroomlike structures dominate the flow.

The secondary instability manifests itself either as varicose or sinuous transverse oscillation mode. The varicose mode is responsible for developing fluctuations on the spanwise structure and it coincides with the regions of high shear at the mushroom hat. [3] It looks like a small horseshoe eddies formed between two neighbouring vortices travelling in the streamwise direction. This horseshoe vortex street appears at irregular intervals periodically being replaced by a secondary instability called the sinuous mode.

This sinuous mode manifests itself as an unsteady meandering of the vortices and associated with the inflectional profiles, which produce the temporal velocity fluctuations. It is driven by the spanwise gradient near the mushroom stem. [3] The sinusoidal transverse oscillations of the streak-lines are an example of sinuous instability mode and can be the most important in the transition to turbulence. A global energy balance study conducted by Yu and Liu [4] verified the amplification rates obtained from secondary instability analysis and confirmed that the sinuous mode would dominate.

The rapid increase in temporal fluctuations takes place in the region where the spanwise structure begins to smear out. This phenomenon can be found downstream of the location where the spanwise structure collapses very quickly. It is related to the increased mixing due to the onset of turbulence. The growth and breakdown of the vortices caused by the Görtler instability are quite similar to those found in the transitional and turbulent flow field [5].

The aim of the present study is to show that the growth of the secondary instability associated with the inflectional profiles that produce the temporal velocity fluctuations in the non-linear developing forced wavelength Görtler vortex flow. The rms-streamwise velocity u'_{rms} structures that have been normalized by the free-stream velocity U_∞ together with the corresponding iso-velocity structures will be presented to provide a clearer picture of the non-linear development of forced wavelength Görtler vortices.

2. EXPERIMENTAL DETAILS

The experiment was carried out in a 60° curved test section with a rectangular cross-section of 0.15 m x 0.60 m, connected to a low speed, blow down type wind tunnel is used to carry out the experiments. A smooth concave test surface of 2.0 m radius of curvature is mounted inside the perspex (plexiglass) curved test section at a distance of 0.05 m from its bottom surface (Fig.1). Thirteen perturbation wires with diameter of 0.2 mm are positioned at 10 mm upstream of the leading edge and the distance between each wire is 15 mm. Fine mesh screens were installed at the inlet to provide uniform flow in the test section with free stream turbulence levels of about 0.35 % for the free-stream velocity range of 1.5 m/s to 9 m/s.

A single hot-wire probe of special design for boundary layer measurements is used to carry out mean and fluctuating velocity measurements in the boundary layer. This probe was operated in a Constant Temperature Anemometer (CTA) mode, which is coupled to a signal conditioner. The signal was low passed filtered at 3000 Hz and sampled at 6000 Hz for the duration of 21 seconds. The data collected were digitized using the A/D (analog to digital) converter card DT3016, which is installed in PC. The data was further analyzed using the HPVEE software.

For the hot-wire calibration, a pressure transducer that has been calibrated using a micro-manometer was used in conjunction with the Pitot-static tube located in the free-stream. The King's law provides the basis for the prediction of the forced convection heat transfer from a hot wire. During the measurements along the spanwise direction the Pitot-static tube was positioned in the free-stream. It was connected to the pressure transducer to monitor the local free-stream velocity. Both hot-wire probe and Pitot-static tube were mounted on a traversing mechanism. Two stepper motors control the movement of the traversing mechanism along the y and z directions with an accuracy of ± 0.01 mm. The measurements were carried out in the y-z plane with the step size of 1-mm along the z direction.

3. RESULTS AND DISCUSSIONS

Figures 2 (a) - (f) show the contours of U/U_∞ in the cross-sectional (y-z) plane at 6 streamwise (x) locations (at x =200, 500, 600, 700, 805, and 904 mm). The corresponding Blasius boundary layer thickness δ is indicated on the ordinate for each streamwise location. To smooth the iso-velocity contours, Tecplot software was used. By assuming that the second derivative normal to the boundary is constant, it results in the data being smoothed near the boundary. To include the effect of rounding out peaks and valleys rather than eliminating them, 5 points are chosen to be the number of smoothing passes to perform with the relaxation factor for each pass of smoothing as 0.5. The presence of the wake velocity profile behind vertical perturbation wires gives rise to a spanwise modulation of streamwise velocity U with the period similar to the spanwise spacing between the wires. The high velocity regions (downwash) occur in the spacing between wires at which the boundary layer thickness is thinner than that in the low velocity regions (upwash) that occur downstream of each vertical perturbation wire.

It is shown in Figs. 2 (a) – (f) that at x = 200 mm from the leading edge, the contours are wavy in the spanwise (z) direction, which indicate the occurrence of Görtler vortices at this location where G_θ = 2.393. The wavy shapes become more pronounced as the flow developed downstream indicating the amplification of the vortices. Furthermore these vortices will evolve to form the horseshoe vortices. The transformation of the horseshoe vortices that propagate downstream into the mushroom shape structure before breaking down, is the consequence of the nonlinear growth of Görtler vortices. It shows the occurrence of the varicose mode instability as a secondary instability [2]. The mushroom shape vortices as the spanwise structure is clearly depicted starting at x = 700 mm, while at x = 904 mm the structure starts to decay. The breakdown of these spanwise structures could be attributed to the increased mixing due to the onset of turbulence. The mushroom shape structures as shown in Figs. 2 (d)–(f), reveal the structure of finite amplitude Görtler vortices, and identify the streamwise region in which the mushroom shape structures are coherent and dominating the flow. The development of the mushroom shape structure is due to the strong nonlinearities in the cross-sectional y-z plane [2].

The corresponding distribution of the temporal velocity fluctuations in y-z plane are presented in Figs 3 (a) – (f) by plotting the u'_{rms} that has been normalized by free-stream velocity U_∞. Unlike the contours of U/U_∞ , the temporal velocity fluctuations contours are not smoothed. After comparing these figures with those presented in Figs. 2 (a) – (f), it is shown that the developing fluctuations are associated with the low-speed streaks, since the presence of two peaks in the u'_{rms} distributions are located on the sides of the low speed regions. This result led to the conclusion that the vortices are susceptible to a secondary instability which is governed by the inflectional velocity profiles in the spanwise direction. As the breakdown of the spanwise structures is approached, a secondary peak in the u'_{rms} develops near the wall as can be seen in Figs. 3 (d) – (f). It has a smaller scale but ultimately attains the highest amplitude in the evolution of the streamwise vortices as reported earlier by Swearingen and Blackwelder [6]. The unclear structures near the wall in the u'_{rms} contours could be due to inadequate probe resolution in this region.

4. CONCLUSIONS

The growth of the mushroomlike structures in the non-linear developing forced wavelength Görtler vortex flow had been studied. The streamwise mean velocity contours reveal the structure of finite amplitude Görtler vortices, and the streamwise region in which the mushroom shape structures are coherent and dominating the flow. The development of these mushroomlike structures is caused by the strong non-linearity in the cross-sectional y-z plane. The contours of u'_{rms} that have been normalized by the free-stream velocity U_∞ show the growth of the secondary instability that is associated with the inflectional profiles in the spanwise directions which produce the temporal velocity fluctuations. It is also shown that the vortices are susceptible to a secondary instability which is governed by the inflectional velocity profiles in the spanwise direction.

ACKNOWLEDGEMENT

The authors would like to thank the National University of Singapore (NUS) for the financial supports provided to this research work, and to the technical staff of the Fluid Mechanics Laboratory, for their assistance in conducting the experiment.

REFERENCES

[1] Schmid, P.J., and Henningson, D.S.,”Stability and transition in shear flows,” *Applied Mathematical Sciences*, Vol. 142, Springer-Verlag, New York (2001).

[2] Lee, K., and Liu, J.T.C. (1992),”On the growth of mushroomlike structures in nonlinear spatially developing Görtler vortex flow,” *Physics of Fluids* A, 4 (1), 95.

[3] Bakchinov, A.A., Grek, G.R., Klingmann, B.G.B., and Kozlov, V.V. (1995),”Transition experiments in a boundary layer with embedded streamwise vortices,” *Physics of Fluids*, 7 (4), 820.

[4] Yu, X., and Liu, J.T.C. (1994), “On the mechanism of sinuous and varicose modes in three-dimensional viscous secondary instability of nonlinear Görtler rolls,” *Physics of Fluids* 6 (2), 736.

[5] Bippes,”Experimental study of the laminar-turbulent transition of a concave wall in a parallel flow,” *NASA TM-75243* (1972).

[6] Swearingen, J.D., and Blackwelder, R.F. (1987),”The growth and the breakdown of streamwise vortices in the presences of a wall,” *Journal of Fluid Mechanics*, 182, 225.

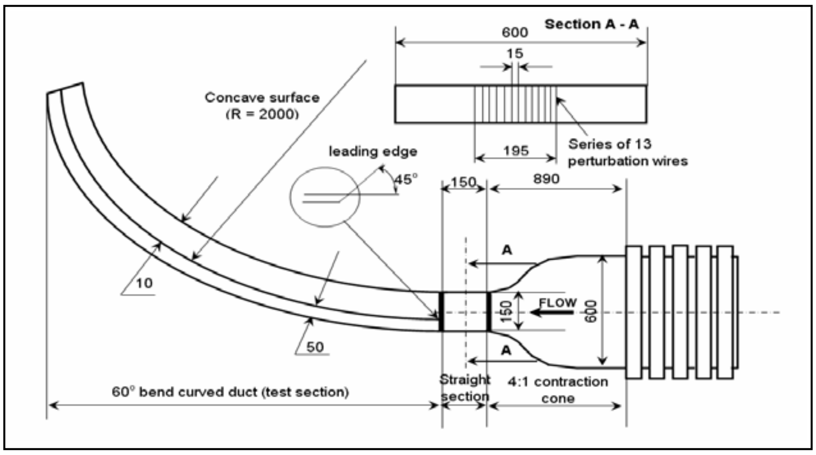

Fig. 1 Sketch of the wind tunnel, curved test section and concave test surface (all dimensions are in mm).

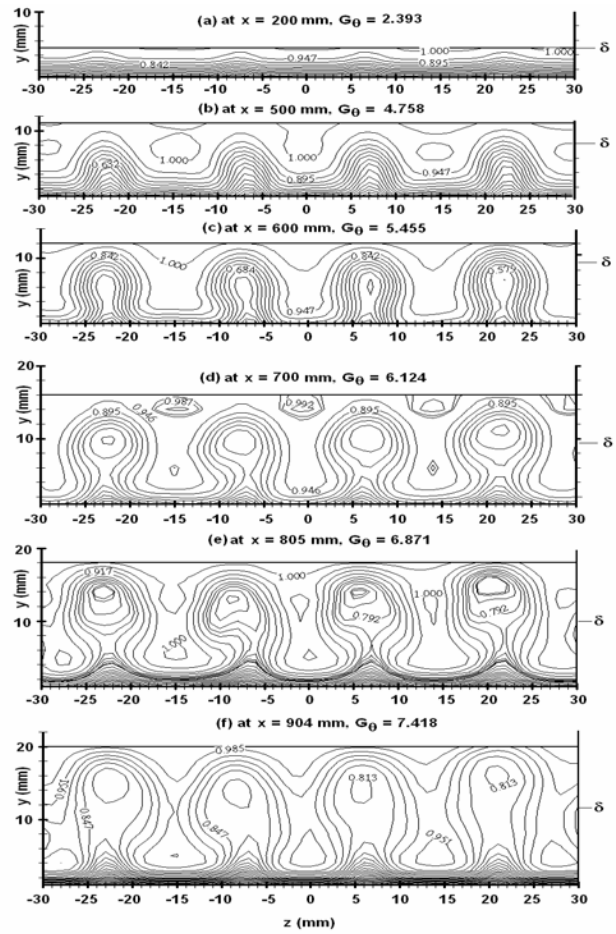

Fig. 2 Mean streamwise velocity (U/U_∞) contours showing the evolution of Görtler vortices in boundary layer flow on a concave surface of 2.0 m radius of curvature at free-stream velocity $U_\infty = 3$ m/s.

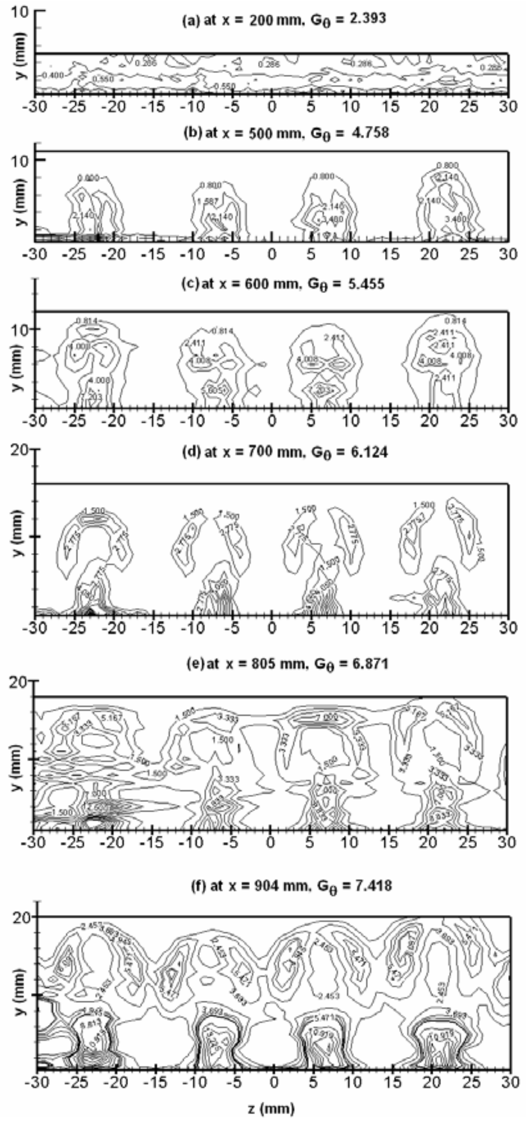

Fig. 3 u'_{rms}/U_∞ (in %) contours showing the growth of the secondary instability associated with the inflectional profiles in the spanwise directions at free-stream velocity $U_\infty = 3$ m/s.

Proceedings of the Tenth Asian Congress of Fluid Mechanics
17-21 May 2004, Peradeniya, Sri Lanka

EFFECT OF FORWARD SWEEP ON THE PERFORMANCE AND STALL MARGIN OF A LOW SPEED AXIAL COMPRESSOR

O.G. Krishnakumar, M. Govardhan and N. Sitaram
Thermal Turbomachines Lab, Department of Mechanical Engineering,
Indian Institute of Technology, Madras-600 036.

ABSTRACT: The paper presents the experimental study of forward sweep on the performance and stall margin of a low speed axial flow compressor. The performance and three-dimensional flow behind 10° forward sweep and 20° forward sweep rotors are compared with baseline unswept rotor. Tip-chordline sweep is employed for the current investigation. The results indicate that low sweep angle could improve the performance in terms of pressure rise, whereas an increase in sweep angle brings down the pressure rise from the rotor. The peak efficiency of forward swept rotors is more than the unswept rotor and well away from the stall to be ideal for practical applications. The rotor exit flow measurements revealed that the forward sweep causes the flow to shift towards the hub

1. INTRODUCTION

The concept of sweep was originally developed and applied for aircraft wing designs where it was used to reduce drag and flow losses at transonic speed. Stress considerations prohibited the application of forward sweep to high-speed compressors for decades after the concept was proposed, though the advances in the material considerations and accurate stress predictions made it possible at present.

The term sweep refers to the tilting of blade sections in the direction of chord, whereas dihedral refers to the tilting of the blade sections perpendicular to the direction of the chord. According to Smith [1], blade sections should be cut by surfaces that are tangent to the axisymmetric stream surface of the meridional flow and these cross sections should be viewed parallel to the stacking line of the blade. This procedure ensures that the resulting blade sections are most nearly comparable to the design criteria. In the present programme, a tip-chordline sweep is employed for the investigation, where each blade section from hub to tip is moved in the direction of tip-chord in such a way that the movement is zero at the hub and progressively increasing along the span to be maximum at the tip. Schematic diagram in Fig.1 gives sweep, dihedral and skew angles for an axial flow compressor.

The main objective for which the concept of forward sweep is evolved and applied for is to improve the operating range and most importantly the stall margin characteristics of the axial flow compressor. It is well known that the operating range of the axial compressor is low at high speeds.

2. EXPERIMENTAL SETUP AND INSTRUMENTATION

The experimental setup (Fig. 2) is a single stage axial flow compressor consisting of a rotor followed by downstream guide vanes. The rotor is designed to give a forced vortex flow at constant exit absolute flow angle, and a specific work of 425 m^2/s^2 at a flow coefficient of 0.6. The rotor consisted of twelve blades with a tip diameter of 400 mm and a hub diameter of 200 mm fixed on an aluminium hub. The drive to the compressor is given by a 7.5 kW, 2900 rpm AC induction motor. The mass flow through the compressor is regulated by means of a throttle control mechanism provided at the inlet. The mass flow through the rotor is calculated from the mass averaged axial velocity at the rotor inlet.

3. EXPERIMENTAL PROCEDURE

Traverse at the rotor inlet was done with the help of three-hole probe whereas that at the exit of rotor was done with the help of five hole probe. Five hole probe was needed in order to study the three dimensional flow pattern behind the rotor since the radial flow become more predominant at lower flow rates. These probes were calibrated in a non-nulling mode in the calibration tunnel facility available in the laboratory.

All the measurements were taken with the help of *Furness Controls,U.K.* make micromanometers (FC012).

The probe traverses were done at close intervals from hub to tip. The wall static pressure from the casing wall was also taken. These flow measurements were carried out at different throttle positions at a constant speed of 2000 rpm. From the calibration chart, true total pressure, true static pressure and flow direction were determined. The temperature and pressure at the time of experiment was also noted down to calculate the density of air.

The average total pressure rise across the rotor is an indicative of the amount of energy transferred from the rotor. This was non-dimensionalized by the product of density and square of tip speed to get energy coefficient ψ. The mass averaged meridional velocity at the rotor inlet was non-dimensionalized by the tip speed to get the flow coefficient ϕ

4. RESULTS AND DISCUSSION

4.1 Comparison of Performance

The comparison of performance (Fig.3) reveals that 10^o forward swept rotor has developed the highest pressure rise among all the three rotors tested. However, when the sweep angle was further increased to 20^o forward sweep, the pressure rise is reduced below the level of the baseline rotor. An observation of this kind has not been reported so far. Investigations by Wadia et al.[2], Mohammed and Raj [3] have observed high pressure rise with the forward swept rotor, while Helming[4], Beiler et al.[5] and Yamaguchi et al. [6] have observed pressure reduction with forward sweep.

It is known that the loading of a swept airfoil is theoretically reduced according to the cosine of sweep angle. Assuming valid, 10^o forward swept blade would be developing a pressure rise 1.5% lower that the unswept blade and 20^o forward swept blade would be developing a pressure rise 6% lower than the unswept blade. This could be the reason behind the low total pressure rise developed by the 20^o forward swept blade. But for an axial turbomachine, the spanwise flow caused by swept blades will be modified by hub and casing and hence the loading of a swept blade would not gradually decrease along the span as the theory of infinitely long airfoils predict (Kuchemann [7] and Thwaites [8]). Thus with rotors employing low sweep angles, the pressure rise could be even higher than the unswept rotor.

It could be seen that 10^o forward sweep though increased the operating range has not increased the stall margin. Whereas, 20^o forward sweep has resulted an increased operating range and stall margin but at the expense of pressure rise. This shows that a high angle of forward sweep is necessary to achieve a high stall margin. On the other hand, pressure rise will be low for rotors employing high sweep angles.

4.2 Comparison of efficiency

The efficiency (Fig.4) of 10^o forward swept rotor is higher than the unswept rotor by about 3% at design: $\phi = 0.60$, whereas 20^o forward swept rotor improved the efficiency by about 4.2% from the baseline rotor at this flow rate. Also, the peak efficiency of the unswept rotor is close to stall. On the other hand, both forward swept rotors gave maximum efficiency to the right of stall point. This is advantageous, as it is possible to operate the compressor near the best efficiency point without getting stalled. Towards stall region, the efficiency of swept rotors reduces with 20^o forward swept rotor showing low efficiency values.

.

The shift of streamlines towards the hub will make the flow pattern uniform in a forward swept rotor by increasing the flow near the hub and decreasing the flow near the casing. The radial distribution of blade loading becomes more uniform with midspan sections taking a major portion of blade work in forward sweep. The improvement in efficiency is due to these improved flow conditions within the forward swept rotor.

4.3 Total pressure rise coefficient

The 10^o forward swept blade showed high total pressure rise almost uniformly from the hub to the tip, Fig. 5. With 20^o forward sweep, the high total pressure rise is observed only near the hub at high flow coefficient of $\phi = 0.71$. At low flow coefficient of $\phi = 0.56$ this is not observed. Near the casing, the total pressure rise of the 20^o forward swept rotor is lower than the unswept rotor and this is more prominent at $\phi = 0.56$.

4.4 Axial velocity distribution

The axial velocity distribution at the exit of the rotor is plotted for $\phi = 0.56$ and $\phi = 0.71$ in Fig. 6. The design of the blade is such that axial velocity is constant from hub to tip. At all flow coefficients, the axial velocity is less at the hub and increases towards the tip sections. This radial gradient of the axial velocity increases as the flow rate is reduced. This clearly shows that the radial shift of streamlines from the original axisymmetric stream surface is higher at low flow rates.

The axial velocity distribution for the swept rotor is more uniform from hub to tip as compared to the unswept rotor. Axial velocity near the hub is more with forward sweep. Near the tip, the axial velocity of the swept rotors is lower than the unswept rotor. This redistribution of axial velocity at the exit of swept rotors shows that forward sweep causes flow to deflect towards the hub. Since the streamline shift is expected to follow this trend, the result of this flow redistribution will be to reduce the boundary layer accumulation near the casing region. The high stall margin observed in 20^o forward swept rotor is a manifestation of this aspect.

4.5 Tangential velocity distribution

Tangential velocity distribution (Fig.7) at rotor exit is indicative of the energy transfer from the blades. The tangential velocity magnitudes of the 10^o forward swept blade are higher than the unswept blade in almost the entire span of blade. This is in agreement with the total pressure rise distribution. Tangential velocity is more near the hub with 20^o forward swept rotor at $\phi = 0.71$, and at $\phi = 0.56$ it is low. At the same time, tangential velocity magnitudes near the casing are low with the 20^o forward swept rotor at these two flow coefficients, as originally seen from the total pressure rise distribution.

4.6 Radial Velocity distribution

From the radial velocity distribution, Fig. 8, it could be inferred whether the nature of streamline flow within the rotor is towards the hub or casing. At $\phi = 0.71$, the radial velocity of forward swept rotors is lower than the unswept rotor, with 20^o forward swept rotor showing the least magnitudes. On the other hand, at $\phi = 0.56$, radial velocity magnitudes of the 10^o forward swept rotor is higher in the midspan as compared to the unswept rotor, whereas 20^o forward swept rotor still shows low values of radial velocity in almost entire span of the blade.

This means that the effect of forward sweep to cause a downward flow towards the hub is more prominent at high flow coefficient. As the flow rate is reduced, the boundary layer growth on the suction surface becomes thicker, and the ability of forward sweep to induce flow towards the hub will be dominated by the centrifugal effects. In order to achieve high stall margin, a high angle of forward sweep is necessary.

5. CONCLUSIONS

Low sweep angle could improve the pressure rise, whereas a high sweep angle results in low pressure rise from the rotor. A high angle of forward sweep is necessary in order to achieve a high stall margin characteristic. Forward sweep results in improved stall margin and efficiency, but in this attempt total pressure rise has to be sacrificed. Forward sweep reduces the pressure rise near the casing and improves the pressure rise near the hub to make the total pressure rise uniform from hub to tip. Axial velocity with forward sweep is low near the casing and more near the hub to make the mass flow through the blade channel uniform from hub to tip. This also shows that the effect of forward sweep is to induce the flow towards the hub. Forward sweep effects diminish at low flow rates suggesting the need of high sweep angles.

REFERENCES

[1] Smith LH Jr and Yeh H: Sweep and dihedral effects in axial flow Turbomachinery. J. of Basic Engg, Trans. of ASME, 1963, **75**, 401-416

[2] Wadia AR, Szucs PN and Crall DW: Inner workings of aerodynamic sweep, ASME J. of Turbomachinery, 1998, **120**, 671-682.

[3] Mohammed KP and Raj DP: Investigations on axial flow fan impeller with forward swept blades, ASME Paper No. 77-FE-1.

[4] Helming K: Numerical analysis of sweep effects in shrouded propfan rotors, J. of Propulsion and Power, 1996, **12 (1)**, 139-145.

[5] Beiler MG and Carolus TH: Computation and measurement of the flow in axial flow fans with skewed blades, ASME J. of Turbomachinery, 1999, **121**, 59-66

[6] Yamaguchi N, Tominaga T, and Masutani J: Performance improvement by forward-skewed blading of axial fan moving blades, ISABE 93-7055, 580-589.

[7] Kuchemann D: A simple method of calculating the span and chordwise loading on straight and swept wings of any given aspect ratio at subsonic speeds, A.R.C, R & M No. 2935, 1952.

[8] Thwaites, B. ***Incompressible Aerodynamics***, Oxford: Clarendon Press, Oxford, 1960.

[9] Adamczyk JJ, Celestina ML and Greitzer EM: The role of tip-clearance in high speed fan stall, ASME J. of Turbomachinery, 1993, **115**, 28-39

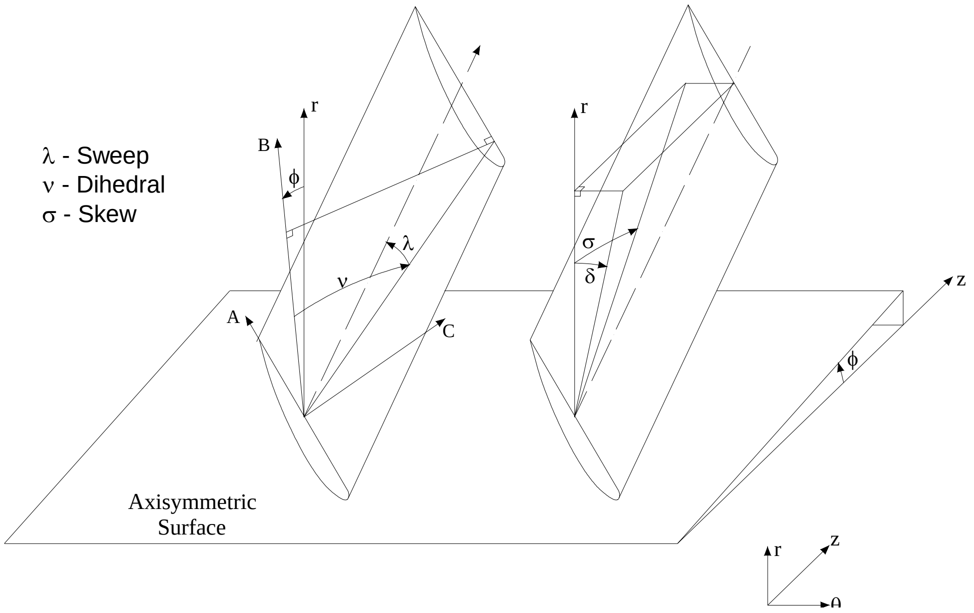

Fig. 1 Sweep, dihedral and skew angles in an axial flow compressor (Beiler and Carolus, (5))

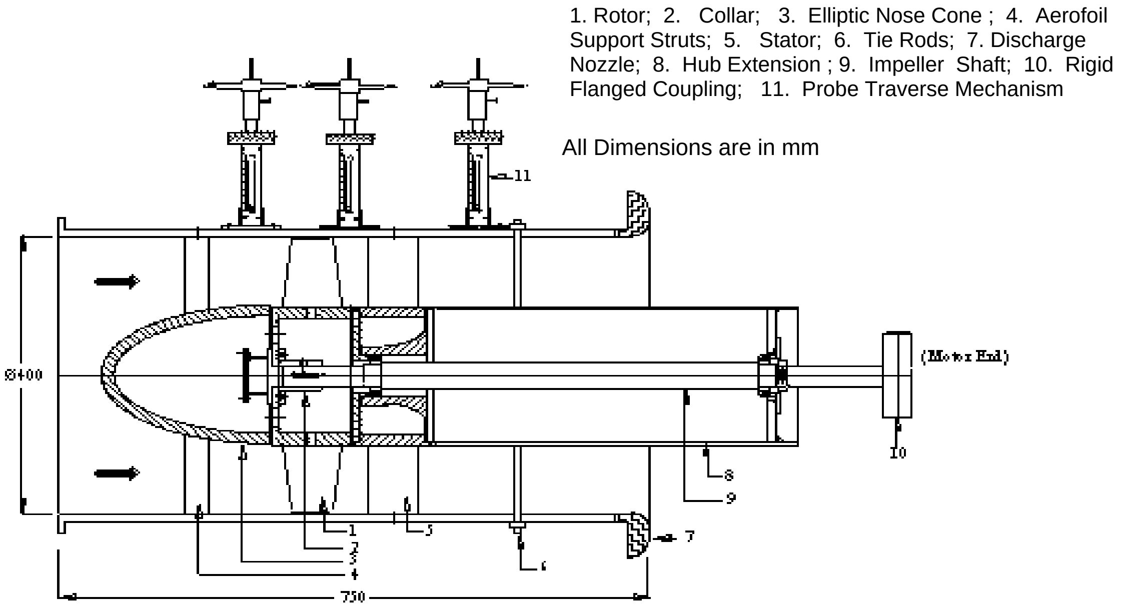
1. Rotor; 2. Collar; 3. Elliptic Nose Cone ; 4. Aerofoil Support Struts; 5. Stator; 6. Tie Rods; 7. Discharge Nozzle; 8. Hub Extension ; 9. Impeller Shaft; 10. Rigid Flanged Coupling; 11. Probe Traverse Mechanism

All Dimensions are in mm

Fig. 2 Schematic of the test set-up

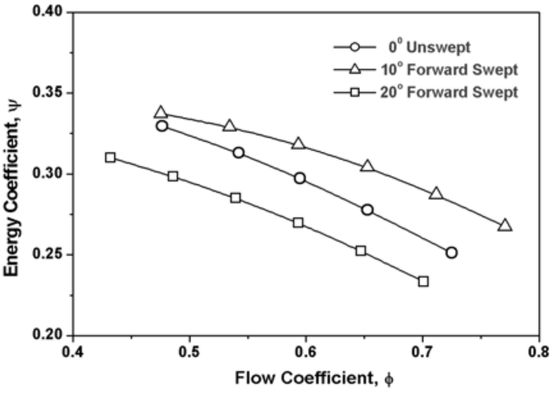

Fig.3 Flow coefficient Vs. energy coefficient

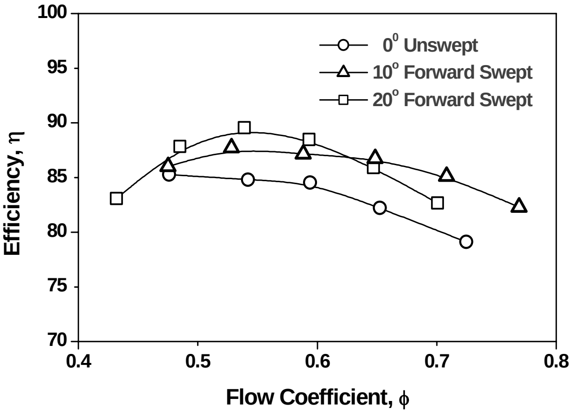

Fig.4 Flow coefficient Vs. Efficiency

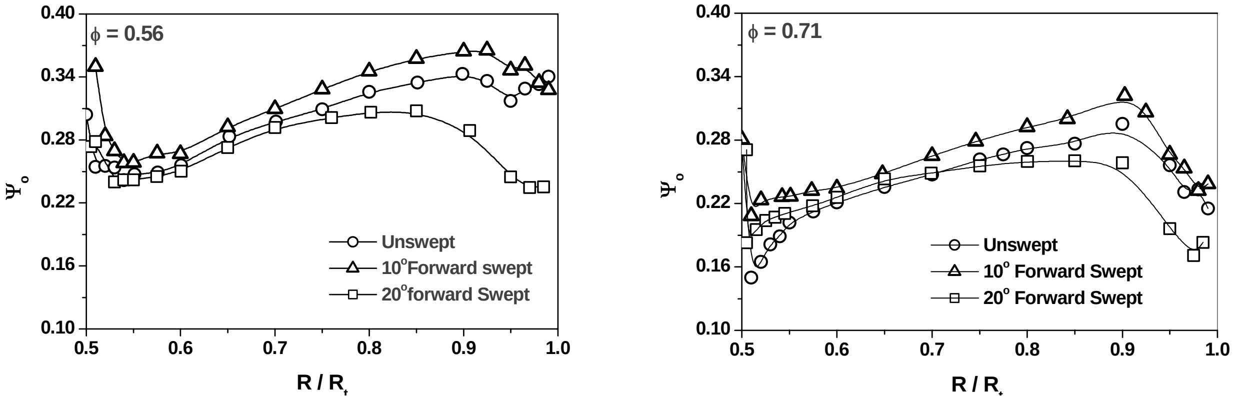

Fig. 5 Variation of total pressure rise coefficient across rotor

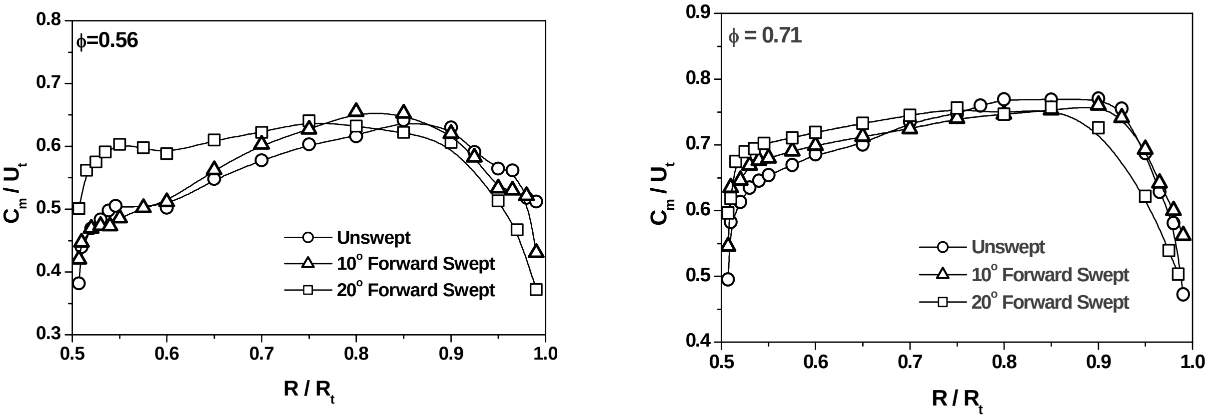

Fig. 6 Variation of axial velocity coefficient at rotor exit

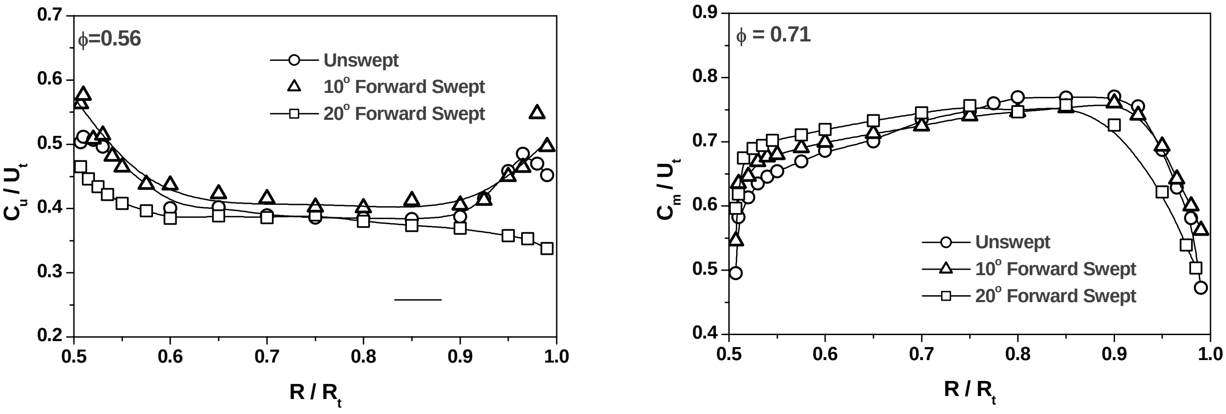

Fig. 7 Variation of tangential velocity coefficient at rotor exit

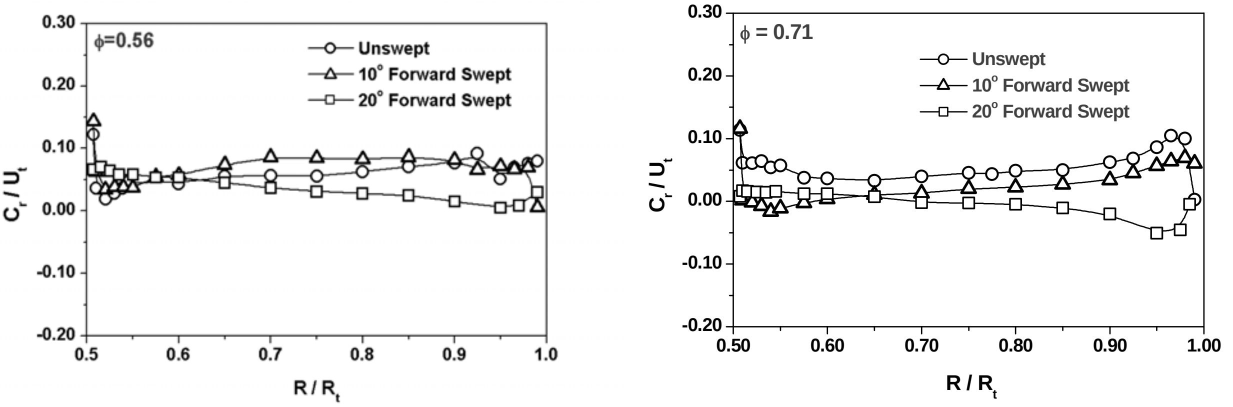

Fig. 8 Variation of radial velocity coefficient at rotor exit

Proceedings of the Tenth Asian Congress of Fluid Mechanics
17-21 May 2004, Peradeniya, Sri Lanka

Up-to-date of the Environment Friendly High Speed Vehicle "Aero-Train" Development

Y. P. Kohama, S. Kikuchi, T. Kato, and F. Ohta
(Institute of Fluid Science, Tohoku University, 2-1-1 Katahira, Sendai 980-8577, Japan)

ABSTRACT Wing in Ground effect vehicle "Aero-Train" which is invented and developed by our group and floats in a U-shape guideway at 500hkm/h with ultra-low energy consumption. We are in the second phase development of the Aero-Train using old MAGLEV (Japanese Linear Motor Car system) test course in the city of Hyuga, Miyazaki prefecture. Presently, we are doing running test using newly developed ART002 model which runs at around 120km/h, floating height of about 5cm. The model is being thrust by two propellers aside driven by 5 kW DC motors. Electricity is fed by the pantograph system equipped at each vertical rear wings and slides along two power cables equipped at each vertical wall. The electricity is generated by solar cells and wind mills equipped at the roof of the center building. Therefore, the Aero-Train system is virtually Zero-Emission high speed vehicle. The details of the research will be presented in the paper.

Key words: Environment friendly technology, Transport system, High speed, Energy minimum, Aerodynamic force, Wing-in-ground effect

1. FEATURE OF THE AERO-TRAIN

Fig.1 Image sketch of the Aero-Train
(3 cars, V=500km/h)

The final goal of an Aero-Train will be 3-car system and glides at about 10 cm off the ground at a speed of 500 km/h. Figure 1 shows the image sketch of the Aero-Train[1]. It has a maximum passenger capacity of 350. The bodies have wings, electric power is gathered from the tips of the vertical left and right wings using a pantograph system, and ducted fans are used for propulsion. The body floats (by wing in ground effect) over a U-shape guideway because the air acts as a cushion supporting the body and wings off the surface, and left and right walls. There is a guideway but no rails, and wheels are only used when starting up and stopping. There are wings but the vehicle cannot fly. It only floats about 10 cm off the ground.

The convenient, comfortable means of high speed transportations human beings have invented so far have all consumed large quantities of fossil or atomic fuels. As a result, they produce large amount of carbon dioxide or radioactive wastes, and exacerbate the problems of global warming and environmental hormones. If things continue like this, it is obvious that our descendants will be deprived of a safe environment in which they can live with peace of mind.”

The aims of present project are: (1) to develop a transportation system running on as little energy as possible; (2) to develop a system allowing composite use of natural energies with a stable supply.

Pelicans and other large birds who are migratory birds and flies such a long distances use the ground effect, that is the air interference between the mountains, ground or water surface and their wings to fly (glide) in a way that consumes little energy. The Aero-train uses the same effect to reduce energy consumption as much as possible. Whereas linear motor cars use magnetic repulsion force, the Aero-train hovers using the air repulsion resulting from this ground effect. The Aero-train can travel on less energy than the “shinkansen” (bullet train), planes or linear motor cars.

In the past, natural energy was overlooked because of the low energy density and changeable nature, but in the future it is necessary to use natural energy effectively. For this reason it is important to develop new systems to collect, store and offer a stable supply of various natural energies.

2. RUNNING TESTS IN MIYAZAKI

Basic research on the Aero-Train was completed in 1998, and running tests to corroborate the concept began in 1999 at the former site of the “Miyazaki Maglev Test Center” owned by JR-Soken (Railway Technical Research Institute; RTRI). We use the abandoned guideway of the linear motor car, which is now tested in Yamanashi Prefecture using new and longer guideway. At first phase, we succeeded in achieving a stable levitated run at 55～85 km/h using a car ART-001 pushing by a car behind2). A new second phase model, called “ART-002”, was completed in January 2002. Test runs with two gasoline engines began in March, followed by tests with a DC motor with nickel-hydrogen cell in July, and a DC motor with lithium-ion batteries in October.

The ART-002 measures 8.4 meters in length and 3.4 meters(0.8m for fuselage) in width, has a chord length of 1.5 meters and a total weight of about 400 kg. Figure 2 shows the

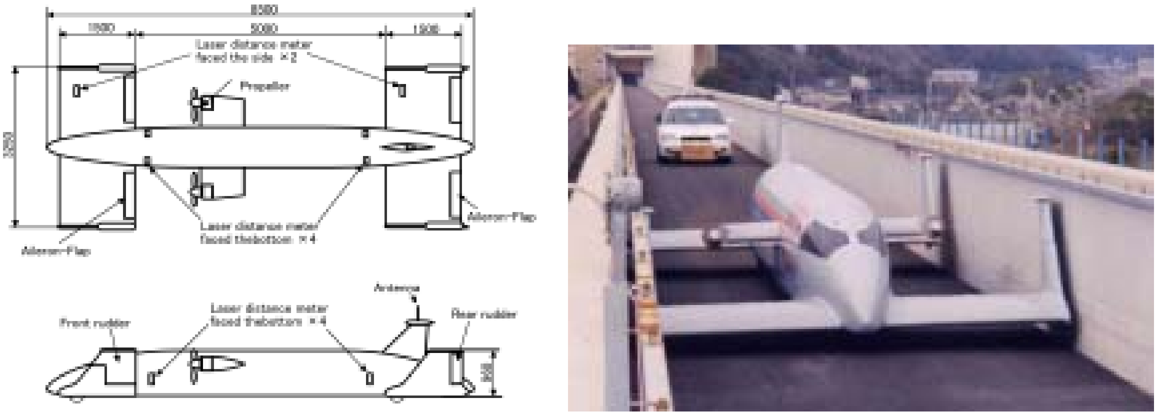

Fig.2 Running test using the second phase model ART002
(V=120km/h, W=400kg)

dimensions in the drawing and the running test picture of the model. Fully autonomous levitated running is achieved at around 120 km/h, about 5 cm off the ground. The drag to lift ratio at present is up to 15.0. The model is 2/7 actual size in terms of the width, about 1/5 actual size in terms of speed. Figure 3 shows the measured data while running. Speed and floating height are set at 120km/h and 5cm. From these data, it is seen that some oscillations in roll and pitch motions. Figure 4 shows the FFT analysis of those data[3]. Peaks at around 0.7 Hz in the case of roll and 2.0 Hz in the case of pitch are seen. Those oscillations might be caused from incomplete control system and program. Therefore, it is needed to develop more accurate and elaborated feed forward control technique.

Another important issue need to be solved is to increase the lift-to-drag ration of the Aero-Train. Presently it is around 15. However, our target is 25 and we need to increase much more. One of the aerodynamic problems is the wing to wing boundary layer interaction as shown in Figure 5. Boundary layer separates at the upper trailing edge region where broken line is drown in the picture. Those separation of the flow seems to be one

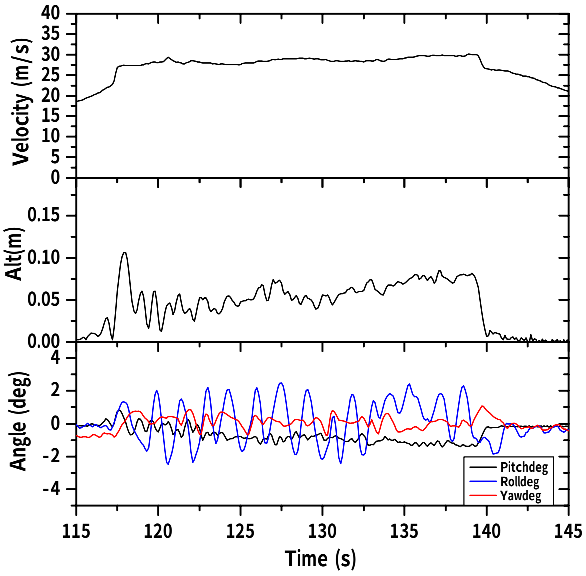

Fig.3 Obtained data during cruise

of the major reason why large aerodynamic drag force exists. Therefore, it is important to control those flow separation actively.

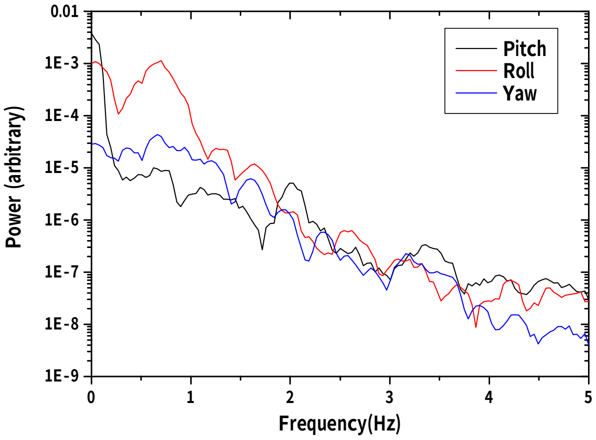

Fig.4 FFT analysis results of the data

3. AIMING AT THE THIRD PHASE DEVELOPMENT AND 2020

In Phase 3 we will completely alter the entire 7-kilometer old test course of the MAGLEV train for the Aero-Train and aim at a top speed of 350 km/h with a passenger capacity of 6. We could accomplish within 5 years if we could get budget for this. However, presently we don’t have any promising offers.

The advantages and problems involved in introducing the Aero-Train as follows. Aero-Train offers ultra-low energy consumption flying. It is safe, a plane that does not crash, a ‘shinkansen’ that does not derail. It is meant as a vehicle that can travel at a speed of 500 km/h with as little energy as possible. In the past the evolution of vehicles has been restricted by the history of technology, and if we evaluate vehicles in terms of the environment they are all fail. One problem of the Aero-train is that active control to reduce horizontal and vertical disturbances generated at high speeds by air repulsion, which is weaker than magnetic repulsion, is still an unknown technology. Furthermore research is currently underway into technology for obtaining electric power from the electric lines on the guideways using a pantograph.

The Aero-train will allow high speed travel at far lower costs than other systems like linear motor car. There are still many issues to be solved before it becomes into reality, but this technology is unique in the world, and the Aero-train is truly the means of land travel we require in 21st century. We hope it will move forward as a national project.

4. GROUND EFFECT

Ground effect is the aerodynamic force which acts to the aerofoil interacted with the ground surface. It can be a plus or minus depending on the attitude of the aerofoil or a body. The minus ground effect(down force) has been used as a matter of course in Formula-1 car racing, but plus ground effect was first used in the field of aircraft. The purpose is to use the ground or water surface effect when flying low so as to save fuel. One famous example is the Ekuranopuran of the former Soviet military. The U.S. military also had a project called “Pelican”. It is reported that a gigantic plane with a transport capacity 7 times that of a 747 could fly on half the fuel at an altitude of 20 to 50 feet (6 to 15 meters). Research on hydro-gliding aero-hydroplanes are currently being conducted in Russia[4)], Germany, U.S. A. and China. Ground effect is the one of possible effect which can be effectively utilized for improving energy efficiency in general energy systems.

5. ENERGY SUPPLY SYSTEM

The Aero-train can be run solely on natural energy. Because energy consumption is extremely low structurally, a truly clean-energy mass transportation system could be established using electricity generated from solar cells and windmills. The idea calls for setting up wind farms along the guideways, covering the guideway's roof entirely with solar panels, and supplying electricity from the vertical wing tips by pantograph. The two lines will be built one on top of the other to reduce land purchasing costs. Hydrogen obtained through electrolysis will be stored under the guideways, and fuel cells will be activated on cloudy days to provide the necessary power. One remaining issue will be a noise problem in the area around the tracks.

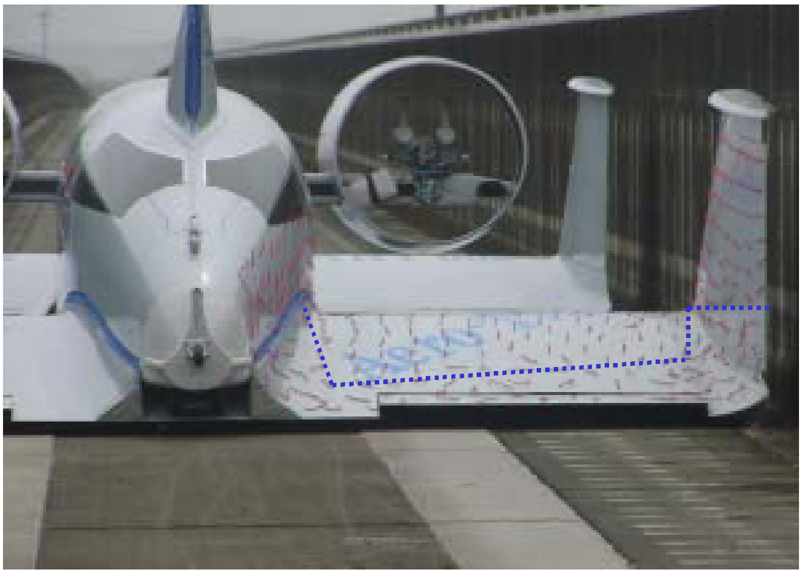

Fig.5 Flow visualization of the rear wing surface by tuft method

6. SUMMARY

We have to do some practical action right away in order to reduce Carbon Dioxide from any energy consuming mechanical systems. Aero-train is one of the answers for such demand. If we could solve technological problem in high speed transport system, which is considered to be a most difficult task, then it is quite sure that we can more easily solve other problems. So, Aero-Train is a kind of symbol for next generation life style.

REFERENCES

1. Y. P. Kohama; Human Friendly High Speed Transportation System and Aerodynamics, Proc. 9 ACFM,30(2001).
2. Yasuaki KOHAMA, et al.; Flight Dynamics and Development of the Stability Control Method of the Aero-Train, J. JSME, B, 68-665(2002), 102-107.(in Japanese)
3. S. Kikuchi, F. Ohta, Y. Kohama; Dynamic Stability Control of the Aero-Train, Proc. 45th. Japan Society for Automatic Control and Measurement, (2002.11.26-27), 7.
4. R. McLeavy; JANE's Surface Skimmers, Hovercraft and Hydrofoils, (1976-77), 136.

Proceedings of the Tenth Asian Congress of Fluid Mechanics
17-21 May 2004, Peradeniya, Sri Lanka

STABILITY AND ACCURACY REQUIREMENTS FOR THE MODELLING OF TOWED UNDERWATER SYSTEMS

S. D. Ranmuthugala
(Australian Maritime College, Launceston, Tasmania, Australia 7250)

ABSTRACT: Investigation of towed underwater bodies generally employ three-dimensional, non-linear, dynamic computer models that are solved using numerical techniques. These models are susceptible to numerical instability and inaccuracies, due to the propagation of numerical and truncation errors through the iteration process. The requirements to avoid the above are investigated and a method to predict an acceptable time interval for the time stepping algorithm of underwater cable system models is developed.

1. INTRODUCTION

Computer modelling is extensively used to investigate underwater towed systems. This requires modelling the cable system, the towed platform(s), and the appropriate dynamic interface. Since the models are non-linear, it is usual to solve them using numerical integration incorporating iterative processes. Similar techniques are used for other underwater cable systems such as mooring systems and petroleum risers. Among the major difficulties encountered by the modeller are numerical instability and inaccuracy. Instability causes the solution process to "blow up", resulting in premature termination of the computer program. Inaccuracy will give erroneous results as well as contributing to instability, as errors entering the calculation will propagate within the solution process

In previous papers[5,6], the author clearly explains the modelling and solution techniques utilised to investigate underwater towed systems. The validation process, which consisted of scaled model tests in a circulating water channel and full-scale trials were also explained. In this paper, for the sake of completion, only brief descriptions of the above are given. The main focus will be the investigation into the numerical stability and accuracy requirements for such models.

2. MODELLING OF THE SYSTEM

Figures 1 and 2 show the basic underwater towed system and the three-dimensional, six degrees-of-freedom (6-DOF) discrete model employed to represent it. The model is capable of representing multi-cable and multi-body systems[5] and allows for the variation of system and environmental parameters. Due to the non-linearities encountered, the cable is modelled by dividing it into a number of discrete segments, which then yields a number of second order differential equations to describe the motion of each segment[6]. The towed fish are modelled in 6-DOF and integrated within the cable solution algorithm to ensure coupling between the fish and the cable system. The author has previously presented detailed description of the mathematical models for two-part and multi tow configurations[6]. The model assumes the distributed mass of the tow cable to be represented by a series of discrete masses separated by weightless, elastic, straight-line segments. The motion of the cable is described by applying Newton's law of motion to each node to give,

$$\underline{F}_i = \underline{\underline{m}}_i \cdot \underline{\ddot{X}}_i \qquad (1)$$

where $\underline{F}$ is the force vector, $\underline{\underline{m}}$ is the mass matrix (including added mass), and $\underline{X}$ is the position vector respectively of element i. These matrices will include the affects of the adjacent cable segments, including tension, net weight, and drag forces. Following the solution technique described in previous publications by the author[6], Eq. (1) can be rearranged to give the linear acceleration of each node as a function of the adjacent tension terms as,

$$\underline{\ddot{X}}_i = (-\underline{P}_i T_{i-1} + \underline{R}_i T_i + \underline{S}_i)/(\Delta t)^2 \qquad (2)$$

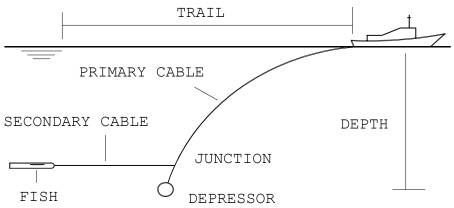

Fig. 1 Two-Part Tow

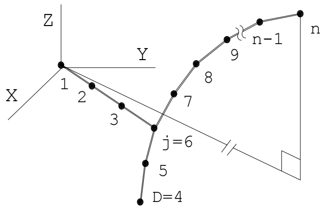

Fig. 2 Lumped Mass Model

The terms T_{i-1} and T_i represent the tensions of the cable segments adjacent to node *i*. Terms $\underline{P}_i$ and $\underline{R}_i$ represent the coefficients of the above tensions respectively, while $\underline{S}_i$ represents all other forces. The fish is modelled with 6-DOF[6] in the following form in order to describe its position and attitude.

$$\begin{bmatrix} \underline{F}_f & \underline{F}_f \end{bmatrix}^T = \underline{\underline{m}}_f . \begin{bmatrix} \ddot{x} & \ddot{y} & \ddot{z} & \ddot{\beta} & \ddot{\alpha} & \ddot{\gamma} \end{bmatrix}^T \tag{3}$$

where $\underline{M}$ is the moment vector, x, y, z are the displacements, and α, β, γ are the angular displacements of the fish *f*. Manipulation of Eq. (3) allows its conversion to a form similar to that of Eq. (2), thus enabling the fish model to be integrated into the cable model during the solution phase[6].

3. SOLUTION TECHNIQUE

The quasi-static solution of the system is an ideal starting point for the dynamic analysis. Using the values obtained from the quasi-static model as initial values at time *t*, the dynamic model is solved to the dynamic boundary conditions during each time interval of Δt. Numerical integration methods are used to solve in the time domain, the nonlinear differential equations describing the motion of the system. A multi-step implicit finite difference algorithm known as the Houbolt scheme[1] is used to describe approximately the positions and velocities of the nodes at time $t+1$ as,

$$\dot{\underline{X}}^{t+1} = (11.\underline{X}^{t+1} - 18.\underline{X}^{t} + 9.\underline{X}^{t-1} - 2.\underline{X}^{t-2}) / 6.\Delta t$$

$$\underline{X}^{t+1} = 2.5.\underline{X}^{t} - 2.\underline{X}^{t-1} + 0.5.\underline{X}^{t-2} + 0.5.(\Delta t)^2.\ddot{\underline{X}}^{t+1} \tag{4}$$

The tentative accelerations for Eq. (4) are obtained from the equations of motion for the nodes, *i.e.* Eq. (2). This in turn uses the static segment tension values as initial tentative tensions. These tentative segment tensions can then be corrected by using a Newton-Raphson iteration process, based on the constraint equation of each segment length. The latter gives the segment length error (*ER*) as,

$$ER_i^{t+1} = (x_{i+1}^{t+1} - x_i^{t+1})^2 + (y_{i+1}^{t+1} - y_i^{t+1})^2 + (z_{i+1}^{t+1} - z_i^{t+1})^2 - \{ l_i^2 .(1 + (T_i^{t+1} / A_i .E))^2 \} \tag{5}$$

where *A* and *E* are the cable's cross-sectional area and the modulus of elasticity respectively. The tentative tension values need to be corrected to reduce the length error term (*ER*) to zero. Since the coordinates of a node are a function of the tensions of the adjacent cable segments, the length error of that segment is a function of the tensions of that cable segment and the two segments adjacent to it. Thus, expanding Eq. (5) as a function of the tensions in a Taylor series[6] gives,

$$ER_i^{t+1} = ER_i^{t+1} + \frac{\partial ER_i^{t+1}}{\partial T_{i-1}^{t+1}}.\delta T_{i-1}^{t+1} + \frac{\partial ER_i^{t+1}}{\partial T_i^{t+1}}.\delta T_i^{t+1} + \frac{\partial ER_i^{t+1}}{\partial T_{i+1}^{t+1}}.\delta T_{i+1}^{t+1} + higher \quad order \quad terms = 0 \tag{6}$$

$$\underline{\underline{ET}}_i^{t+1} . \underline{\underline{\delta T}}_i^{t+1} = \underline{\underline{ER}}_i^{t+1} \tag{7}$$

where matrices [*ER*] is the cable segment error, [δT] the tension correction, and [*ET*] the tension error, with the higher order terms neglected. This is reduced to a set of recursive linear equations by elimination and the tentative tensions are then updated, with the process repeated until convergence.

4. STABILITY ANALYSIS

Given the long simulation time required for dynamic time domain cable system models, the mathematical model and the solution technique must be sufficiently accurate and stable. The errors that can enter during the integration process are divided into two categories. The first is the truncation error, which is the difference between the exact solution of the partial differential equations and the exact solution of the difference equations. The second is the numerical (round off) error, which is the difference between the exact solution of the difference equations and the numerical solution of the difference equations. Generally the former is much larger than the latter, and is usually responsible for the stability issues encountered in numerical schemes.

Usually all implicit time integration schemes are unconditionally stable, while explicit schemes are only conditionally stable. Therefore, explicit schemes require a time step that is ***less*** than a defined critical value, while the implicit schemes have no limiting time step. However, when using implicit schemes for non-linear systems, large time steps will cause the numerical integration scheme to "blow out", *i.e.* become unstable. The reason for this is the truncation error introduced by the required iteration scheme. Thus, the selection of the time step is dependent on the accuracy and stability of the numerical scheme. Therefore, the time step should be sufficiently small to ensure accuracy and stability, but large enough to prevent long simulation times.

There are two basic approaches to investigate the dynamics of structures *i.e.* the direct integration of the equations of motion and the modal analysis. In the former, the equations are integrated using a numerical step-by-step procedure, the term ***direct*** implying that prior to this procedure the equations are not transformed in any manner. The solution procedure utilised to solve the tow model is of this type. The latter approach consists of changing the basis from the element coordinate basis to an eigenvector basis, associated with the natural frequencies (or eigenvalues) of the undamped problem. Thus, it generates an alternate set of equations that can be integrated more efficiently by a direct integration scheme, than the unmodified equations of motion. It reasons that if the modal form and the unmodified equations are integrated using the same scheme, the results should be the same. Therefore, it is possible to analyse the modal form of the equations to determine the accuracy and stability of the direct integration scheme. Consider the general cable equation of motion given by:

$$\underline{\underline{m}}\,\underline{\ddot{X}} + \underline{\underline{c}}\,\underline{\dot{X}} + \underline{\underline{k}}\,\underline{X} = \underline{F} \tag{8}$$

where $\underline{\underline{m}}$, $\underline{\underline{c}}$, and $\underline{\underline{k}}$ are the cable element mass, damping, and stiffness matrices respectively. The set of equations represented by Eq. (8) is assembled for a discrete system by superposition of the equations representing each individual node. If the number of nodes in the system is n, then the matrices in Eq. (8) will be square matrices of the n^{th} order, while the vectors will be column matrices of a similar order. Equation (8) is transformed to the eigenvector basis by solving the generalised eigenproblem, which gives it in modal form as,

$$\underline{\ddot{X}}_m + 2\,\zeta\,\omega_n\,\underline{\dot{X}}_m + \omega_n^2\,\underline{X}_m = \underline{F} \tag{9}$$

where $\underline{X}_m$ is the time dependent modal displacement vector, ω_n is the natural frequency, and ζ is the damping ratio. This requires only the variables ω_n, ζ, and Δt to be considered in the analysis, and not the complete stiffness and mass matrices. In light of the solution characteristic of the direct integration method, it is required to estimate the integration error in the solution of Eq. (9) as a function of $\Delta t / t_{n,min}, \zeta, \text{ and } \underline{F}$, where $t_{n,min}$ is the minimum natural period of the cable mesh. Note: it is the time ratio $\Delta t / t_{n,min}$, (*i.e.* the ratio between the time step and the minimum natural period of the cable mesh), and not the absolute time step that governs the criteria for stability and accuracy.

As stated previously, the integration of the modal form and the unmodified equations using the same scheme should give the same result. Therefore, by analysing the modal form of the equations it is possible to determine the accuracy and stability of the direct integration scheme.

Numerical stability depends not on the original set of equations, but on the numerical scheme used. Stability requires that the amplification of any errors entering the solution process should be limited. One method to estimate the stability of the solution technique employed for Eq. (9) is the use of the amplification matrix and the load operator[1,2]. These will depend on the integration scheme used in the solution, and are generally defined as,

$$\underline{R}^{t+1} = \underline{\underline{A}}\,\underline{R}^{t} + \underline{\underline{L}}\,\underline{F}^{t+1} \tag{10}$$

where $\underline{R}$ is a vector storing the solution quantities, (*e.g.* displacements, velocities, *etc.*), $\underline{\underline{A}}$ is the amplification matrix, and $\underline{\underline{L}}$ is the load operator. Since the load operator will not influence the numerical stability of the scheme, the analysis is carried out with no external load, thus Eq. (10) reduces to,

$$\underline{R}^{t+1} = \underline{\underline{A}}\,\underline{R}^{t} \tag{11}$$

Inspection of Eq. (11) reveals that it is possible to recursively calculate the solution at any time as,

$$\underline{R}^{t+m} = \underline{\underline{A}}^{m}\,\underline{R}^{t} \tag{12}$$

where superscript m represents the number of time intervals, *i.e.*, $t^{t+m} = t^{t} + (m.\Delta t)$.The amplification matrix for the integration scheme is derived using spectral decomposition, resulting in,

$$\underline{\underline{A}} = \underline{\underline{P}}\,\underline{\underline{J}}\,\underline{\underline{P}}^{-1} \tag{13}$$

where $\underline{\underline{P}}$ is the matrix of eigenvectors of $\underline{\underline{A}}$, and $\underline{\underline{J}}$ is the Jordan form of $\underline{\underline{A}}$, with its eigenvalues along its diagonal. This gives a recursive relationship for the amplification matrix as,

$$\underline{\underline{A}}^{m} = \underline{\underline{P}}\,\underline{\underline{J}}^{m}\,\underline{\underline{P}}^{-1} \tag{14}$$

From Eq. (14) it is possible to deduce the requirements for $\underline{\underline{A}}$ to remain bounded, as “m” increases, *i.e.*, $\underline{\underline{A}} \rightarrow 0 \quad as \quad m \rightarrow \infty$. This occurs if the ***spectral radius*** ($p(\underline{\underline{A}})$, *i.e.* the maximum absolute value of the eigenvalues of $\underline{\underline{A}}$), is equal to or less than one, *i.e.*,

$$p(\underline{\underline{A}}) \leq 1 \tag{15}$$

Thus, for the stability of the integration method employed, ***the spectral radius of the amplification matrix should be equal to or less than one***. It should also be noted that, smaller the spectral radius, more rapid is the convergence of the integration scheme. Now consider the Houbolt scheme given by Eq. (4). Substituting them in Eq. (9) gives the recursive relationship inclusive of the amplification matrix as,

$$\begin{bmatrix} \underline{X}_m^{t+1} \\ \underline{X}_m^{t} \\ \underline{X}_m^{t-1} \end{bmatrix} = \underline{\underline{A}} \begin{bmatrix} \underline{X}_m^{t} \\ \underline{X}_m^{t-1} \\ \underline{X}_m^{t-2} \end{bmatrix} + \underline{\underline{L}}\,\underline{F}^{t+1} \tag{16}$$

where

$$\underline{\underline{A}} = \begin{bmatrix} \dfrac{5\,\alpha_p}{\omega_n^2\,\Delta t^2} + 6\,\beta_p & -\dfrac{4\,\alpha_p}{\omega_n^2\,\Delta t^2} - 3\,\beta_p & \dfrac{\alpha_p}{\omega_n^2\,\Delta t^2} + \dfrac{2\,\beta_p}{3} \\ 1 & 0 & 0 \\ 0 & 1 & 0 \end{bmatrix},$$

$$\underline{\underline{L}} = \begin{bmatrix} \dfrac{\alpha_p}{\omega_n^2} & 0 & 0 \end{bmatrix}^T, \quad \alpha_p = \left(\frac{2}{\omega_n^2\,\Delta t^2} + \frac{11\,\zeta}{3\,\omega_n\,\Delta t} + 1 \right)^{-1}, \text{ and } \beta_p = \frac{\zeta\,\alpha_p}{\omega_n\,\Delta t}$$

The stability condition for the Houbolt scheme is measured by obtaining the spectral radius of the amplification matrix $\underline{\underline{A}}$ given above. Thus, it is required to calculate the eigenvalues of $\underline{\underline{A}}$. A plot of the spectral radii versus the time ratio $\Delta t / t_{n,min}$ for the Houbolt scheme assuming no damping is given in Fig. 3. It is seen from this figure that the spectral radius is less than “1” for all values of $\Delta t / t_{n,min}$. Therefore, the Houlbolt scheme is deduced to be unconditionally stable. Inspection of these curves shows that as $\Delta t / t_{n,min}$ increases, the spectral radius rapidly reduces, highlighting a fast rate of convergence. Note: although the inclusion of damping will change the shape of the curve, it does not significantly change the stability characteristics at low damping ratios.

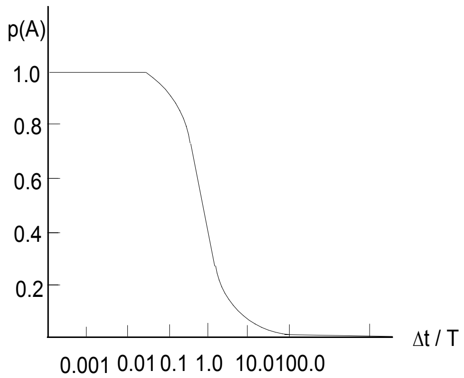

Fig. 3 Spectral Radii of the Houbolt Scheme with $\zeta = 0$

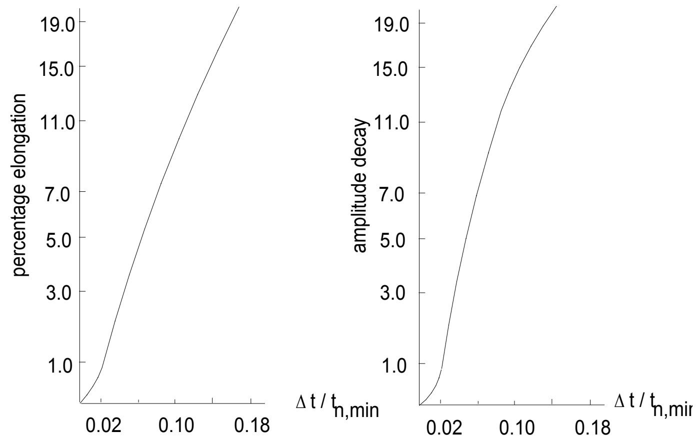

Fig. 4 Accuracy Parameters of the Houbolt Scheme

The forgoing stability analysis was based on the system being linear. However, we know that the mathematical model for the towed cable system is non-linear, *i.e.* the coefficients of the equations of motion will change with time. Since the Houbolt scheme is unconditionally stable, it can be successfully used to solve the non-linear underwater tow model. As in linear systems, the Houbolt scheme being implicit, considers the equilibrium of the system at the "next" time step, *i.e.* at $time = t+1$. However, since the system is non-linear, an iterative process is required to solve the equations for each time step. The iterative process used here is the Newton-Raphson iteration scheme. This is a **predictor-corrector** method, as the values predicted from the system equations are repeatedly corrected until convergence is achieved.

Two criteria that affect such iteration schemes are the selection of a correct *convergence tolerance*, (which is the difference between the exact solution of the difference equation and the accepted solution), and the *truncation error*, (which is due to neglecting the higher order terms of the Taylor series expansion). Either one will introduce errors into the iteration process, that may grow during the integration, resulting in inaccuracies and/or stability problems. Consider the solution technique outlined previously. The correction terms for the iteration process are obtained by expanding Eq. (5) in a Taylor series to yield Eq. (6). It is assumed that the tentative values of the tow configuration are sufficiently close to the solution, thus enabling the higher order terms to be neglected. This is acceptable, if the time step is sufficiently small, as the solution of the previous time step (*i.e.* t) is used as the tentative values for the current time step, (*i.e.* $t+1$). However, if the time step is large, then the higher order terms cannot be neglected, as the error thus introduced may cause the iteration process to "blow up". A similar situation occurs if the forcing function is large, as the changes during the time step are considerable.

It is possible to increase the accuracy by including some higher order terms into the process. For example, the second order terms can be calculated by further differentiating Eq. (5) with respect to the tensions of the relevant cable segments. However, the additional computation introduced does not offer a significant advantage over the use of a smaller time step with a solution scheme without the higher order terms. In general, the stability of implicit numerical schemes utilised for non-linear systems can be maintained by using a sufficiently small time step. The limiting condition for the time step has been investigated through experience and testing of practical schemes by a number of researches[1,2,7], and is predicted as,

$$\Delta t \le t_{n,min} / 10 \qquad (17)$$

5. ACCURACY ANALYSIS

The accuracy of the numerical schemes is measured for the solution using two criteria, *i.e.* the **period elongation** and the **amplitude decay**. These give the deviation of the numerical solution against the exact solution, and Fig. 4 shows these parameters for the Houbolt scheme. They indicate that the accuracy is good at low $\Delta t / t_{n,min}$, *i.e.* when the condition given by Eq. (17) is met. As stated previously, the integration of the unmodified equations and their modal form, both using the same scheme should give the same result. Therefore, by analysing the modal form, (*i.e.* Eq. (9)), it is possible to determine the accuracy of the direct integration scheme. Inspection of Eq. (4) reveals that the Houbolt scheme is a three-step scheme. Therefore, using the general expression for multi-step integration schemes, Eq. (9) is replaced by the following 3-step algorithm.

$$\sum_{t=0}^{3}\left(\alpha^{t}\,\Delta t^{-2} + 2\,\gamma^{t}\,\zeta\,\omega_{n}\,\Delta t^{-1} + \beta^{t}\,\omega_{n}^{2}\right)R^{m+t} = 0 \qquad (18)$$

where the terms α^t, β^t, and γ^t are given in reference (6). The truncation error is obtained by using the exact solution of Eq. (9) in the integration scheme given by Eq. (18). Substituting and solving the resulting characteristic polynomial of the 3-step algorithm yields the error terms as,

$$2\delta_{p}\omega_{n}Sin\,\nu = \left(\delta_{a}^{2} - \delta_{p}^{2}\right) + 6\omega_{n}^{2}\Delta t\left\{\delta_{a}Cos^{2}\nu - \delta_{a}Cos2\nu + \delta_{p}Sin2\nu - \delta_{p}Cos\,\nu.Sin\,\nu\right\} + O\left(\Delta t^{2}\right) \qquad (19)$$

$$2\delta_{a}\omega_{n}Sin\,\nu = -2\delta_{a}\delta_{p} + 6\omega_{n}^{2}\Delta t\left\{\delta_{p}Cos2\nu - \delta_{p}Cos^{2}\nu + \delta_{a}Sin2\nu - \delta_{a}Cos\,\nu.Sin\,\nu\right\} + O\left(\Delta t^{2}\right) \qquad (20)$$

where δ_a is the amplitude error, δ_p is the phase error, and $O(\Delta t^2)$ is the asymptotic notation of the error having an order of two. Inspecting Eqs. (19) and (20) shows that the error terms δ_a and δ_p are of order Δt^2. Therefore, it is stated that the ***amplitude and phase errors are*** $\boldsymbol{O(\Delta t^2)}$. The actual expressions for the respective error terms can be obtained by solving the above equations. It can be showed that stability issues occur, if a higher order accuracy is pursued[7]. Therefore, as shown in Fig. 4, errors in the order of $O(\Delta t^2)$ are acceptable providing the time step is relatively small, *i.e.* as defined by Eq. (17). Thus, for the numerical integration of the non-linear tow model, the time step should be smaller than one tenth of the smallest natural period of the cable mesh to ensue acceptable accuracy.

6. CONCLUSION

In practice, a simpler and quicker method to estimate an appropriate time step for the dynamic simulation of the tow model is desirable. By using the longitudinal wave speed obtained from the continuous cable model[4,6] a guide to select an appropriate time step for the time domain simulation is obtained as in Eq. (21), which used in existing models by the author has shown that the required accuracy is obtained without causing the programs to "blow up". (Note: ρ is the density of the cable material).

$$\Delta t \le (l_{min}/10).\sqrt{\rho / E} \qquad (21)$$

Computer modelling is a major tool in the investigation of underwater cable systems, including towed systems. Due to the non-linearities, these models are solved using numerical techniques incorporating iterative processes. The resulting instability and inaccuracy problems have for decades been a "thorn in the side" of researches of cable systems. This study has attempted to investigate the reasons for such problems, and has led to the prediction of a time step that can be used by operators to minimise instability and inaccuracy problems in underwater dynamic cable models.

REFERENCES

[1] Bathe KJ. Finite Element Procedures in Engineering Analysis. Prentice-Hall Inc, New Jersey, 1982.

[2] Hearn GE and Thomas DO. The Influence of Practical Time Integration Schemes on Dynamic Mooring Line Analysis. Proceeding from the 23rd Offshore Technology Conf., Houston, May 1991. 397-409

[3] Huang S. Dynamic Analysis of Three Dimensional Marine Cables. J Ocean Engineering, 1994. Vol 21, No 6, 587-605.

[4] Ractliffe AT. Dynamic Response of Flexible Catenary Risers. International Symposium on Floating Production Systems, RINA, London, March, 1984.

[5] Ranmuthugala, S.D. Modelling and Related Numerical Stability Requirements of Underwater Towed Bodies, Proceedings of the Int. Conf. on Shallow Survey 99, Sydney, 1999.

[6] Ranmuthugala SD. Modelling and Related Numerical Stability Criteria of Underwater Two-Part and Multiple Towed Systems. Final Report, Task D2, Australian Maritime Engineering CRC, Launceston, June 2000.

[7] Wood, WL. Practical Time-Stepping Schemes, Clarendon Press, Oxford, 1990.

Proceedings of the Tenth Asian Congress of Fluid Mechanics
17-21 May 2004, Peradeniya, Sri Lanka

The use of Curved Bodies in a Wind Tunnel to model Bodies in a Steady Turn

P. A. Gregory[1], P. N. Joubert[2] and M. S. Chong[2]

([1]Defence Science and Technology Organisation
Melbourne, Victoria, 3207 AUSTRALIA)
([2]Department of Mechanical and Manufacturing Engineering,
University of Melbourne, Victoria, 3010 AUSTRALIA)

ABSTRACT: RANS simulations of a body performing a steady turn and a deformed body in rectilinear flow are compared. The deformed body is curved so as to preserve that change in angle of attack along the body that occurs when a straight body moves through curved streamlines. RANS results for two different turn radii show good agreement between the two cases for measurements of forces and moments on the body. The effect of introducing a velocity gradient upstream of the curved body (to preserve the change in velocity due to a change in radius) causes an increase in forces and moments. In theory, introducing this velocity gradient is essential for maintaining flow similarity between the two cases and should improve the solution. Analytical methods to determine the fluid acceleration effects (which are present in the first case but not in the second) are presented.

1 INTRODUCTION

The use of deformed bodies to examine the flow over bodies in a steady turn first began in the 1930s. Gurzhienko [2] used it to measure forces and moments on airship hulls, as did Von Karman. Gurzhienko's methods were used by Chang and Purtell[1] to provide an experimental validation for a numerical method to predict the forces on a turning body and to examine the flow separation created by this body.

Conventional methods to investigate the flow separation of a body in a steady turn usually rely on a rotating-arm apparatus, which was used by Lloyd[5] in his extensive study on vorticity measurements from a body of revolution in a steady turn. Another approach used to investigate the flow separation caused by a manoeuvring body is to rely on a dynamic plunge/pitch mechanism to create an unsteady manoeuvre. Much work has been carried out by Simpson, Wetzel, Hoang and Hosder ([7],[3],[4]) at the University of Virginia using such an apparatus. They have conducted extensive measurements on both the surface and wake flow created by prolate spheroids and generic submarine body shapes in an unsteady manoeuvre.

The use of curved bodies was proposed by P. N. Joubert to examine the flow over a body of revolution in a steady turn, but without the need for complicated apparatus such as a rotating arm or a large turning basin. This enables the body to be examined in a conventional wind tunnel, and since the body is now stationary, flow measurement becomes significantly easier.

By using this method, we have moved from a body accelerating through a stationary fluid to a stationary body placed in a steady rectilinear flow. The effects of the fluid acceleration on the flow behaviour must be accounted for if the method of curved bodies is to be used with confidence.

2 TRANSFORMING EQUATIONS

The full derivation of the transforming equations can be found in Gurzhienko[2]. The essence of the transformation is the requirement to keep the change in angle of attack β along the body centreline identical in both cases. As this change in β depends on the curvature of the streamlines, it becomes necessary to construct a different deformed body for each turn radius investigated. Our situation involves a body of length L performing a turn around radius R_0, whose centre of mass is moving with velocity V_0 and is aligned at an angle of attack β_0 to the flow (see Figure 1). Along the centreline $\overline{BD}$ the angle of attack varies from zero (denoted as the *pivot point*) at B, to β_0 at the aerodynamic centre, and to some value β at D. We wish to deform the body such that placing it in a recitilinear flow will preserve this change in angle of attack.

The right-hand side of Figure 1 shows such a body placed in straight streamlines. Note that a velocity gradient equal to $V = \omega/R$ must be placed upstream of the curved body to maintain that change in velocity due to the increasing radius that the body experiences in a steady turn. The equation of the centreline of the body is :

$$z' = R_0 \cos\beta_0 \left[\cosh\left(\frac{x}{R_0\cos\beta_0}\right) - 1\right] \tag{1}$$

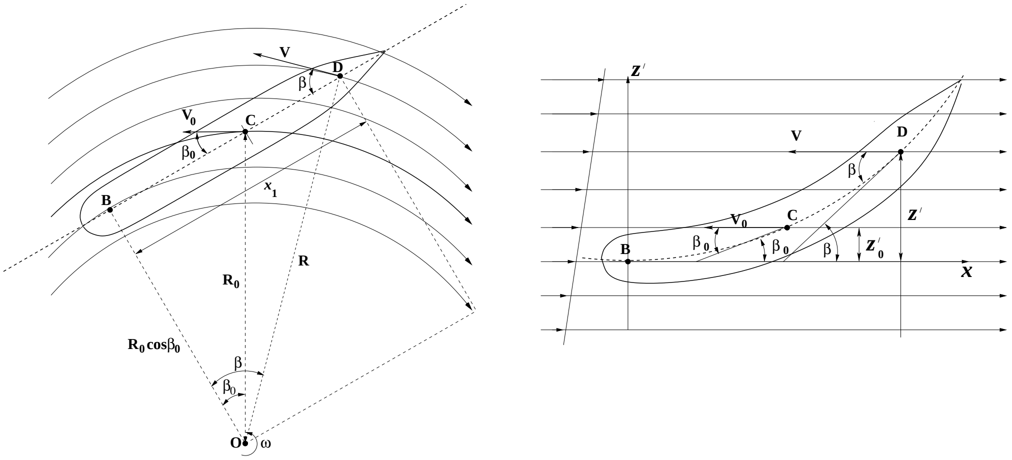

Figure 1: Body of revolution turning about point O, and the corresponding deformed body placed in rectilinear flow.

Gurzhienko also derived equations which define the deformed cross-sections passing through point D as :

$$z' = x_1 \left[\cosh\left(\frac{x - x_D}{x_1} - \operatorname{arcsinh}\frac{1}{nx_1}\right)\right] - \frac{1}{n} \tag{2}$$

where $n = R_o \cos\beta_0$. The equation for the velocity gradient in the rectilinear flow case is :

$$v = v_o \left(1 + \frac{z'}{R}\right) \tag{3}$$

3 NUMERICAL METHOD

Two cases were examined. In the first, a tight turn was simulated, with turn radius $R = 3L$. In this case, the pivot point was located at the nose (so $\beta = 0$ at $x/L = 0$), and $\beta_0 = 8.7°$.

The second case examined a more gentle turn, with $R = 5L$, with the pivot point located at $x/L = 0.2$. For this instance, $\beta_0 = 2.9°$.

All results were obtained using the commercial RANS code FLUENT with the two-equation $k-\omega$ model. The modified Shear-Stress-Transport (SST) version of this model was used. The transitional flows option was used, which requires the mesh near the surface to be fine enough so that the flow in the boundary layer can be computed all the way to the wall. A second-order discretisation scheme was used to solve for momentum, pressure and turbulence quantities.

A hybrid-meshing scheme was used. The surface of the body was decomposed into logical squares so that a hexahedral mapping scheme could be used in the near field region (roughly twice the model diameter in width). This mapping scheme facilitated the construction of a very fine mesh close to the body to resolve the boundary layer. From this hexahedral region, tetrahedrons were used to to fill the rest of the flow domain.

4 RESULTS

4.1 R = 3L

For $Re = 7.8 \times 10^6$, the average forces and moments about the centroid for the bodies are:

	C_D	C_L	C_M
Steady Turn	0.119	0.0235	0.0660
Rectilinear	0.0961	0.0235	0.0747
Rectilinear (with shear)	0.135	0.0309	0.0728

Table 1: Force and moment coefficents for $R = 3L$.

In both cases, the value of drag for the curved body varies by more than 10% compared to the straight model, as does the computed value of the moment about the y axis. In the case of computed lift coefficients, the curved model is within 1% of the straight model, while adding the velocity gradient results in almost a 30% increase in C_L.

Plots of surface static pressure at cross sections along the body shown in Figure 2 show good agreement along the length of the body for the straight body and the curved body. Adding the velocity gradient to the rectilinear flow case creates a noticeable difference in the variation in C_p across the body.

Plots of streamwise vorticity shown in Figure 3 show the structure of the off-body vortex produced by the cross-flow separation. The size of the vortex is very similar for the straight body and for the curved body. Introducing the velocity gradient slightly reduces the size and strength of the vortex at $x/L = 0.9$.

Pictures of the surface streamlines in Figure 4 for each body (obtained by integrating the x, y and z components of wall-shear stress) show that the surface flow and three-dimensional separation lines are very similar in all cases. Both feature two separation lines, and local topology that is consistent with that identified by Wetzel and Simpson[7]. Note that introducing the velocity gradient shows no visible change in the streamline pattern.

4.2 R = 5L

For $Re = 7.8 \times 10^6$, the average forces and moments about the centroid for the bodies are :

Co-ord. system	C_D	C_L	C_M
Rotating	0.121	0.00507	0.0238
Rectilinear	0.119	0.00618	0.0281
Rectilinear (with shear)	0.127	0.00627	0.0280

Table 2: Force and moment coefficents for $R = 5L$.

Computed values of C_D for the curved bodies are within 5% of the value for the straight body. Values of C_L are in both cases are greater than 20 %, whilst the error between the values for C_M are of similar magnitude to the previous case $R = 3L$.

The surface pressure distribution in this case show similar trends to the corresponding case for $R = 3L$ with respect to the three cases considered. The radial pressure gradient for this turn radius is less severe than for $R = 3L$.

Plots of streamwise vorticity showed the same trends to the previous case, except the size and strength of the off-body vortex was reduced.

Pictures of the surface streamlines in Figure 5 for each body show similar surface topology to the previous case. Since the angle of attack for the case is less than for $R = 3L$, the size of the separation lines are signficantly smaller, indicating a smaller region of cross-flow separation as expected. As with the previous case, the introduction of the velocity gradient does not effect the flow pattern.

5 DISCUSSION

Munk [6] used simple momentum analysis to attempt to compute the forces on a slender body of revolution in a steady turn moving through a perfect fluid. These equations were then used to predict the applied bending moment to an airship hull.

Munk showed that the equations for the transverse force (in this case lift) and longitudinal force (drag) were :

$$F_{lift} = \frac{K_1 \rho \cos(\beta) V^2}{r} \tag{4}$$

$$F_{drag} = \frac{K_2 \rho \sin(\beta) V^2}{r} \tag{5}$$

whilst the moment about the aerodynamic center was equal to :

$$M = \frac{1}{2}(K_2 - K_1)\rho \sin(2\beta) V^2 \tag{6}$$

Here $K_1\rho$ and $K_2\rho$ refer to the added masses in the longitudinal and transverse direction. For our body with $L/D = 9.9, K_1 = 0$, computing these equations for our flow case gives the data shown in Table 3. The values for C_D vary between 30-100 % when compared to computed values for the body in a steady turn. The values of C_M vary by an order of magnitude.

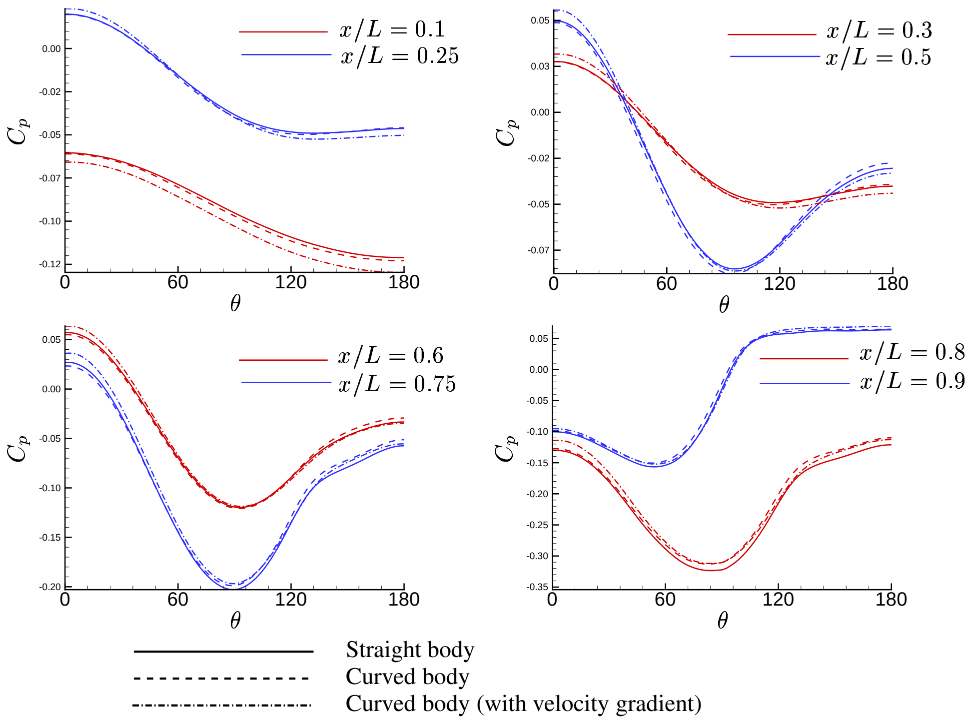

Figure 2: Plots of C_p vs θ at various x/L for $R = 3L$.

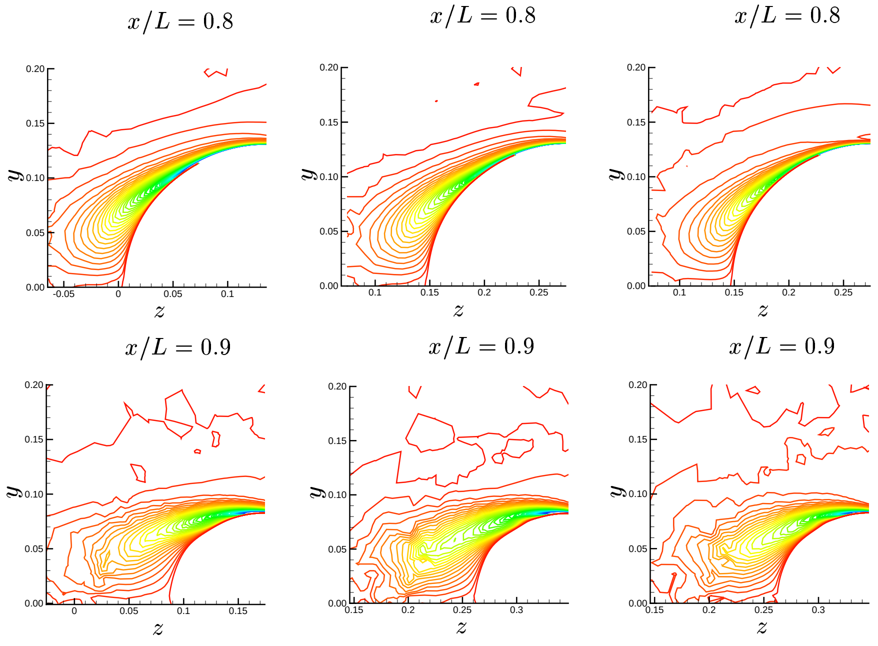

Figure 3: Contour plots of streamwise vorticity for straight body (left), curved body (centre) and curved body with velocity gradient (right), at various x/L for $R = 3L$. The value of vorticity ranges from -1500 to 0 s^{-1}

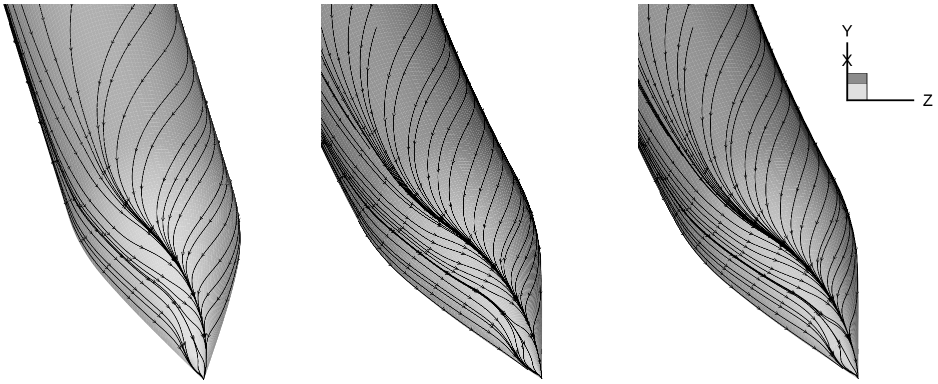

Figure 4: Surface flow patterns for straight body (left), curved body (center) and curved body with velocity gradient(right) for $R = 3L$

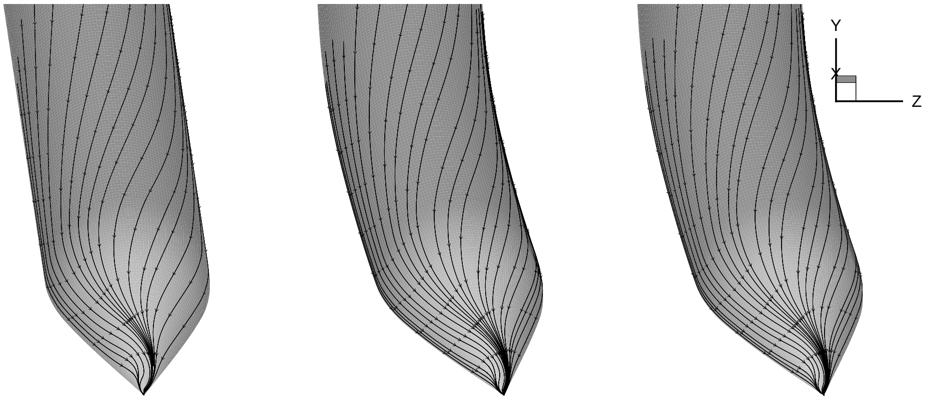

Figure 5: Surface flow patterns for straight body (left), curved body (center) and curved body with velocity gradient (right) for $R = 5L$

5.1 Effect of centrifugal forces

Munk also attempted to quantify the effect of the centrifugal forces on the airship hull and its contribution to the bending moment. Continuing with his simple analysis, Munk showed that the transverse force distribution along an airship was equal to :

$$dF = dx \left[(k_2 - k_1) \frac{dS}{dx} \frac{1}{2} \rho V^2 \sin 2\beta + k' V \frac{\rho}{r} S \cos\beta + k' V^2 x \frac{\rho}{r} \frac{dS}{dx} \cos\beta \right] \tag{7}$$

where k' is the ratio of the apparent moment of inertia of the body to the moment of inertia of the displaced fluid. The first term of this equation agrees with the moment of a ship moving rectilinearly with angle of attack β. The second term describes the negative component of centrifugal force acting the length of the body, whilst the last term describes the positive components acting at each end.

A preliminary first-order solution of this equation for our bodies of revolution shows that the centrifugal forces are an order of magnitude less than the forces associated with the pitching moment created by the body moving rectilinearly at an angle of attack β.

Munk concluded that the transverse forces acting on a body of revolution in a turn are (a) due to the angular velocity associated with the tangential velocity; (b) due to the body positioned with an angle of attack

R	β	Drag (N)	C_D	Moment (N m)	C_M
3	8.71°	2.58	0.072	19.76	0.30
5	2.9°	0.52	0.024	6.67	0.10

Table 3: Forces and Moments according to Munk's calculations

(c) due to the centrifugal force of the longitudinal apparent mass and (d) due to the centrifugal force of the transverse apparent mass if the body has an angle of attack. The forces due to (a) and (b) are most important.

When we perform tests with our curved bodies, we are maintaining the effects of (a) and (b), so we are including the important forces which act on our body. What is required is an estimate of the centrifugal forces to ensure that either these forces can be safely neglected, or that a correction can be applied to our results if necessary.

5.2 Effect of the velocity gradient

In section 4 the effect of introducing a velocity gradient across our curved model was shown to incease the accuracy of the method of curved bodies. Previous calculations have shown that the magnitude of the forces and moments depends greatly on the range of z' that the velocity gradient is applied to. In order to match the change in velocity of the curved flow over the straight body, the velocity gradient should only be applied within the limits of the curved body along the z' axis. For our case, this corresponds to a variation in freestream velocity of less than 1%. In practise, this may be impossible to achieve within a wind tunnel.

Gurzhienko recorded undesirable effects when he introduced a velocity gradient across his wind tunnel using a variable cotton mesh. Although this mesh was able to introduce the correct gradient of velocity, it was present along the whole width of working section. This increased the measured forces and moments on his curved bodies, which agrees with our earlier calculations. Whilst he acknowledged the effect of this mesh in introducing more turbulence into the working section, he never fully quantified the reasons for the increased forces and moments he measured on his curved bodies.

6 CONCLUSION

In this study, comparisons were made using a commercial RANS CFD package between a body of revolution in a steady turn, and a deformed body in rectilinear flow. The results show a reasonable agreement between the forces and moments obtained using the deformed body, which is consistent with earlier work.

The use of the curved bodies provides good qualitative data in such areas as the size and location of the off-body vortex, and the location and topology of the surface streamlines and flow separation.

Simple momentum analysis shows that the absence of any centrifugal forces in the case of the deformed body has little effect on the measured forces. But the absence of these forces may affect the separation behaviour.

REFERENCES

[1] Chang MS and Purtell LP. "Three-dimensional flow separation and the effect of appendages". In "16th Symposium on Naval Hydrodynamics", 1986 .

[2] Gurzhienko GA. "Metod iskrivlenykh modelei primenenie ego k izucheniu krivolineinogo noleta vozdushnykh korablie (The method of deformed bodies and its use in the study of curved flights of airships". Technical report, Trudy TsAGI, Moscow, 1934. Translated and reprinted in 1937 as NACA reports 829 and 830.

[3] Hoang NT, Wetzel TG and Simpson RL. "Surface pressure measurements over a 6:1 prolate spheroid undergoing time-dependent maneuvers". *AIAA*, June 1994.

[4] Hosder S and Simpson RL. "Unsteady turbulent skin-friction and separation location measurements on a maneuvering undersea vehicle". In "39th AIAA Aerospace Sciences Meeting and Exhibit, Reno, Nevada", 2001 .

[5] Lloyd ARJM and Campbell IMC. "Experiments to investigate the vortices shed from a submarine-like body of revolution". In "59th meeting of the AGARD Fluid Dynamics Symposium", Monterey, California, October 1986 .

[6] Munk MM. "The aerodynamic forces on airship hulls". Technical Report 184, National Advisory Committe for Aeronautics, 1924.

[7] Wetzel TG and Simpson RL. "Unsteady crossflow separation location measurements on a maneuvering 6:1 prolate spheroid". *AIAA*, November 1998. **36**(11), 2063–2071.

Proceedings of Tenth Asian Congress of Fluid Mechanics
17-21 May 2004, Peradeniya, Sri Lanka

A NEW SURFACE TENSION FORCE MODEL FOR VOLUME TRACKING METHODS

E. Shirani
Department of Mechanical Engineering, Isfahan University of Technology
Isfahan, Iran

N. Ashgriz, and J. Mostaghimi
Department of Mechanical & Industrial Engineering, University of Toronto
Toronto, Ontario, Canada, M5S 3G8

ABSTRACT: A new method for the calculation of surface tension force in the computational modeling of interfacial flows which use volume tracking methods is developed. This method which is referred to as Pressure Calculation based on the Interface Location (PCIL), is an improved version of the CSF model and is based on the calculation of the pressure force at the interface cell faces. The pressure forces at the interface cell faces are calculated according to the pressure imposed by each fluid on the portion of the cell face that is occupied by that fluid. Special formulations for the pressure in the interfacial cells are derived for different orientations of an interface. The method is applied to a two-dimensional motionless drop of liquid in an initially stagnant fluid with no gravity force. A two-fluid, PLIC-VOF method is used to simulate the flow numerically. A wide range of Ohnesorge numbers, and density and viscosity ratios of two fluids are tested. It is shown that the presence of spurious currents is mainly due to the inaccurate calculation of pressure forces on the interface cells. The new model reduces the spurious currents up to three orders of magnitude for the cases tested.

Keywords: Volume-Of-Fluid (VOF) method; Two-phase flow; Continuum surface force; Pressure Calculation based on Interface Location (PCIL) model; Interfacial flows; Free surface flows; Spurious currents; Parasitic currents.

1. INTRODUCTION

In simulation of interfacial flows with fixed mesh, determination of the interface pressure and surface tension has been one of the most troublesome and challenging issues. Surface tension forces appear in equations by imposing a jump condition across the interface. This condition is difficult to apply numerically and has been the center of attention by many researchers.

In order to circumvent these problems, Brackbill *et al.*[1] developed a method referred to as the Continuum Surface Force (CSF) model. This model replaces the need to know the exact location of free surface by converting the surface tension effect into an equivalent volume force which is simply added to the Navier-Stokes equations as an additional body force. This force has smoothed properties and acts only in a finite transition region (where the cells or their neighbors consist of both phases) across the interface. The CSF model reformulates surface tension into an equivalent volume force F_v^{st} as follows:

$$F_v^{\;st} = s\,k\mathbf{n}\frac{\left| \; F\right|}{\left[F\right]}\frac{r(x)}{[\,r\,]}, \tag{1}$$

where, is the surface tension coefficient, is the surface curvature, **n** is the unit normal to the surface, *F* is volume fraction of heavy fluid in the cells, *?(x)* is the local value of density and [?] is the difference between the density of the heavier and the lighter fluids. The second fraction (the density correction term) in Eq. (1) is added to correct the force in the momentum equation. This dampens the acceleration of the lighter fluid in the cells near the interface that contain small amounts of heavier fluid. This fraction is not directly obtained from any conservation law, but it is only postulated.

The CSF model does not produce accurate numerical solution in capillary dominated fluid problems. In problems where the surface tension forces dominate the viscous forces, the spurious currents can cause interface oscillations and deform or destroy the interface. New methods are needed to deal with this problem. There have been some attempts to reduce the spurious currents. Popinet and Zaleski[8] have reduced the spurious currents considerably using a front capturing algorithm for the solution of two-dimensional flows. They have used a Lagrangian advection marker to advect the interface and have calculated the pressure force according to the location of the interface at each cell face. Meier *et al*.[6] have also developed a new method based on the higher order model for the calculation of interface curvature to reduce the spurious currents. Renardy and Renardy[9] have introduced another VOF based algorithm (referred to as PROST) for the calculation of the body force due to the surface tension. The advection of the volume fraction in their method is based on a Lagrangian scheme that allows no diffusion and produces a sharp interface. They have used a least-square fit of a quadratic surface to the volume fraction function for each interface and its neighbors. Jamet *et al*.[4] have introduced a model to eliminate the parasitic currents through the conservation of energy in the second gradient method. Therefore, by using the second-gradient method and the reduction of the truncation error in the computation of the energy exchanges between the surface and the kinetic energies, the energy is conserved and the parasitic currents are reduced drastically.

Although the above methods reduce the spurious currents by some orders of magnitude, the methods are expensive, somewhat complicated and they may not accurately calculate the pressure force at the interface. Here, we present a new method, which we will refer to as the Pressure Calculation based on the Interface Location (PCIL). We will show that by an accurate implementation of the pressure forces at the interface cells, it is possible to eliminate a significant portion of the spurious currents. By using this new method, the spurious currents can be reduced by up to three orders of magnitude. Unlike the above mentioned methods, PCIL model is simple and extremely inexpensive (very limited extra calculations are needed to implement PCIL model). The new method is directly derived by applying the momentum balance on each interface cell.

2. GOVERNING EQUATIONS

For the unsteady, incompressible Navier-Stokes equations in two dimensions and with fluid interfaces the volume-of-fluid, VOF[3], method along with a piecewise linear interface calculation, PLIC[7], is used to capture the fluid interfaces. The governing equations describing this problem are:

$$\frac{u_i}{x_i} = 0, \tag{2}$$

$$\frac{F}{t} + u_i \frac{F}{x_i} = 0, \tag{3}$$

and

$$\frac{r u_i}{t} + \frac{r u_i u_j}{x_j} = \quad \frac{p}{x_i} + F_v^{st}.\hat{i} + m\frac{{}^2 u_i}{x_j{}^2} + r g_i, \tag{4}$$

where, u_i's are the velocity components, and t and x_i are time and space coordinates, the volume fraction of fluid, F, is zero where only fluid 2 exists in the cell and is one where only fluid 1 exits in the cell, p is pressure, $\hat{i}$ is unit vector in i^{th} direction and *?* and *μ* are the mixture density and absolute viscosity and they depend on the densities and viscosities of each fluid as:

$$r = r_2 + F(r_1 \quad r_2), \tag{5}$$

and

$$m = m_2 + F(m_1 \quad m_2), \tag{6}$$

where, $?_1$ and $?_2$, μ_1 and μ_2 are densities and viscosities of fluids 1 and 2, respectively.

3. SURFACE TENSION FORCE MODEL

Consider a two-dimensional interface cell shown in Fig. (1), in which fluid 1 and 2 are separated by an interface line. We denote fluid 1 as the heavier fluid and fluid 2 as the lighter fluid. If the surface tension forces are considered, then there would be a pressure jump at the interface. Thus, the value of the pressure in each fluid may be different. In order to calculate the pressure force exerted on the cells. We apply the momentum balance equation to the cell.

From the balance of the pressure force acting along the *x*-direction on the cell the pressure force per unit area on the left side of the cell, which is the average pressure acting on this side of the cell, can be obtained as follow:

$$p_L = p_{2L} + H_L(p_{1L} \quad p_{2L}), \tag{7}$$

where, p_L is the average pressure on the left side, and $H_L \quad \frac{l_L}{y}$ is a non-dimensional parameter that denotes the location of the interface at the left side of the cell, *?y* is the length of the cell in *y* direction and l_L is the length of the cell side which is in contact with fluid 1.

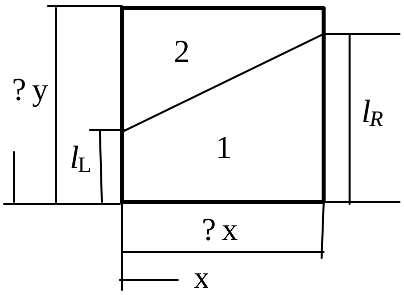

Fig. 1 An interface cell described based on the volume of the fluids.

The pressure difference in the parenthesis represents the pressure jump due to surface tension. Similar relations can be obtained for the pressure force on the right *(R)*, top *(T)* and bottom *(B)* sides of the cell:

$$p_k = p_{2k} + H_k(p_{1k} \quad p_{2k}), \tag{8}$$

where, *k* may be *L, R, T,* or *B*. H_k is the non-dimensional parameter corresponding to the *k* side of the cell. The value of H_k is between zero and one in the interface region and is one or zero otherwise, depending on being in fluid 1 or 2, respectively.

The pressure jump, p_s, at the interface is related to the surface tension coefficient according to:

$$p_s = p_1 \quad p_2 = s\,k\ . \tag{9}$$

Therefore, Eq. (8) becomes:

$$p_k = p_{2k} + H_k s\,k\ , \tag{10}$$

The second term in the right hand side of Eq. (10) is the normal force per unit area due to the pressure jump or surface tension force,

$$\mathbf{F}_s^{\ st} = Hs\,k\mathbf{n}\,. \tag{11}$$

So our model for the surface tension force would be the modified version of CFS model which the factor H is included in the model. Thus Eq. (1) becomes:

$$F_v^{\ st} = Hs\,k\mathbf{n}\frac{|\ \ F|}{[F]}\,. \tag{12}$$

Note that the density correction factor (the last term in the Eq. 1) is no longer needed and is omitted in our model. In the process of the reconstruction of interface, the location of the interface and its cross-section with the cell faces is already determined (see Youngs[12] and also Shirani *et al.*[11] for more details). So the value of H_k on each side of a cell can be easily calculated.

Finally the PCIL method explained above may be summarized by the following steps:

1. Determination of the intersection locations of an interface line with the cell faces.

2. Calculations of H_k, by normalizing the intersection locations with the cell face length.
3. Multiplying the value of H_k to the capillary forces used in the momentum equation, Eq. (12).

4. RESULTS AND DISCUSSIONS

The CSF model for surface tension force is modified using our PCIL model and is tested by simulating the temporal evolution of a two-dimensional liquid drop. A circular drop of the liquid in the absence of gravity is placed inside of a second fluid. The initial velocities of both fluids are set to zero. The drop radius, r, the fluid densities, $?_1$ and $?_2$, the viscosities, μ_1 and μ_2, and the surface tension coefficient, s, are the main physical variables (subscript 1 stands for the drop and 2 for the surrounding fluid). The number of grid points, the time step, $?t$, and the grid size, h, are the numerical parameters. The computational grid is fixed, rectangular and uniform. The code SURFER[5] is modified and used in this work. The details of the numerical method based on VOF-PLIC and Chorin's projection method for a semi-implicit Navier-Stokes solver, which have been used in this code, are given in[5] and are not repeated here.

Number of grid points, the grid size, the time step, and the radius of the drop are held fixed. We investigate the effects of variation of physical properties (i.e., density, viscosity and surface tension coefficient) on the flow field. Due to the inaccurate modeling and calculation of the pressure force at the interfacial cells, the spurious currents are produced. These currents tend to grow with time. The drop radius is taken as 0.25L, where L is the domain length in the x-direction and it is set equal to one. A 66×66 mesh and a time step of 10^{-5} are chosen for all of the calculations.

From the dimensional analysis the physical properties of the problem are grouped into three non-dimensional parameters:

$$Oh_1 = \frac{m_1}{\sqrt{r r_1 s}}, \quad \frac{r_1}{r_2} \quad and \quad \frac{m_1}{m_2}, \tag{13}$$

where Oh_1 is Ohnesorge number based on the properties of fluid 1 contained in the drop. Following Popinet and Zaleski [8] and Scardovelli and Zaleski[10], for a constant radius drop and from the dimensional analysis, the velocity of spurious currents is only a linear function of the surface tension coefficient and viscosity, i.e., $u \sim s/\mu$, and it is not a function of density. Thus it is expected that as the density of the flow changes, the velocity of the spurious currents remains constant.

A wide range of values including the properties of water (fluid 1) and air (fluid 2) are used for the above parameters. The results are presented in terms of the norms of the velocity (mean values of the absolute velocity) and the maximum values of the velocity of the spurious currents as a function of various variables. Figures (2) and (3) show the velocities of spurious currents at N=8000, when the density correction factor, (see Eq. 1), is or is not used, respectively. N is the number of time steps. The scale for the velocity vectors shown in the figures is the same. The results in this case are obtained for a drop of water in air, i.e., $?_1/?_2 = 830.545$, $\mu_1/\mu_2 = 54.945$ and the Ohnesorge number based on the water properties (Oh_1) is 1.17×10^{-4}. As can be seen form the figures, the addition of the PCIL model results in much smaller spurious currents.

Figure (4) shows the maximum velocities of the spurious currents as a function of time for the above cases. The results show that the velocities of spurious currents are reduced by orders of magnitudes when the PCIL model is used. From Figure (3) it can be seen that once the density correction ratio is added, the spurious currents become smaller, but they are still significant. By implementing the PCIL model, the velocities of the spurious currents drop by about two orders of magnitudes. Note that in all the cases studied, the spurious currents still tend to increase with time. From the figure, it can clearly be seen that the implementation of the PCIL factor is enough to reduce the spurious currents and there is no need to implement the density ratio correction in addition to the PCIL. Therefore, the PCIL model is a better alternative to the density ratio correction, which is some what a heuristic relation and does not reduce the spurious currents as much as the PCIL model.

Effects of fluid properties in the form of density and viscosity ratios and Ohnesorge number are considered here. Figure (5) shows the maximum velocities of spurious currents as a function of density ratio. Results for cases with and without the PCIL model are presented. The viscosity ratio (μ_1/μ_2) is 54.945 and $Oh_1 = 1.17\times10^{-4}$ (equivalent to that of a drop of water in air). This figure shows that as the density ratio increases, the velocity of the spurious currents remains constant for the corrected pressure forces, while it increases when the correction is not applied. This variation of velocity in the corrected version is in agreement with the dimensional analysis, which indicates that $u \sim s/\mu$ and it should not be a function of density. It has been recorded by other researchers (e.g. see[2]) that by increasing the density ratio, the spurious current velocity increases and thus they cannot get reasonable results for high density ratios. Figure (5) shows that when the PCIL model is used, the increase in the density ratio does not generate extra spurious velocities. Therefore, one may be able to get reasonable results for high density ratios.

Figure (6) shows the maximum velocities of the spurious currents as a function of Ohnesorge number. Results for both cases with and without the PCIL model are presented. In this figure, the density ratio ($?_1/?_2$) is 830.545 and the viscosity ratio (μ_1/μ_2) is 54.945. It is shown that the spurious velocities decrease by two orders of magnitude when the PCIL is used. As Oh_1 increases, the spurious velocities decrease by a power law. The variation of the velocity with Oh_1 is also in agreement with the dimensional analysis which indicates $u \sim s/\mu$.

Figure (7) shows the maximum velocities of the spurious currents as a function of viscosity ratio. Results for both cases with and without the PCIL model are presented. In this figure, the density ratio ($?_1/?_2$) is 830.545 and $Oh_1 = 1.17\times10^{-4}$. Here, μ_1 has been changed and in order to keep Oh_1 constant, the surface tension coefficient is changed accordingly. It is shown that the spurious velocities decrease by more than two orders of magnitude when the correction is applied. As the viscosity ratio increases, the spurious velocities increase by a power law. This variation is also in agreement with the dimensional analysis which indicates that $u \sim s/\mu$,[8,10].

5. CONCLUSIONS

A new method for the calculation of the pressure force at the interface cells for volume tracking methods is derived and presented. In this method, first the intersection locations of an interface with the interfacial cell faces are determined. Then the area of a cell face which is in contact with the heavier fluid is normalized with the cell face area to obtain a factor *H*. Finally, the capillary force used in momentum equation is corrected by multiplying it by the factor *H* determined for the cell.

The new method is applied to a sample problem of still drop in a motionless fluid. It is shown that the velocities of the spurious currents decrease by more than two orders of magnitude. Variation of the velocity of the spurious currents with Ohnesorge number, density and viscosity ratios of the two fluids involved, are examined. It is found that the variation with the Ohnesorge number and the viscosity ratio is a power law. Changes in the density ratio do not affect the corrected version. However, the spurious currents drastically increase with the density ratio when pressure is not corrected. Although the spurious currents are reduced by several orders of magnitude when the corrected pressure is used, there are still some currents in the flow. They increase with time at a rate similar to those in the original CSF model but with much smaller magnitudes. These currents can be further reduced by using a more accurate calculation of normal vectors and the interface locations.

REFERENCES

1. Brackbill, J.U, Kothe, D.B., and Zemach, C.: A continuum Method for modeling surface tension. *J. Comput. Phys.* **100**:335-354, 1992.
2. Gueyffier, D., Li, J., Nadim, A., Scardovelli, R., and Zaleski, S.: Volume-of-Fluid Interface Tracking with Smoothed Surface Stress Methods for Three-Dimensional Flows. *J. Comput. Phys.* **152**:423-456, 1999.
3. Hirt, C.W., and Nichols, B.D.: volume of Fluid (VOF) method for the Dynamics of Free Boundaries. *J. Comput. Phys.* **39**:201-225, 1981.
4. Jamet, D., Torres, D. and Brackbill, J.U.: On the Theory and Computation of Surface Tension: The elimination of Parasitic Currents through Energy Conservation in the Second-Gradient Method. *J. Comput. Phys.* **182**:262-276 (2002).
5. Lafaurie, B., Nardone, C., Scardovelli, R., Zaleski, S., and Zanetti, G.: Modelling merging and fragmentation in multiphase flows with SURFER. *J. Comput. Phys.* **113:**134-147, 1994.
6. Meier, M., Yadigaroglu, *H*., and Smith, B.L.: A novel technique for including surface tension in PLIC-VOF methods. *Eur. J. Mech. B/Fluids* **21**:61–73, 2002.
7. Polliod, J.E.: An Analysis of Piecewise Linear Interface Reconstruction Algorithm for Volume of Fluid Methods. *M.Sc. Thesis*, Department of Mathematics, University of California, Davis, 1992.
8. Popinet, S., and Zaleski, S.: A front-tracking algorithm for accurate representation of surface tension. *Int. J. Numer. Meth. Fluids* **30**:775–793, 1999.
9. Renardy, Y., and Renardy, M.: PROST: A Parabolic Reconstruction of Surface Tension for the Volume-of-Fluid Method. *J. Comput. Phys.* **183**:400-421, 2002.

10. Scardovelli, R., and Zaleski, S.: Direct numerical simulation of free surface and interfacial flow. *Annu. Rev. Fluid Mech.* **31**:567-603, 1999.
11. Shirani, E., N. Ashgriz, and J Mostaghimi: Interface Pressure Calculation Based on Conservation of Momentum for Front Tracking Methods. *Submitted for Pub., JCP*, 2003
12. Youngs, D.L.: Time-Dependent Multi-material Flow with Large Fluid Distribution. in **Numerical Methods for Fluid Dynamics**, Morton and Norman, Editors, 187-221, 1986.

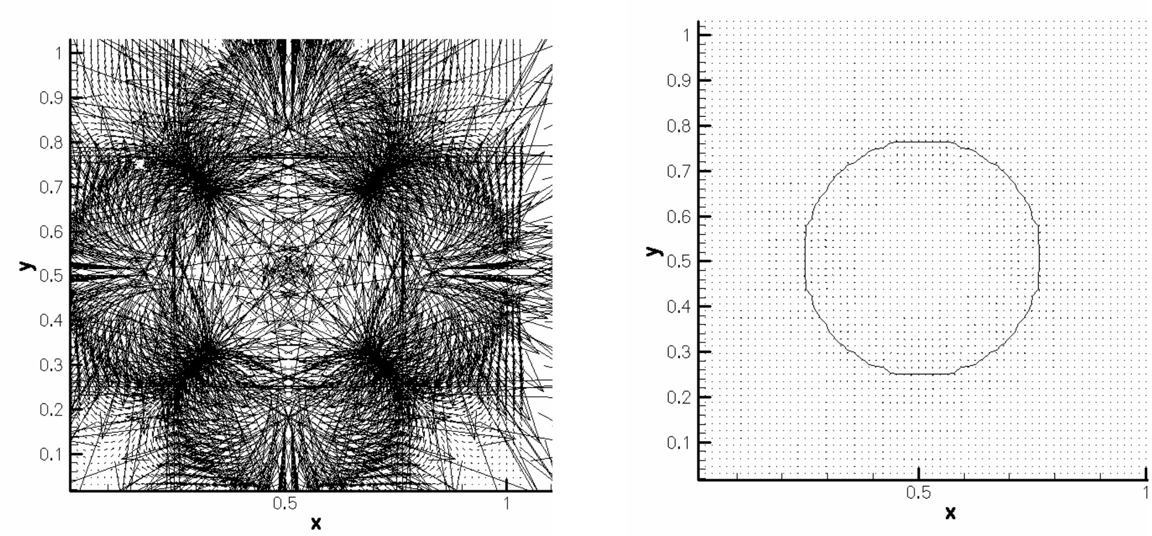

Fig. 2 Spurious currents with the same velocity scales, without density correction without PCIL model (left column) and with PCIL model (right column)

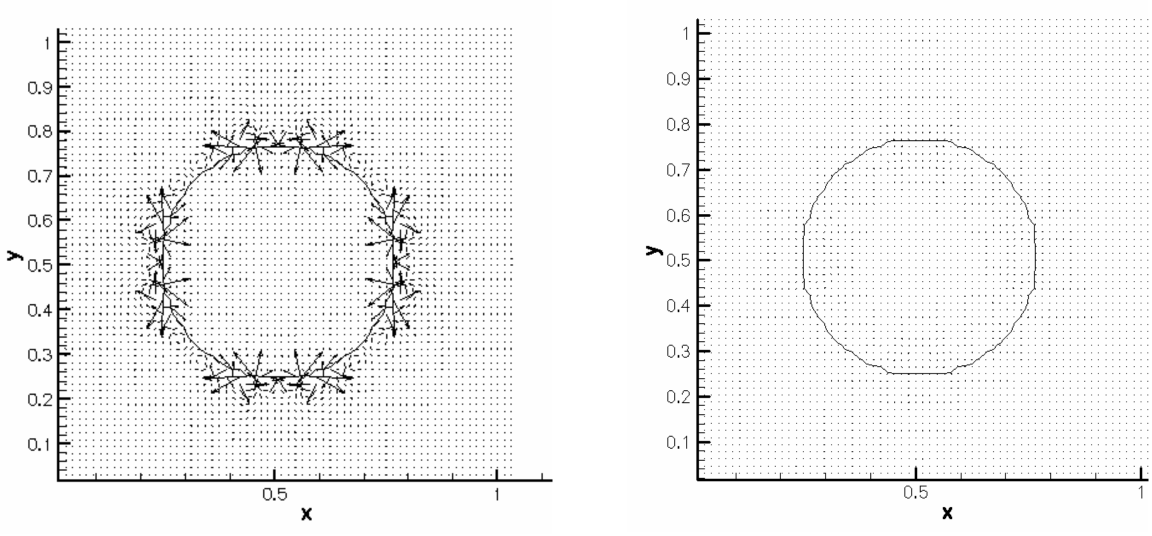

Fig. 3 Spurious currents with the same velocity scales, with density correction without PCIL model (left column) and with PCIL model (right column)

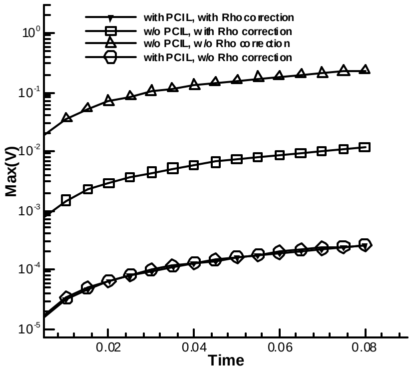

Fig. 4 Max. spurious velocity as a function of time

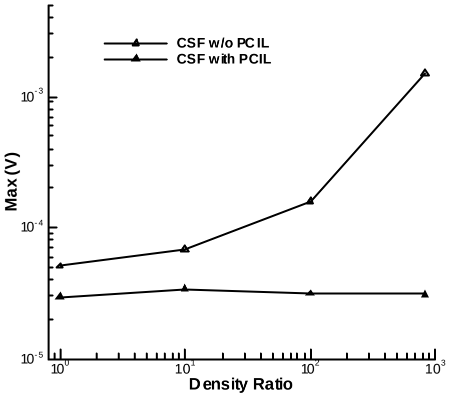

Fig. 5 Max. spurious velocity as a function of density ratio

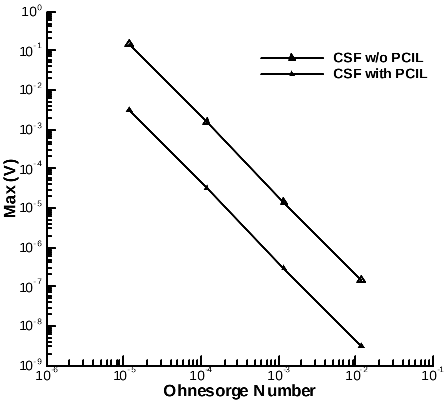

Fig. 6 Maximum spurious velocity as a function of Ohnesorge number

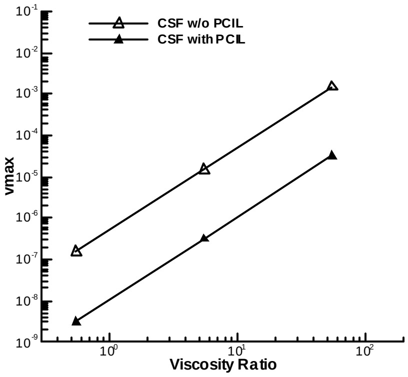

Fig. 7 Maximum spurious velocity as a function of viscosity ratio

Proceedings of the Tenth Asian Congress of Fluid Mechanics
17-21 May 2004, Peradeniya, Sri Lanka

IN-VITRO STUDY ON THE STEADY FLOW CHARACTERISTICS OF PROXIMAL ANASTOMOTIC MODELS

L. P. Chua, W. F. Ji and T. M. Zhou
School of Mechanical and Production Engineering, Nanyang Technological University, Singapore 639798

ABSTRACT: Particle Image Velocimetry (PIV) was used to study the effects of grafting angle, graft Reynolds number and graft resistance on the steady flow characteristics of proximal anastomosis. Low velocity regions are found at the heel and toe, whose size depends on the Reynolds number, anastomosis angle and resistance of the graft. Stagnation point is found along the graft outer wall. The spatial gradients of wall shear stress are high around the anastomosis joint. Based on the experimental results, the method of improving the graft patency rate is proposed.

1. INTRODUCTION

Arterial bypass graft, the major treatment for arterial stenosis, has long-term patency problem due to the formation of intimal hyperplasia along the graft and at the graft/artery junction. It has been well demonstrated that the hemodynamic factors, including anastomosis angle, flow rate ratio of the graft to the aorta, wall shear stress distribution etc, are linked to the development of intimal hyperplasia [1, 2]. However, most of the previous studies were focused on the distal anastomosis and little effort has been put on the proximal side. But it is possible that the proximal anastomosis provides the condition to form mitogens and activated platelets, and then they are convected down to the distal part. The effect of flow patterns of the proximal side on the distal part has not been fully understood. Therefore the objective of this study is to investigate the effect of flow angle, flow rate, and wall shear stress distributions etc. on the graft patency under steady flow condition by PIV measurement.

2. EXPERRIMENTAL METHODS

2.1 Flow Models and Working Fluid

Proximal anastomosis models with angles of 30, 45, 75and 90 degree were fabricated from pyrex glass for backward facing graft condition, as shown in Fig. 1. The "aorta" and the "graft" have the inner diameters of 20mm and 6mm respectively. The working fluid involved mixing 30% of glycerin with 70% of aqueous ammonium thiocyanate (NH_4SCN) solution by weight. The aqueous ammonium thiocyanate solution was made up of equal parts of ammonium thiocyanate salt and distilled water by weight. The solution has a refractive index of 1.47 and dynamic viscosity of $4.08\times10^{-3}\,Pa\cdot s$ at the room temperature $22^{\circ}C$, which were measured by commercial refractometer (model ATAGO 3T) and a controlled rate rheometer (model Contraves low shear 40) respectively. Polyamid Seeding Particle (38A2-121 PSP-50, Dantec Measurement Technology) was added into the fluid to highlight the flow field.

2.2 Flow Circuit and PIV System

Fig. 2 is a schematic presentation of the experimental setup for Particle Image Velocimetry measurements. The fluid is forced from a sump tank (1) by a centrifugal pump (2) into the reservoir and overflow container (3). To maintain a constant static pressure in the model, overflow fluid flows back into the sump tank (1). The fluid flows through the contraction cone (6) and then the test model (8) before going back into the sump tank (1). The three valves (4), (4a) and (4b) are used to control the inlet flow rate and resistance of the aorta and the graft respectively. The flow meter (5) monitors the flow rate into the graft.

A Q-switched, double cavity pulsed Nd: YAG laser was used as the illumination source, which has a repetition rate of 10Hz and provides two thin (0.3-1mm) green laser sheets ($\lambda = 532nm$). An 80C42 DoubleImage 700 camera with a Nikon AF Micro-Nikkor lens 60/2.8 was used to capture two consecutive images of the scatter particles passing through the test section.

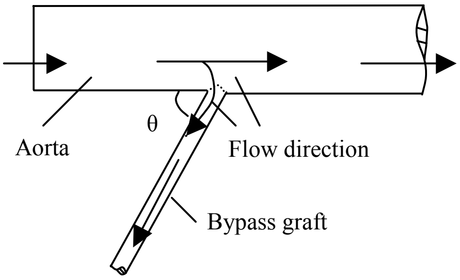

Fig. 1 Schematic designs of the proximal anastomotic models

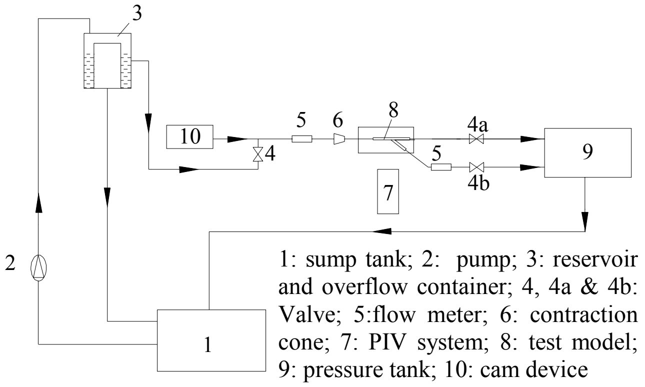

Fig. 2. Schematic presentation of in-vitro experimental arrangement.

Clinical studies have shown that the mean flow rate in the saphenous vein aorta-to-coronary graft is around $79 \pm 25ml/\min$ [3] and the Reynolds number based on the 6 mm diameter graft and $79ml/\min$ is around 169. Hence Reynolds numbers 100, 169 and 250 were selected as the control parameter in this measurement to study the flow characteristics under different peripheral resistance (after aorta) conditions.

3. RESULTS AND DISCUSSION

The flow characteristics of 45° backward facing graft model with Reynolds number at the graft Re_G =100 and 250 were shown in Fig. 3 (a) and (b) respectively. For Re_G =100, the aorta flow follows closely to the contour of the wall before it starts to deviate towards the graft upon passing the heel section (at about half the graft diameter). The flow reattaches at the graft inner wall at further downstream location, which results in the formation of a low velocity region closed to the heel. Close to the toe section, the deviated main flow approaches the high curvature wall and forms a stagnation point where the flow bifurcates. The velocity distribution in the graft is skewed towards the graft outer wall at the entry, and at further downstream of the graft, the flow is observed to skew slightly towards to the inner wall.

For Re_G =250, it is observed that the main flow moves towards the graft much earlier as compared to Re_G =100 case. This has resulted in the formation of the low velocity region near the heel to move further downstream and smaller in size. Meanwhile the fluid in the graft is observed to impinge on the outer wall which results in the stagnation point near the toe. It has also been observed that the size of the low velocity region along graft inner wall is smaller than those of Re_G =100 and Re_G =169 (not shown here).

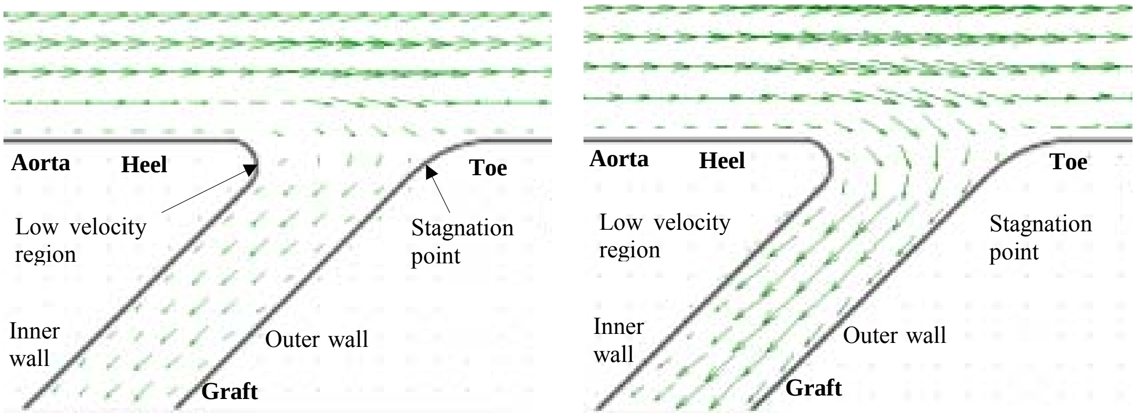

(a) (b)

Fig. 3. Flow characteristics of 45° backward facing graft model under different Re_G (a) $\mathrm{Re}_G = 100$; (b) $\mathrm{Re}_G = 250$.

The effect of anastomotic angle on the flow characteristics has also been studied in this project. The flow fields of 30°, 45°, 75° backward facing and 90° graft models at $\mathrm{Re}_G = 169$ are shown in Fig. 4 (a), (b), (c) and (d) respectively. Comparing velocity plots of different backward facing graft models, it is observed that the 45° backward facing model has the smallest low velocity region near the heel along the graft inner wall. It is also noticed that in this model the flow upon entering the graft tends to follow more closely to the geometry of the graft at further downstream. However, in cases of 30°, 75° backward facing graft model the flow skews more obviously toward the graft outer wall and results in a new low velocity region along the graft inner wall. On the whole, it is noted that the flow skews toward outer wall greatly in the graft at other angles except 45° backward facing graft model. In summary, the low velocity regions are observed to locate at the heel and toe at all anastomotic models. The region at the heel is thus experienced low shear stress [4], which is an ideal site for thrombus formation. These low velocity regions will also be prone to fat deposition and result in the formation of hyperplasia at the joint, blocking the re-routed blood flow into the graft.

The investigation on the effect of the resistance at the end of the graft was conducted in this experiment. With the preset inlet flow rate ($5l/\mathrm{min}$), The graft resistance is simulated by 1.00, 1.25, 1.50 and 1.75 rounds of valve (4b) opening, which is corresponding to the flow rate ratio Q_G/Q_A of 0.0293, 0.0380, 0.0447 and 0.0507 respectively. Note the Fig. 5 (a) to (d) show the enlarged velocity plots of 45° backward facing model under different resistance conditions. It is observed that the low velocity region at the heel reduces in size with the increase of valve opening, which is increase of graft flow rate. It is also noticed that at larger graft flow rate, the flow in the aorta skews less towards the graft outer wall before entering the graft, and the flow aligns back to the graft axis at relative shorter downstream distance.

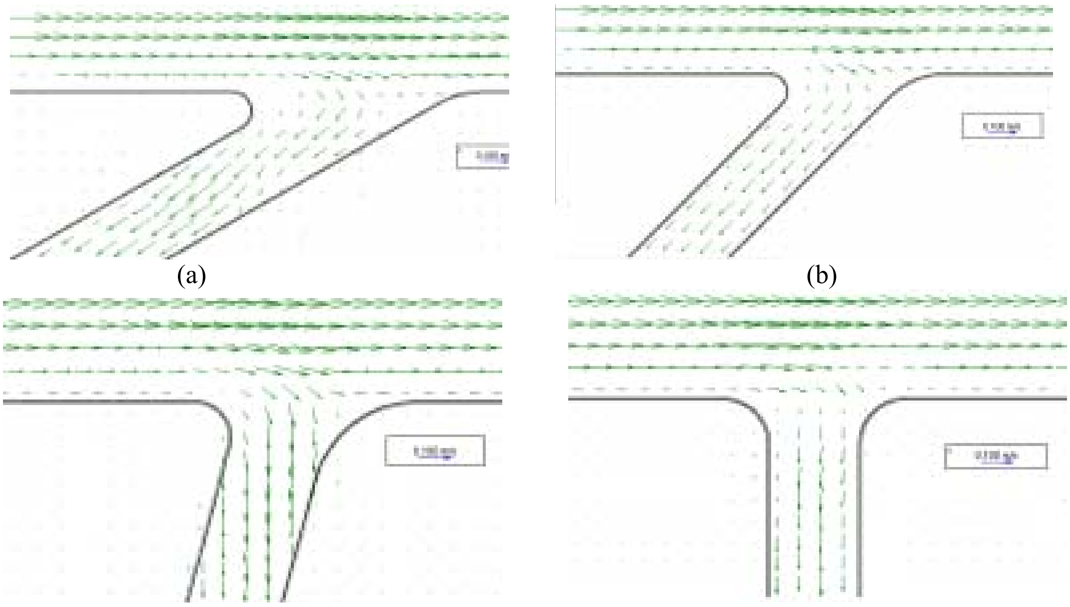

(a) (b)

(c) (d)

Fig. 4. Flow fields of various anastomotic angles in models with Re_G =169. (a) 30° backward facing (b) 45° backward facing (c) 75° backward facing (d) 90° graft model.

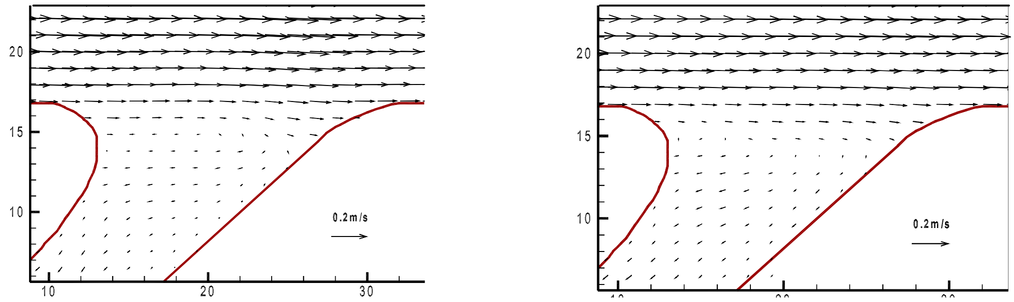

(a) Valve opening at 1 rnd (b) Valve opening at 1.25 rnd

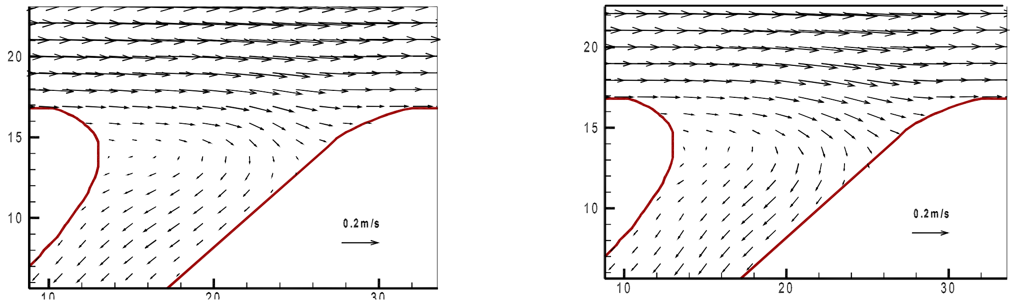

(c) Valve opening at 1.5 rnd (d) Valve opening at 1.75 rnd

Fig. 5. Velocity vector and streamline of 45° backward facing graft model with different resistance configurations: (a) 1 rnd, (b) 1.25 rnd, (c) 1.5 rnd and (d) 1.75 rnd of valve opening

The wall shear stresses along the graft inner wall and outer wall were calculated using the following relation:

$$\tau = \mu \frac{\partial u}{\partial y} |_{y \to 0} \tag{1}$$

where $\partial u / \partial y$ is the velocity gradient close to the wall and $\mu = 4.08 \times 10^{-3}\, Pa \cdot s$ is used in the present study. Fig. 6 shows the wall shear stress distribution in 45° backward facing model with different Re_G. Note the coordinates used to express the wall shear stress profiles are shown schematically at the corner of the figures. The annotation, x_1 and x_2 are the points selected approximately at the end of the straight aortic wall and are going along the direction of the graft inner and outer walls respectively.

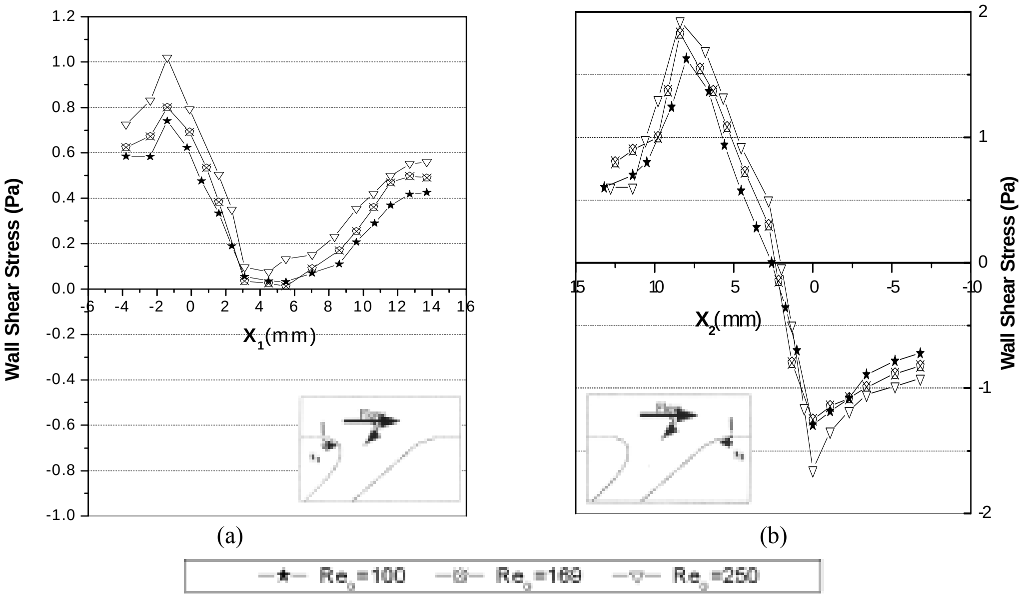

(a) (b)

Fig. 6 Wall shear stress distributions in the 45° backward facing anastomotic joint with different Re_G. (a) Inner wall;(b) Outer wall.

The wall shear stress value falls sharply to a low level at the curved section of the inner wall around $x_1 = 3mm$ as shown in Fig. 6 (a), and then remains fairly constant over a distance before gradually increasing at further downstream of the graft. At around the toe region as shown in Fig. 6 (b), the wall shear stress along the graft increases after moving away from the stagnation point (whereby wall shear stress=0 at $x_2 = 3mm$) but remains fairly constant at the region beyond $x_2 = 10mm$. This is probably due to the fact that the fluid beyond this point has actually realigned itself with the graft axis. A peak value of wall shear stress is found at the region about $x_2 = 8mm$ which corresponds to the sudden change in the flow direction at the region upon hitting the graft outer wall. For the region whereby part of the bifurcation flow goes back to the aorta, the wall shear stress decreases sharply till the minimum of -1.7 Pa at $x_2 = 0.0mm$ for Re_G =250, before it gradually levels at approximately -0.75 Pa at $x_2 = -4.5mm$, i.e. it is at the similar level of those at the aortic wall before the joint. Note that the negative value in the aorta is due to the definition of x_2.

In general, the distribution of wall shear stress is consistent with the general flow characteristics described in the earlier section. The region downstream of the stagnation point along the outer wall has a higher wall shear stress value than those at the upstream aorta region. When the Re_G increases from 100 to 250, the highest wall shear stresses along the outer wall increase from $-1.6\,\mathrm{Pa}$ to 2.0 Pa. This should be due to the high flow rate in the graft, resulting in the higher lashing stress on the toe of the graft. Note that large wall shear stress variation is found near the heel and toe region. It is believed that the high wall shear stress variation together with the low wall shear stress region was associated with the formation of intimal hyperplasia [4, 5, 6].

4. CONCLUSION

The velocity vectors obtained from the PIV measurements provide a comprehensive view of the flow fields in the anastomotic models. In the steady flow, low velocity regions were observed at the heel and the toe of the anastomotic model. In addition, stagnation points were also found along the outer wall in all cases. The low velocity region at the heel is an ideal site for thrombus formation. The spatial extent of these low velocity regions was dependent on the flow rate in the graft as well as the anastomotic angle, that is the higher the flow rate in the graft, the smaller the size of the low velocity region near the heel.

Large wall shear stress variation was found near the heel and the toe of all anastomosis models. Note that the peak wall shear stress is always found at the graft outer wall and a small region near the heel has a relatively low wall shear stress level (range from 0 to 0.5 Pa). The experimental results under steady flow condition could provide detailed and reliable flow fields and wall shear stress distribution of the anastomosis. More realistic physiological waveform shall be used in the next stage of study and the results will be reported in due course.

ACKONWLEDGEMENT

The financial support of A*STAR Project Number 0221010023 is gratefully acknowledged.

REFERENCE

[1] Hofer M, Rappitsch G, Perktold K, Trubel W, Schima H: Numerical study of wall mechanics and fluid dynamics in end-to-side anastomoses and correlation to intimal hyperplasia. *J Biomech*. 1996, **29**, 1297-1308

[2] Vorp, DA: Fluid mechanical considerations in vascular grafts. ASAIO J, 1997, **43**(3), 237-238.

[3] Jaffrin MY, Caro CG. *Biological flows*. New York: Plenum Press, 1995.

[4] Shu MCS, Hwang NHC: Heamodynamics of angioaccess venous anastomoses. *J Biomed. Eng*., 1991, **13**,103-112.

[5] Henry FS, Collins MW, Hughes PE and How TV: Numerical investigation of steady flow in proximal and distal end-to-side anastomoses. *J Biomechanical Eng*. 1996, **118**, 302-310.

[6] Kleinstreuer C, Lei M and Jr, JPA: Hemodynamic simulations and computer-aided designs of branching blood vessels. *J Biomechanical Eng.,* 1996, **118**, 506-510.

Proceedings of the Tenth Asian Congress of Fluid Mechanics
17-21 May 2004, Peradenia, Sri Lanka

A NEW METHOD OF FLUIDIZATION EXPERIMENT

R Takaki, K.Hatada, M. Matsuda and D.Shugai
(Department of Mechanical Systems Engineering, Tokyo University of Agriculture and Technology,
Koganei, Tokyo 184-8588, Janan)

ABSTRACT: A new experimental technique was developed to measure all particle positions which are dispersed in a liquid three-dimensionally. This measurement was shown to be possible if particles and liquid are transparent with the same index of refraction, they are illuminated by a laser sheet and a fluorescent material is mixed in the liquid. By traversing the laser sheet in the direction perpendicular to the camera axis, we could obtain series of cross sectional images of particles and after image analysis we could calculate coordinates of all particles. This method was shown to be applied to the case of fluidized particles.

1. INTRODUCTION

Behavior of particles in fluidized liquid-particle systems are difficult to observe, because they are obstructed by other particles in the container. This is the reason why particle behavior in 3D fluidized system has not been studied precisely. There are some trials to obtain particle positions by the use of laser sheet. For dilutely dispersed systems direct observation of particles are possible[1]. Transparent particles packed in a liquid with the same refraction index were observed [2]. Particles including fluorescent material were visualized under illumination by laser light [3]. In these methods particles are overlapped in densely dispersed cases, and identification of each particle is rather difficult.

Now, the present authors have shown that particle positions in 3D liquid-particle system can be measured if the conditions listed below are satisfied. This idea was proposed at an informal seminar[4].

(1) Particles and liquid are transparent and have an equal deflection indices,
(2) the liquid contains a certain amount of fluorescent material,
(3) the system is illuminated by a laser sheet, from the direction perpendicular to the axis of camera.

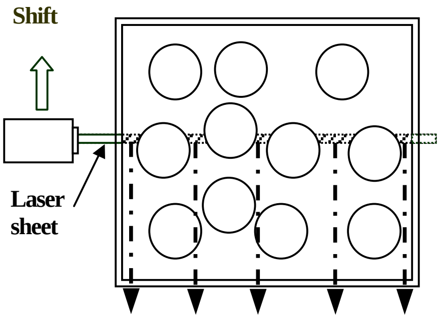

Fig.1 Basic idea of this work. Left: arrangement of particles and laser sheet. Right: an example of cross sectional image.

As is shown in Fig. 1(a), the laser sheet is not scattered or refracted while going through the liquid particle system. Moreover, when a fluorescent material is mixed in the liquid, only the liquid part within the cross section by the laser sheet emit light, which is visible from the direction perpendicular to the laser sheet. This image is not disturbed by the particles because of the same refraction indices between particles and liquid. Figure 1(b) is an example of cross sectional image of liquid-particle system taken in this way. By recording images at many cross sections one can obtain positions of all particles after some image analyses. This is the basic idea of this method. Precise of the method of measurement is explained in the next section.

2. APPARATUS

The apparatus for measuring particle positions in fluidized system is shown in Fig. 2. It was composed of a test section, 100 x100 x150 mm, in which spherical particles of acrylic resin with diameter 15 mm and a mixture of two types of silicon oil (Shinetsu-Kagaku, KF56 and KF96-50CS) with a small amount of fluorescent material (pyrromethene 580, 5.72×10^{-1} mg/lit) were filled, a laser system (Ion Laser Tech., 5490A) with an optical system to produce a light sheet, a roller pump (Furukawa Science, RP-KV1-100) to circulate the liquid, a temperature regulator and a video camera. Glass fibers for light transmission were set with interval 5 mm, which played a role to indicate the position of the laser sheet.

Data obtained directly from the video images were the *x*- and *y*-coordinates and the radii of cross section of all particles. Each particle was cut twice by the laser sheet, and from data at these two cross sections one could calculate the z-coordinate of the particle centers.

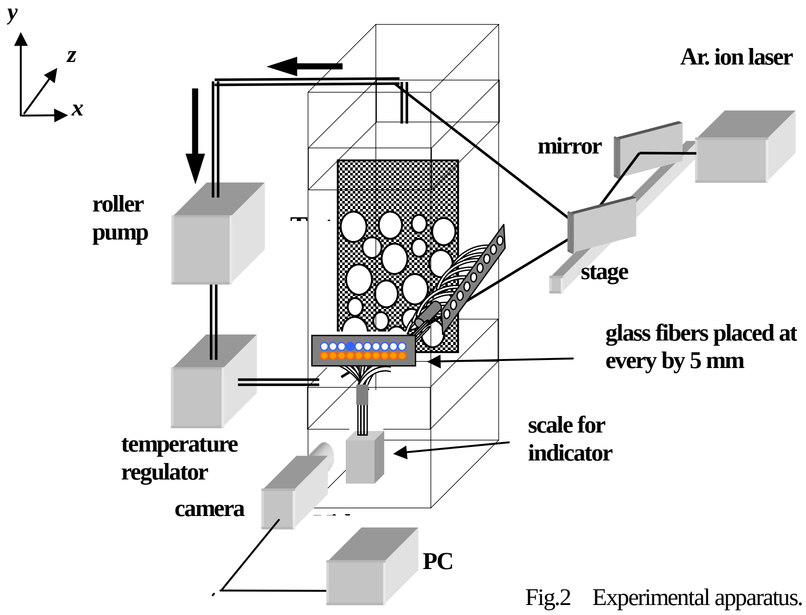

Fig.2 Experimental apparatus.

In general refraction indices depend on the temperature. In a preliminary experiment it was confirmed that the refraction indices of the particles and the liquid became equal at the temperature 32℃, where images of particles were sharpest. The temperature regulator shown in Fig. 2 was necessary to assure this temperature condition.

In order to know the position of the laser sheet in the *z*-direction, glass fibers were arranged linearly, which were directed to receive the laser sheet. Other ends of the glass fibers were arranged linearly directed to the camera, so that one glass fiber at the position of the laser sheet transmitted laser light. In addition scale for this position indicator was attached below the ends of the glass fiber.

3. RESULTS

First, accuracy of this method was examined by measuring positions of particles with known configuration. Next, this method was applied to the case of fluidized particles.

3.1 Estimation of accuracy

Accuracy of measurement was examined for rest particles arranged in close-packed state. Under the condition with the laser traversing velocity 75 mm/s, video data with 60 frame/s and exposure time 0.01s, which was the best condition for the present apparatus, the coordinates of particles relative to one particular particle could be obtained with error of 0.5 mm (about 0.5 % of the particle diameter).

Reproducibility of measurement was examined for randomly packed particles at rest by measuring twice during both ways of laser traversing. Deviations of particle positions between two measurements were 0.5 mm in *x*- and *y*-coordinates and 1-2 mm in *z*-coordinate. The worse reproducibility in *z*-coordinates came from a systematic error in deviation between the shatter instant of the video camera and the glass fiber indicator.

3.2 Measurement for fluidized particles

The particles were fluidized by operating the roller pump with flow rate 1.3 lit/min. In this case particles were moving with velocities less than about 2 mm/s. By traversing the laser sheet both ways 3 times without any pose in between, six sets of cross sectional data were recorded. The interval time between successive traversing was 1 s, and particle shifts within this interval were less than 2 mm (much less than the particle diameter), hence correspondences between particle images in successive traversing were assured. From the successive measurements of particle positions, velocities of all particles were calculated.

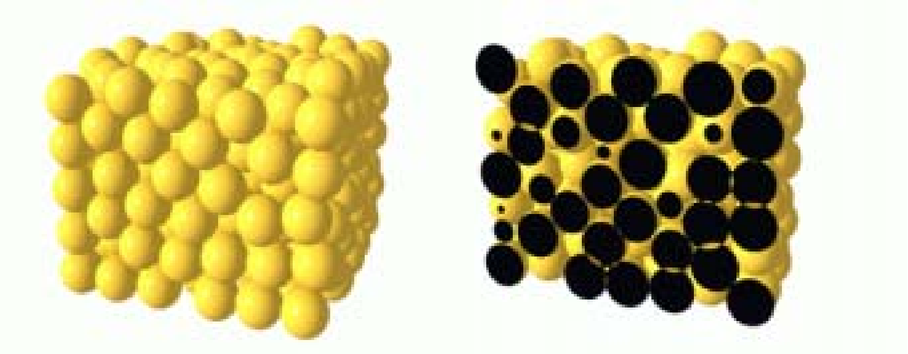

Fig. 3 Reconstruction of all particles in fluidization. Left: perspective view of instantaneous positions of particles. Right: cross section at $\mathbf{z} = 50$ mm.

Reconstructed distribution of particles during one traversing process is shown in Fig. 3. The overlapping of cross sections of several particles in Fig. 3(Right) shows an existence of errors in the measurement.

Velocity vectors of particles during one intervals is shown in Fig. 4. This figure shows a random distribution of vectors, as was expected. However, in some cases velocity vectors were aligned to the same direction (not shown in this figure), which is an unnatural situation because the particles were confined in a finite container. This was caused by the systematic error mentioned above.

After all, the present results show that this method of measurement works well. And, at the same time there is still a room for improvement.

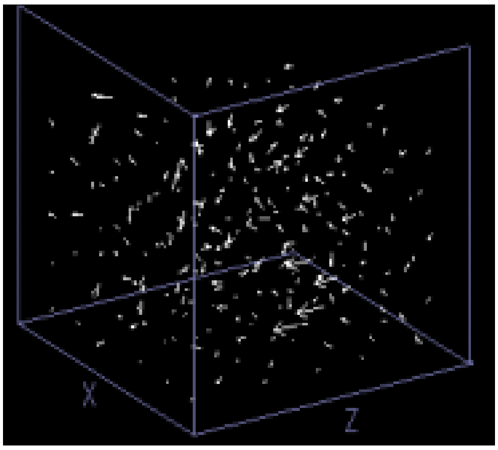

Fig. 4 Velocity vectors of all particles obtained from particle positions at 2 instants.

4. CONCLUSION

The new method of measurement of particle positions in 3D liquid-particle system was confirmed to work well if some optical conditions are satisfied. The systematic error mentioned in the preceding section will be eliminated by setting one stationary particle at a place where it does not disturb motions of other particles.

This method has a room for improvement to match to various needs of researches. For example, if particles have various diameters or various shapes one needs more number of cross sections and a sophisticated algorithm to treat them. However, this method will be developed it to a standard method for studying particle behavior in 3D systems. Possible fields to which this method can be applied would be the chemical engineering, the soil mechanics, the physics of condensed matter, etc. However, it should be noted also that this method can not be applied to real systems, because it requires severe conditions on optical properties of material in experiment. Therefore, this method will be powerful in model experiments of liquid particle systems.

REFERENCES

[1] HORIO M and KUROKI H: Three-dimensional flow visualization of dilutely dispersed solids in bubbling and circulating fluidized beds, ***Chem. Eng. Sci***. 1994, **4**9(15), 2413.

[2] KONAGAYA K and TAMURA J: Visualization of dynamical behavior of particle structure, ***Seisan Kenkyu*** (***Monthly J. Inst. Indust. Sci***.), 1988, 40(11),580. [in Japanese]

[3] CHIN H, MIKAMI F and NISHIKAWA S: PTV measurement of natural convection of suspension by the use of fluorescent particles, ***Kashika joho (J.of Visual.),*** 1997, **17**(Suppl.1) 329. [in Japanese]

[4] TAKAKI R: New experimental methods for fluidization research, ***Proceedings of Seminar on Chemical Physics under Microgravity,*** organized by Nat. Space Develop. Agency Jpn., February 2003 at Hachioji.

Proceedings of the Tenth Asian Congress of Fluid Mechanics
17-21 May 2004, Peradeniya, Sri Lanka

THE DANCE OF FALLING LEAVES

H. Satoh, H. Saito and H. Nakamura
Institute of Flow Research, Machida, Tokyo 194-0041, Japan

ABSTRACT: When summer ends, tree leaves start falling. They dance around in air. We planned to perform a systematic investigation on the dance. We used a transparent water tank and dropped various kinds of thin model leaf. Among them the most beautiful dance is performed by the Japanese one-yen coin. The dance by the coin is very regular and reproducible. After hundreds of trial we found that the stable dance is performed by models with axial symmetry. In the process of falling all models turn around the vertical axis and if there is no symmetricity, falling mode changes and the path is randomized. Appropriate conditions for the stable dance were discovered.

1. INTRODUCTION

The dance of falling leaves in autumn is an excellent subject of poems. People feel that the warm summer is gone and the cold winter is coming. The motion of leaf is, from the fluid-dynamical viewpoint, a mixture of regular and random motions. So often we argue if we can predict the motion of leaves by Navier-Stokes equation. We planned a systematical experiment on falling leaves in a laboratory. Our aim is to obtain some insight on the mixed regular and random motions.

2. EXPERIMENTAL ARRANGEMENT

Experiments were performed in a square water tank of which height is about 2 meters and cross-section of 15 cm by 15 cm. Various kinds of simulated leaf were dropped from the top of tank. The material of leaves are either aluminum or plastic plates of which specific weight is larger than 1. Real leaves move around in air. Our experiments are plastic leaves floating in water. They may be some quantitative difference but we may not lose the qualitative features of dancing leaves in a water tank.

Motion pictures were taken from two directions, one from the front and the other form the side by using a mirror set at 45 degrees. By the picture processing technique we could obtain a series of still pictures at a specified time interval.

3. LEAVES

More than 20 kinds of plastic leaf were tested. Among them fig. 1 is an example of regular dancing by an aluminum maple leaf. The left picture is taken from the front, whereas the right picture is taken from the side. Fig. 2 shows an irregular mode of dance played by a plastic ginkgo leaf. It is not easy to predict the performance of leaf from the plan form. Two leaves are not much different in shape but the dance is different. The location of the center of gravity may play an important role.

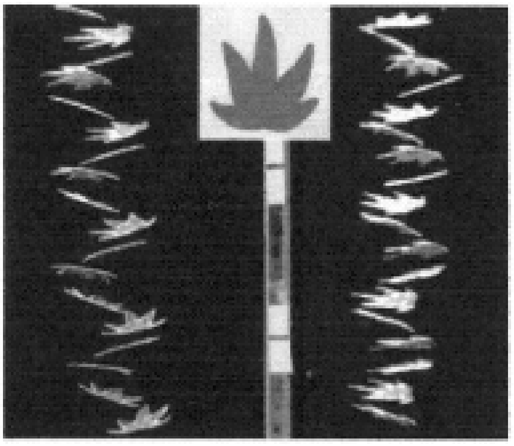

Fig. 1: Maple

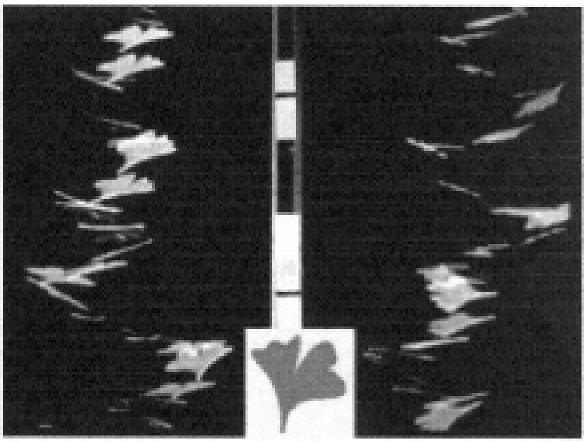

Fig. 2: Ginkgo

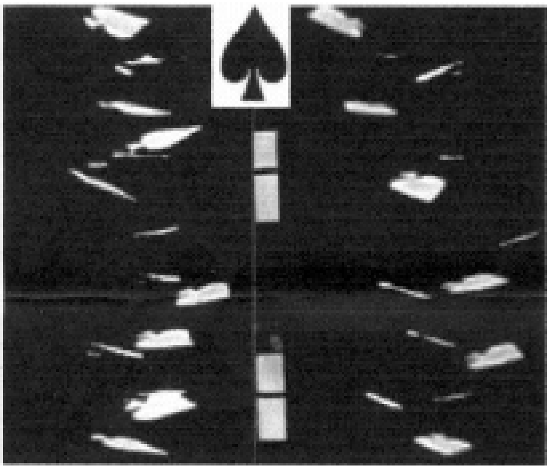

Fig. 3: Spade

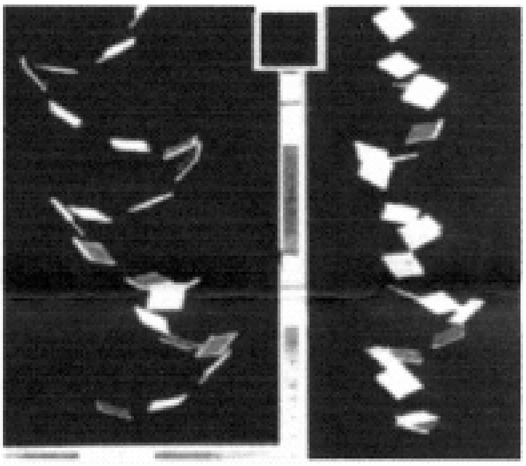

Fig. 4: Rectangle

4. GEOMETRICAL FIGURES

Plastic plates of various geometrical shapes were dropped from the top. Fig. 3 shows the result by a spade-shape of plastic plate of 0.5 mm thickness. The flight in this case is rather irregular. Fig. 4 shows a rectangle. It is a regular dance. From these results it is clear that the axi-symmetricity of plan form is very important for the stable dance.

An excellent regular dance was performed by Japanese one-yen coin as shown in Fig. 5. The coin is circular, made of pure aluminum, the diameter is exactly 2 cm and the mass is exactly 2 grams. The motion is almost periodic and highly reproducible. We can observe that the coin eventually moves upward. This is also observed in Fig. 4.

Two coins pasted back-to-back shows a regular trace as shown in Fig. 6. In this case the mass is doubled but the surface area remains the same. This implies that the regular flight is a result of axisymmetricity rather than the weight itself.

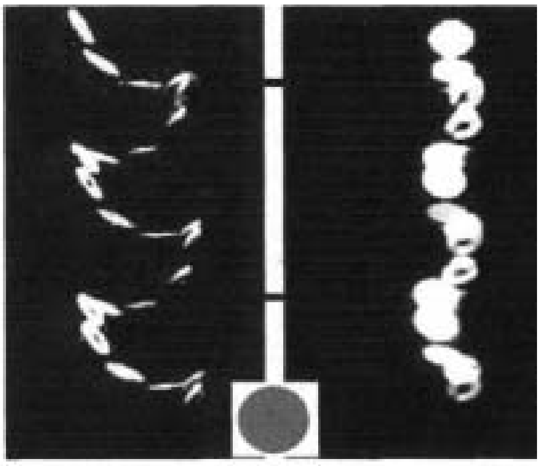

Fig. 5: One-yen coin

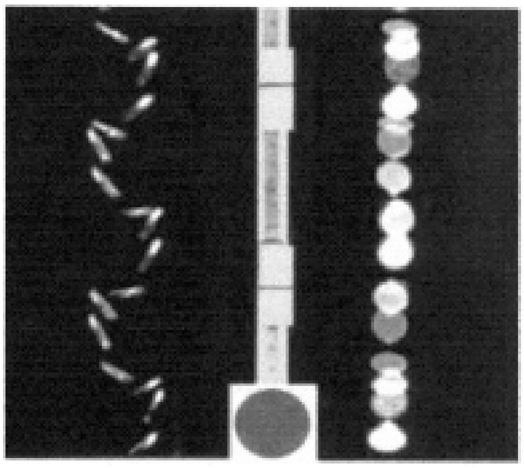

Fig. 6: Pasted two coins

5. DYNAMICS OF FALLING LEAVES

Fig. 7 shows the schematic pattern of falling one-yen coin. It starts from vertical fall with a horizontal face -1, 2. This mode is unstable. The coin tilts and slides. As it falls it picks up speed and the lift force acts on the coin –3, 4. A pitching moment also acts and lifts the leading edge of coin. As a result lift force increases and there is a short period of horizontal slide –5. The lift increases further and exceeds the gravitational force. Due to the lift the coin moves upward as shown in 6 and eventually it stalls. Then the lift is lost and the coin falls backward –7, 8, 9, 10. It picks up the lift and repeats the same pattern –11, 12, 13, 14, 15.

Fig. 8 shows forces acting on the falling leaf. The angle of attack is an important factor for the balance of three forces because the lift force is determined by the angle. The pitching moment is also important.

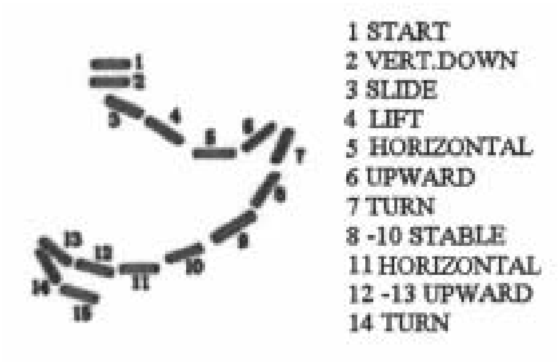

Fig. 7: Flight path

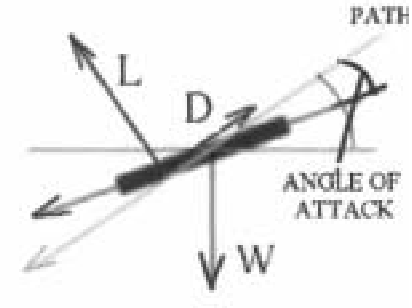

Fig. 8: Force system

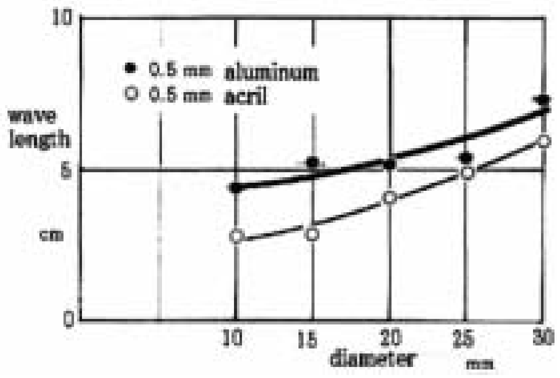

Fig. 9: Diameter and wave length

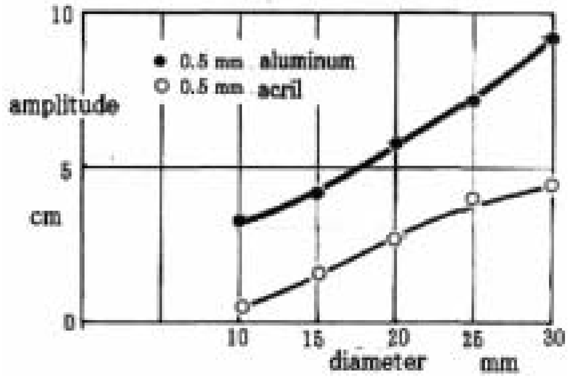

Fig. 10: Diameter and amplitude

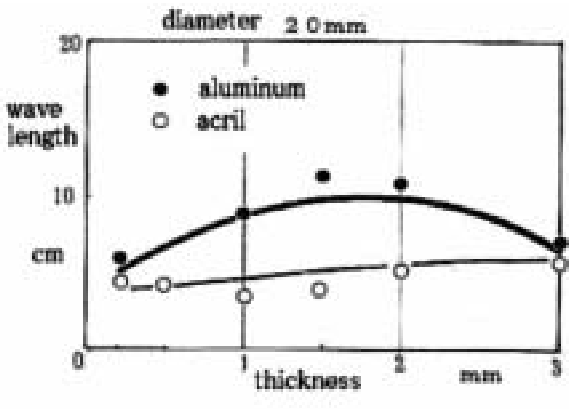

Fig. 11: Thickness and wave length

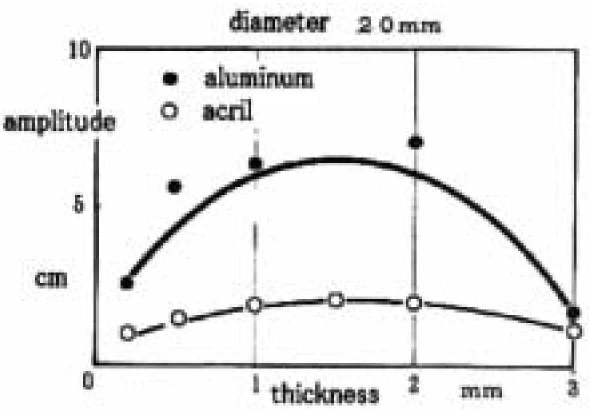

Fig. 12: Thickness and amplitude

In order to understand the effect of shape of leaf on the dance performance a systematic experiment was made with circular models. Two kinds of material with different specific weights, aluminum (s.w. = 2.7) and plastic plate, acryl (s.w. = 1.4) were used. In Figs. 9 and 10 the thickness is kept constant and the diameter was varied. They show the effect on the wave length and amplitude, respectively. As the diameter increases both wave length and amplitude increase.

Fig. 11 and 12 show the effect of thickness on wave length and amplitude. A large-scale dance seems to be performed by an appropriate thickness.

5. CONCLUDING REMARKS

Patterns of dancing falling leaves of various shapes in a water tank were photographed. We found conditions for the stable dance as:

(1) The model should be of appropriate thickness. If it is too thin, it slides too much and does not come back.
(2) The sable flight is supported by the lift due to side slides.
(3) The axi-symmetricity is an important for a stable flight.
(4) The most stable flight is achieved by a circular leaf.

Proceedings of the Tenth Asian Congress of Fluid Mechanics
17-21 May 2004, Peradeniya, Sri Lanka

ELECTRON SHOCK WAVES: DISCONTINUITY CONDITIONS

M. Hemmati
(Department of Physical Science, Arkansas Tech University, Russellville, Arkansas 72801 USA)

ABSTRACT: A one-dimensional, steady-state, three component (electrons, ions, and neutral particles) fluid model is utilized to find analytical solutions to electrical breakdown waves. This model treats the wave front as an electron shock wave moving forward mainly due to the electron impact ionization. The set of equations describing the model will include the equation of conservation of mass, equation of conservation of momentum, and equation of conservation of energy, coupled with Poisson's equation. Inclusion of heat conduction term in the equation of conservation of energy and allowance for the temperature derivative discontinuity at the shock front alters the initial boundary conditions on electron temperature and velocity. This article presents derivation of the discontinuity conditions and the use of these conditions in integration of the electron fluid dynamical equations through the dynamical transition region of the wave. This study will concentrate on antiforce waves, waves for which the electric field force on electrons is in the opposite direction of wave propagation.

1. INTRODUCTION

During the 1920s, based on the examination of the process of formation and distribution of space charge in the long discharge tube, Beams [1] was the first who proposed a qualitative theory consistent with the observed lack of heavy particle motion in the breakdown waves. Beams called them "Potential Waves." However, it was in the 1960s that most of the advances in formulation and understanding of the propagation of breakdown waves took place. Paxton and Fowler [2] formulated a fluid model for breakdown wave propagation. Using a one-dimensional, steady state, three-fluid, hydrodynamical model, they were able to write down the equations of conservation of mass, momentum, and energy. In terrestrial application these wave represent the "dart leader" or "return stroke" observed in lightning strikes.

Nowhere in the theory of the electron waves is the distinction between the concepts associated with Townsend process and the wave process as clearly displayed as in the discontinuity conditions which govern the leading edge of the electrical breakdown wave. It is at the leading edge of the wave that the illusion was created that antiforce breakdown waves could not exist without photo processes. The photo-ionization model assumed that the radiation emitted by the gas is the driving mechanism and it is the fundamental element in propagation of the ionization from one place to another. In Townsend type analysis one must be able to discuss, at the wave front, the parallel acceleration in the field of a group of electrons which were at rest at the instant before attention was directed to them, and that the front of the wave is a transition layer in which this acceleration is taking place. The wave process recognizes the existence of a discontinuity, on one side of which is the electron gas, whose members have gathered there by diffusive mixing from many distant places and have no individual relationship to the mechanical parameters existing at a given point.

2. ANALYSIS

The discontinuity conditions derive from the global differential equations for balance of charge, baryons, mass, momentum, and energy. When stationary solutions are sought, and the space dependant expressions are integrated across a presumed discontinuity with nothing but neutral particles in front of it, one obtains

$$nv \quad N_iV_i = 0, \tag{1}$$

$$N_iV_i + NV = N_0V_0, \tag{2}$$

$$mnv + M_iN_iV_i + MNV = MN_0V_0, \tag{3}$$

$$mnv^2 + M_iN_iV_i^2 + MNV^2 + nkT_e + N_ikT_i + NkT = MN_0V_0^2 + N_0kT_0 + \frac{e_0}{2}(E^2 \quad E_0^2), \tag{4}$$

$$mnv^3 + M_iN_iV_i^3 + MNV^3 + 5nvkT_e + 5N_iV_ikT_i + 5NVkT$$

$$+2nvef_i = MN_0V_0^3 + 5N_0V_0kT_0 - 2q_e. \qquad (5)$$

Where, n, N_i, N, m, M_i, M, T_e, T_i, T, v, V_i, and V are the electron, ion, and neutral particle number density, mass, temperature, and velocity behind the wave front respectively. N_0 and V_0 are the neutral particle number density and velocity in front of the wave respectively, E is the electric field within the wave, E_0 is the electric field at the wave front, f_i is the ionization potential, k is the Boltzman's constant, and q_e is the heat conduction term.

The essence of the electron fluid wave behavior is that there is no mechanism to build up a neutral particle motion at the discontinuity, so $V = V_0$ and $T = T_0$; and since at the wave front ions are produced from the neutral particles by action of the electron gas, they too are unaffected by the wave, so $V_{i1} = V_0$. The time during which the entire wave acts on the gas that it passes through is very brief so that $V = V_0$ and $T = T_0$ remains a good approximation at all times. V_i, however, changes through the wave by a small but significant amount under the direct action of the electric field. Using Equations (1-3), one can modify several terms in the momentum equation as follows

$$\begin{aligned}
&N_ikT_i + NkT = N_ikT + NkT = (N_i + N)kT = N_0kT\\
&M_iN_iV_i^2 = V_i[MN_0V_0 - MNV - mnv] = V_i[MN_0V_0 - M(N_0V_0 - N_iV_i) - mnv] =\\
&\qquad V_i[MN_0V_0 - M(N_0V_0 - nv) - mnv] = MnvV_i - mnvV_i\\
&MNV^2 = MV(N_0V_0 - N_iV_i) = MV(N_0V_0 - nv) = MN_0VV_0 - MnvV\\
&\qquad = MN_0V_0^2 - MnvV_0.
\end{aligned}$$

Substituting the above terms in the momentum equation reduces it to

$$mnv(v - V_i) + Mnv(V_i - V_0) + nkT_e - \frac{e_0}{2}(E^2 - E_0^2) = 0. \qquad (6)$$

The wave front can not be marked by a sudden change in the electric field, because a discontinuity in the electric field results from a surface charge, or from an infinite volume charge density at the wave front, so the electric field, E, has to be equal to E_0 at the wave front. At the wave front the electrons will have a velocity, v_1, a number density, n_1, and a temperature of, T_{e1}, and also the ion and neutral particle velocities are equal that of heavy particle velocity in front of the wave ($V_i = V = V_0$). Using these conditions in Equation (6) reduces it to

$$mn_1[v_1(v_1 - V) + \frac{kT_{e1}}{m}] = 0. \qquad (7)$$

If n_1 and v_1 are not zero, there can be a strong discontinuity, Rankine-Huganot type, with the bracketed quantity conditionally zero. At the wave front, since $n_1 \neq 0$, we obtain the initial condition on electron temperature as follows

$$T_{e1} = \frac{mv_1}{k}(V - v_1). \qquad (8)$$

Since temperature cannot be negative, and zero current condition requires that V and v to have the same sign; therefore,

$$V > v > 0.$$

Introducing dimensionless variables

$$y = \frac{v}{V}, \quad n = \frac{2efn}{e_0E_0^2}, \quad q = \frac{T_ek}{2ef}, \quad h = \frac{E}{E_0}, \quad x = \frac{eE_0x}{mV^2}, \quad w = \frac{2m}{M},$$

$$k = \frac{mVK}{eE_0}, \quad m = \frac{b}{K}, \quad a = \frac{2ef}{mV^2},$$

in Equation (8), we obtain the dimensionless initial condition on electron temperature as follows

$$aq_1 = y_1(1 \quad y_1). \tag{9}$$

Using Equations (1-3) and the above mentioned approximations, several terms within the equation of conservation of energy can be modified as follows

$$\begin{aligned}
&5NVkT + 5N_iV_ikT_i \quad 5kT(N_iV_i + NV) \quad 5N_0V_0kT_0 \\
&M_iN_iV_i^3 = V_i^2[MN_0V_0 \quad MNV \quad mnv] = V_i^2[MN_0V_0 \quad M(N_0V_0 \quad N_iV_i) \quad mnv] \\
&\qquad V_i^2[Mnv \quad mnv] \quad MnvV_i^2 \quad mnvV_i^2 \quad MnvV_i^2 \quad mnvV_0^2 \\
&MNV^3 = MV^2(N_0V_0 \quad N_iV_i) = MV^2(N_0V_0 \quad nv) \quad MN_0V_0^3 \quad MnvV^2
\end{aligned}$$

Substituting the above modifications in Equation (5) we obtain a modified global energy equation as follows

$$mnv(v^2 \quad V_0^2) + Mnv(V_i^2 \quad V^2) + 5nvkT_e + 2envf_i + 2q = 0 \tag{10}$$

At the wave front, Vi = V₀ = V, therefore, equation (10) reduces to

$$mnv(v^2 \quad V^2) + 5nvkT_e + 2envf_i + 2q = 0. \tag{11}$$

The heat conduction term takes the standard form, $\frac{5}{2}\frac{k^2nT}{mK_1}\frac{dT}{dx}$, where K_1 is the elastic collision frequency. Substituting the heat conduction term in the energy equation results in

$$mnv(v^2 \quad V^2) + 5nvkT_e + 2envf_i \quad \frac{5k^2nT_e}{mK_1}\frac{dT_e}{dx} = 0. \tag{12}$$

In dimensionless variables Equation (12) reduces to

$$ny(y^2 \quad 1) + 5anqy + any \quad \frac{5a^2nq}{k}\frac{dq}{dx} = 0,$$

and at the wave front it becomes

$$n_1y_1(y_1^2 \quad 1) + 5an_1q_1y_1 + an_1y_1 \quad \frac{5a^2n_1q_1}{k}\left(\frac{dq}{dx}\right)_1 = 0. \tag{13}$$

Substituting for $_1$ in Equation (13) from Equation (9) and expanding the resulting equation becomes

$$4n_1y_1^3 \quad n_1y_1 + 5n_1y_1^2 + an_1y_1 \quad \frac{5an_1y_1q_1}{k} + \frac{5an_1y_1^2q_1}{k} = 0. \tag{14}$$

Dividing both sides of Equation (14) by $_1$ $_1$, results in the following quadratic equation in $_1$

$$4y_1^2 \quad y_1\left[5 + \frac{5aq_1}{k}\right] + \left[1 \quad a + \frac{5aq_1}{k}\right] = 0. \tag{15}$$

Solving Equation (15) for $_1$ results in

$$y_1 = \frac{5[1+\frac{aq_1}{k}] \pm \sqrt{(3 \quad \frac{5aq_1}{k})^2 + 16a}}{8}. \qquad (16)$$

The condition, V > v> 0, requires that 1 > $_1$ > 0. Therefore, the negative sign in Equation (16) has to be chosen.

For antiforce waves, waves for which the electric field force on electrons is in the opposite direction of wave propagation, the final form of the equations of conservation of mass, momentum, energy, and Poisson's equation in non-dimensional form is (Hemmati [3])

$$\frac{d(ny)}{dx} = kmn\,, \qquad (17)$$

$$\frac{d}{dx}\{ny\,(y \quad 1) + naq\} = nh \quad kn(y \quad 1)\,, \qquad (18)$$

$$\frac{d}{dx} \quad ny\,(y \quad 1)^2 + anq\,(5y \quad 2) + any + ah^2 \quad \frac{5a^2nq}{k}\frac{dq}{dx}$$

$$= \quad wkn\left\{3aq + (y \quad 1)^2\right\}, \qquad (19)$$

$$\frac{dh}{dx} = \quad \frac{n}{a}(y \quad 1). \qquad (20)$$

3. THE NUMERICAL SOLUTIONS AND RESULTS

We will use Hemmati's [3] approach to integrate the set of equations through the dynamical transition region (sheath region) of the wave. At the wave front the electron velocity is less than the wave velocity ($_1$<1); therefore, according to Equation (20), the net electric field intensity will increase until electrons gain speeds in excess of ions and heavy particles (>1). The net electric field then will start decreasing. Since a conductor cannot support an electric field, the magnitude of the electric field has to approach zero at the end of the sheath region (0). Without the supporting potential of the electric field the electrons gradually slow down due to collisions with neutral particles, until their speeds approach that of the ions and heavy particles (1). Using the initial conditions on electron temperature and velocity (Equations 9 and 16), we have been successful in integrating equations (17-20) through the sheath region for antiforce waves propagating into a non-ionized medium. We will present the wave profile for two wave speeds (= 0.05 and   = 1). Our solutions meet the above mentioned conditions (1 and   0) at the end of the sheath region.

Figures 1 and 2 show the net electric field (applied plus space charge field), , as a function of electron velocity, , within the sheath region for antiforce waves propagating into a non ionized medium for   = 0.05 and   = 1 respectively.   = 0.05 represents a wave speed of V = 1.3 x 10^7 m/s, and   = 1 represents a slow wave speed of V = 3.2 x 10^6 m/s. We were also able to integrate the electron fluid dynamical equations for wave speeds as low as V = 2 x 10^6 m/s. Integration of the equations for lower wave speeds becomes very difficult and time consuming.

Figures 3 shows the wave profile for electron

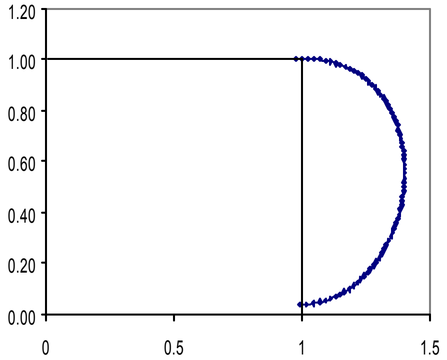

Figure 1. Electric Field as a Function of Electron Velocity Within The Sheath for Alpha = 0.05

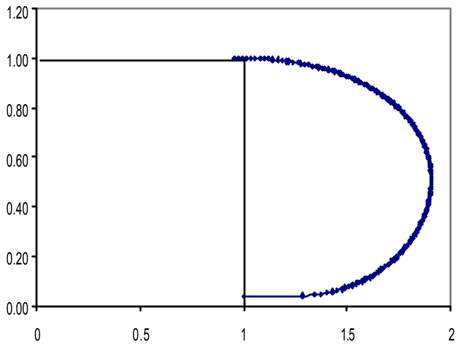

Figure 2. Eleclric Field as a Function of Electron Velocity Within the Sheath for Alpha = 1

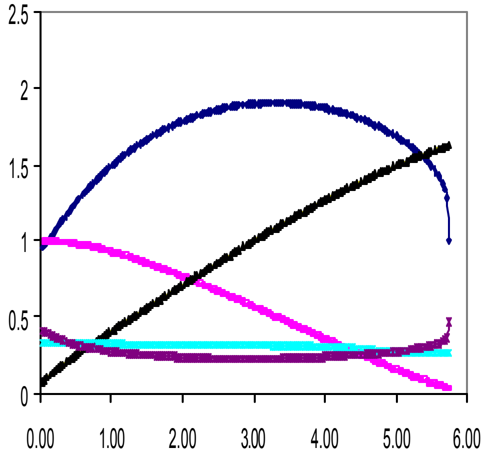

Figure 3. Electric Field, Electron Velocity, Electron Temperature, Ionization Rate, and Electron Number Density as a Function of Position Within the Sheath for Alpha = 1

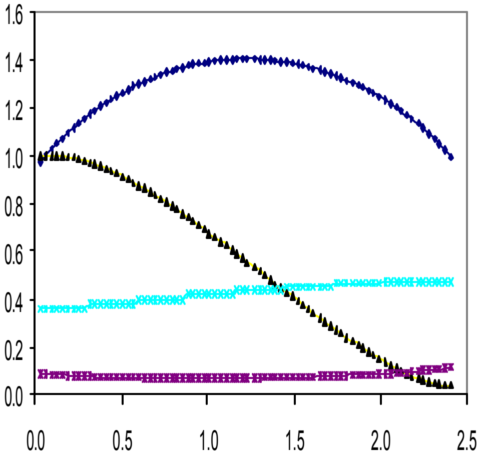

Figure 4. Electric Field, Electron Velocity, Ionization Rate, and Electron Number Density as a Function of Position Within the Sheath for Alpha = 0.05

velocity, , electric field, , electron temperature, , ionization rate, , and electron number density, , as a function of position, , within the sheath for = 1. Figure 4 shows the wave profile for electron velocity, electric field, ionization rate, and electron number density for = 0.05. Figure 5 is a plot of electron temperature as a function of position within the sheath for = 0.05. As the graphs indicate the sheath thickness increases as the wave velocity decreases. = 6 for = 1 represents a sheath thickness of 0.003 m. = 15 for = 0.05 represents an electron gas temperature 8.7 x 10^6 K.

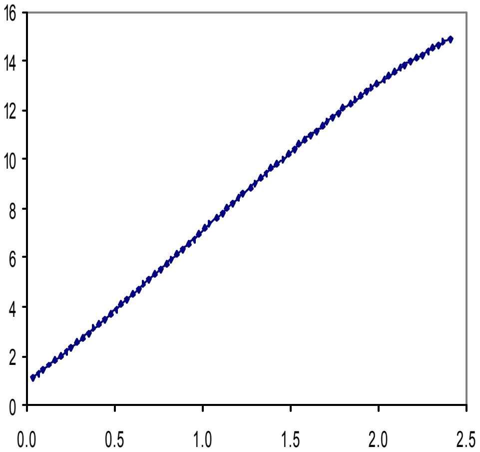

Figure 5. Electron Temperature as a Function of Position Within the Sheath for Alpha = 0.05

4. CONCLUSIONS

Including the heat conduction term in the equation of conservation of energy and allowance for the temperature derivative discontinuity at the shock front results in a new boundary condition equation for electron velocity. Using the new boundary condition equation for electron velocity we were able to integrate the new set of electron fluid dynamical equations through the sheath region of the wave. The results meet the expected conditions at the end of the sheath region. The wave velocities for which the integration of the set of electron fluid dynamical equations become possible compare well with the experimental results reported by Rakov et al. [5]. Practicing engineers and physicists such as Allen et al. [6], who for instance conduct "experimental studies of spark-generated shock wave propagation in CO-laser sustained optically pumped CO-Ar-O_2 plasmas" will find our results useful.

ACKNOWLEGMENTS

The author would like to express his gratitude to the Arkansas Space Grant Consortium for its financial support of this research project.

REFERENCES

[1] Beams, J.W. 1930. The propagation of luminosity in discharge tubes. Phys. Rev. 36:997-1002.
[2] Hemmati M. Antiforce Breakdown Waves: QNR Region. Proceedings of the International Conference on Phenomena in Ionized Gases, Greifswald, Germany, July 2003. Vol. 3, 83-84.
[3] Hemmati M. Antiforce current bearing breakdown waves. Proceedings of The Ninth Asian Congress of Fluid Mechanics, Isfahan, Iran, May 2002, No. 135.
[4] Paxton, G.W. and R.G. Fowler. 1962. Theory of breakdown wave propagation. Phys. Rev. 128:993-997.
[5] Rakov VA, Uman MA, Rambo KJ, Fernandez MI, Fisher RJ, Schnetzer GH, Thottappillil R, Eybert-Berard A, Berlandis JP, Lalande P, Bonamy A, Laroche P, and Bondiou-Clergerie. New insights into lightning processes gained from triggered-lightning experiments in Florida and Alabama. J. Geophys. Res. 1998. NO. D12. 100:14117-14130.
[6] Allen R.W., P. Palm, E. Plonjes, V.V. Subramaniam, and I.V. Adamovich. 2001. Effect of electron density on shock wave propagation in optically pumped plasmas. J. Appl. Phys., Vol. 91, No. 5. 2604-2610.

Proceedings of the Tenth Asian Congress of Fluid Mechanics
17-21 May 2004, Peradeniya, Sri Lanka

Gauge Theory of Ideal Fluid Flows and Variational Formulation

Tsutomu KAMBE[1]

IDS[2]; kambe@gate01.com

ABSTRACT: A new variational formulation is presented for flows of a compressible ideal fluid by defining first a Galilei-invariant Lagrangian. The variation is required to be gauge-invariant (both global and local) with respect to two kinds of symmetry group. By carrying out a gauge-covariant variation, we deduce the Euler's equation of motion.

First symmetry group in the study is the *translation group.* The velocity field consistent with the parallel translational transformation is found to be *irrotational.* Next, we consider a gauge group, *i.e.* $SO(3)$. It will be shown that the new gauge transformation introduces a *rotational* component in the velocity field, *i.e.* the vorticity. In complying with the local gauge invariance, a gauge-covariant derivative is defined by introducing a new gauge field. It is found that the gauge field is the *vorticity* itself. As a result, the covariant derivative of velocity coincides with the so-called *material* derivative of velocity. Thus, from the Hamilton's principle, the Euler's equation of motion for an ideal fluid is derived.

Based on the Noether's theorem, the gauge symmetry with respect to the translation group results in the conservation law of total momentum, while the symmetry with respect to the rotation group results in the conservation law of total angular momentum. In addition, the Lagrangian has a symmetry with respect to particle permutation, which leads to the vorticity equation. Thus, it is found that the well-known equations in fluid mechanics are related to various symmetries of the Lagrangian.

1 INTRODUCTION: FLUID FLOWS AND FIELD THEORY

Study of fluid flows is considered to be a field theory in Newtonian mechanics. In other words, it is a *field theory of mass flow* subject to Galilei transformation. It is well-known that there are various similarities between fluid mechanics and electromagnetism. For example, the functional relation between velocity and vorticity fields is the same as the Biot-Savart law known in the electromagnetism between magnetic field and electric current. One may ask whether the similarity is mere an analogy, or has a solid theoretical background.

In the theory of *gauge field*, a guiding principle is that laws of physics should be expressed in a form that is independent of any particular coordinate system. In the quantum field theory [1, 2], a free-particle Lagrangian is defined first in such a way as having an invariance under Lorenz transformation. Next, a gauge principle is applied to the Lagrangian, requiring it to have a *symmetry*, *i.e.* the gauge invariance. As a result, a gauge field such as the elecromagnetic field is introduced to satisfy *local* gauge invariance. In regard to the fluid flows, relevant symmetry groups are *translation group* and *rotation group* [5].

---

[1] Visiting Professor, Nankai Institute of Mathematics, China

[2] Institute of Dynamical Systems, Higashi-yama 2-11-3, Meguro-ku, Tokyo 153-0043, Japan

We seek a scenario which has a formal equivalence with the gauge theory in the quantum field theory. To that end, we define a Galilei-invariant Lagrangian for fluid flows and examine whether it has a gauge invariance in addition to the Galilei invariance. Applying the gauge principle to the Lagrangian first with respect to translational transformations, we obtain an equation of motion from the action principle. However, the velocity field thus obtained with respect to the translation group must have a potential, *i.e.* is *irrotational.*

Next, we consider an additional transformation with respect to the gauge group $SO(3)$, a *rotation group* in three-dimensional space. The gauge transformation introduces a new *rotational* component in the velocity field (*i.e.* vorticity), even though the original field is irrotational. In complying with the local gauge invariance, a gauge-covariant derivative is defined by introducing a new gauge field Ω. Galilei invariance of the covariant derivative requires that the gauge field Ω should coincide with the *vorticity.* As a result, the covariant derivative of velocity is found to be the so-called *material* derivative of velocity, and the Euler's equation of motion for an ideal fluid is derived from the Hamilton's principle [3]. The Noether's theorem leads to conservation laws associated with the global invariance with respect to the two gauge groups [4]: *i.e.* conservation equations of total momentum and total angular momentum respectively.

In the following sections, we try to formulate the flow field on the basis of the gauge principle. It will be found that the flow fields are characterized by two gauge groups: a translation group and a rotation group. Interestingly, the former is abelian and the latter is non-abelian. So, the flow fields are governed with two different transformation laws.

2 HAMILTON'S PRINCIPLE FOR AN IDEAL FLUID

2.1 Constitutive Conditions

In order to comply with two gauge invariances (translational and rotational), we carry out the material variations under the following three constitutive conditions.

(i) *Kinematic condition*: The trajectory of a material particle in the physical $\boldsymbol{x}$-space, specified by the Lagrangian coordinte $\boldsymbol{a}$, is denoted by $\boldsymbol{x}_a(\tau) = \boldsymbol{x}(\tau, \boldsymbol{a})$, and the particle velocity is

$$\boldsymbol{v}(\boldsymbol{x}, t) = \partial_\tau \boldsymbol{x}(\tau, \boldsymbol{a})\,. \tag{1}$$

All the variations are taken so as to follow such trajectories of material particles. In addition, all the analyses are carried out by keeping mass fixed. As a consequence, the equation of continuity must be satisfied always.

(ii) *Ideal fluid*: An ideal fluid is defined by the property that there is no disspative mechanism within it such as viscous dissipation or thermal conduction ([6], §2, 49). As a consequence, the fluid motion is *isentropic*, *i.e.* the entropy s per unit mass (specific entropy) remains constant following the motion of each material particle. The entropy is not necessarily constant at every spatial point, *i.e.* not necessarily homentropic.

(iii) *Gauge-covariance*: All the expressions of the formulation must satisfy both global and local gauge invariance. Therefore, not only the action $\mathcal{A}$ (defined by (3) just below), but also its varied form must be gauge-invariant. The gauge-covariant derivative $\nabla_t \boldsymbol{v}$

defined by (5) (or (6)) must be used for the variation.

2.2 Lagrangian and Action Principle

Full Lagrangian for flows of an ideal fluid is defined by

$$L_{\mathrm{F}}[\boldsymbol{v},\rho,\epsilon] = \int_M \tfrac{1}{2}\,\langle\,\boldsymbol{v},\boldsymbol{v}\,\rangle\,\rho\,\mathrm{d}V - \int_M \epsilon(\rho,s)\,\rho\,\mathrm{d}V\,, \tag{2}$$

where $\boldsymbol{v} = (v_k)$ is the fluid velocity, ρ the density, and ϵ the internal energy per unit fluid mass, with $\mathrm{d}V$ a volume element, and $\langle\boldsymbol{v},\,\boldsymbol{v}\rangle \equiv \boldsymbol{v}\cdot\boldsymbol{v} = \sum_{k=1}^{3} v_k v_k$ is a scalar product, and M is a bounded space under consideration with $\boldsymbol{x}\in M\subset\mathbb{R}^3$. This Lagrangian is invariant with respect to both the translational [5] and rotational gauge transformations [3, 4]. The action principle is given by $\delta\mathcal{A}=0$, where the action is defined by

$$\mathcal{A} = \int_{t_0}^{t_1} L_{\mathrm{F}}[\boldsymbol{v},\rho,\epsilon]\;\mathrm{d}t. \tag{3}$$

According to the scenario outlined in the previous section, we carry out an *isentropic material variation* satisfying local gauge invariance, and obtain the Euler's equation of motion for an ideal fluid. There are some byproducts from the present formulation. From the global gauge invariance of $SO(3)$, we will obtain a Noether's conservation law, *i.e.* the conservation of total angular momentum of the system, in addition to the conservation of total momentum associated with the translational invariance. Furthermore, the Lagrangian has a symmetry with respect to particle permutation, which leads to a local law of vorticity conservation, *i.e.* the vorticity equation [4].

2.3 Gauge principle

Flow of an ideal fluid is described by a velocity field $\boldsymbol{v}(\boldsymbol{x},t)$, which can be represented by a linear combination of irrotational and rotational parts:

$$\boldsymbol{v}(\boldsymbol{x},t) = \mathrm{grad}\,f + \mathrm{curl}\,B\,. \tag{4}$$

The covariant derivative $\nabla_t\boldsymbol{v}$ is given by

$$\begin{aligned} \nabla_t\boldsymbol{v} &= \partial_t\boldsymbol{v} + \mathrm{grad}(\tfrac{1}{2}\,v^2) + \boldsymbol{\omega}\times\boldsymbol{v} && (5)\\ &= \partial_t\boldsymbol{v} + (\boldsymbol{v}\cdot\nabla)\,\boldsymbol{v}\,, && (6) \end{aligned}$$

which is also composed with irrotational and rotational parts, where $\boldsymbol{\omega} = \nabla\times\boldsymbol{v}$.

The above form of the covariant derivative $\nabla_t\boldsymbol{v}$ is deduced [3, 4] on the basis of the gauge principle [1, 2]. According to the principle, the time derivative $\partial_t = \partial/\partial t$ must be modified so that all the variations as well as the Lagrangian L_{F} are gauge-invariant. Suppose that the time derivative of velocity $\boldsymbol{v}$ is represented such that

$$\nabla_t\boldsymbol{v} = \Delta_t\boldsymbol{v} + \Omega\boldsymbol{v} = \partial_t\boldsymbol{v} + A\boldsymbol{v} + \Omega\boldsymbol{v}, \qquad \Delta_t\boldsymbol{v}_* = \partial_t\boldsymbol{v}_* + A\boldsymbol{v}_*.$$

where A and Ω are linear operators, called *gauge fields*. First, concerning an irrotational flow field $\boldsymbol{v}_* = \mathrm{grad}\,f$, we require that the covariant derivative $\Delta_t\boldsymbol{v}_* = \partial_t\boldsymbol{v}_* + A\boldsymbol{v}_*$ is invariant with respect to *translational* gauge transformation, both global and local. Furthermore, $\Delta_t\boldsymbol{v}_*$ is required to be invariant with respect to Galilei transformation. This determines the gauge operator A [5] such that $A\boldsymbol{v}_* = (\boldsymbol{v}_* \cdot \nabla)\boldsymbol{v}_* = \frac{1}{2}\,\mathrm{grad}(\boldsymbol{v}_*)^2$, where $(\boldsymbol{v}_* \cdot \nabla)(\boldsymbol{v}_*)_k = (\partial_i f)\partial_i(\partial_k f) = (\partial_i f)\partial_k(\partial_i f) = \frac{1}{2}\,\partial_k(\boldsymbol{v}_*)^2$.

Next, it is required that the covariant derivative $\nabla_t \boldsymbol{v} = \Delta_t \boldsymbol{v} + \Omega \boldsymbol{v}$ is invariant with respect to *rotational* gauge transformation $SO(3)$, both global and local. Galilei invariance of $\Delta_t \boldsymbol{v} + \Omega \boldsymbol{v}$ determines the gauge operator Ω which is represented as a skew-symmetric matrix (an element of Lie algebra $\mathbf{so}(3)$). Then, the $\Omega \boldsymbol{v}$ is expressed by a vector product $\hat{\Omega} \times \boldsymbol{v}$, where

$$\hat{\Omega} = \nabla \times \boldsymbol{v} = \boldsymbol{\omega}$$

is the **vorticity**. It is found [3, 4] that the vorticity $\boldsymbol{\omega}$ is the gauge field with respect to the gauge group $SO(3)$. Thus, the covariant derivative (5) is deduced.

The first expression (5) represents two different fields explicitly, derived from two different gauge invariances. The second (6) is the expression of the *material derivative*. It should be noted that the covariant derivative $\nabla_t \boldsymbol{v}$ is invariant with respect to the two gauge transformations: both translational and rotational.

2.4 Material Variation: Rotational and Isentropic

Invariance of the mass $\rho\,\mathrm{d}V$ along the flow, *i.e.* $\mathrm{D}_t(\rho\,\mathrm{d}V) = 0$, is required as a kinematic condition, where $\mathrm{D}_t = \partial_t + \boldsymbol{v} \cdot \nabla$. From this, we obtain the continuity equation:

$$\partial_t \rho + \mathrm{div}(\rho \boldsymbol{v}) = 0. \tag{7}$$

The isentropic condition is represented by $\mathrm{D}_t(s\rho \mathrm{d}V) = 0$. Using (7), we obtain the equation of entropy conservation:

$$\mathrm{D}_t s = \partial_t s + \boldsymbol{v} \cdot \nabla\, s = 0\,. \tag{8}$$

In the material variation, all variations are taken so as to follow particle displacement under the kinematical constraint (7) and the isentropic condition (8).

Writing an infinitesimal variation of the particle position as

$$\boldsymbol{x}_a \mapsto \boldsymbol{x}_a + \boldsymbol{\xi}(\boldsymbol{x}_a, t)\,, \tag{9}$$

the variation field $\delta \boldsymbol{x}_a = \boldsymbol{\xi}(\boldsymbol{x}_a, t)$ is represented by a linear combination of irrotational part and rotational part:

$$\boldsymbol{\xi}(\boldsymbol{x}, t) = \mathrm{grad}\,\varphi + \mathrm{curl}\,\Psi\,. \tag{10}$$

Variation of the particle velocity is given by $\boldsymbol{v}_a \mapsto \boldsymbol{v}_a + \Delta \boldsymbol{v}_a$, where $\Delta \boldsymbol{v}_a = (\boldsymbol{\xi} \cdot \nabla)\boldsymbol{v} + \mathrm{D}_t \boldsymbol{\xi}$ (up to $O(|\boldsymbol{\xi}|)$ terms).

Variations of ρ and ϵ consist of two components: $\Delta\rho = \boldsymbol{\xi} \cdot \nabla\rho + \delta\rho$ and $\Delta\epsilon = \boldsymbol{\xi} \cdot \nabla\epsilon + \delta\epsilon$. It is assumed that their variations are carried out *adiabatically*: $\delta s = 0$.

The proper part of density variation $\delta\rho$ is caused by the displacemnet $\delta \boldsymbol{x}_a = \boldsymbol{\xi}(\boldsymbol{x}, t)$. From the condition of fixed mass variation, we have, $\delta\rho = -\rho\,\mathrm{div}\,\boldsymbol{\xi}$. Then, the proper variation of the internal energy $\epsilon(\rho, s)$ is given by $\delta\epsilon = (p/\rho^2)\,\delta\rho$.

The variation field $\boldsymbol{\xi}(\boldsymbol{x}, t)$ is constrained to be tangential to the boundary surface S of M, and vanishes at both ends t_0, t_1 of the time integration of the action $\mathcal{A}$:

$$\langle \boldsymbol{n}, \boldsymbol{\xi} \rangle = 0, \qquad \text{for } \boldsymbol{x} \in S = \partial M, \quad \text{at any } {}^{\forall}t, \tag{11}$$

$$\boldsymbol{\xi}(\boldsymbol{x}, t_0) = 0, \qquad \boldsymbol{\xi}(\boldsymbol{x}, t_1) = 0, \quad \text{for } {}^{\forall}\boldsymbol{x} \in M, \tag{12}$$

where $\boldsymbol{n}$ is unit outward normal to the boundary S.

3 EULER'S EQUATION OF MOTION

From (3) together with (2), variation of $\mathcal{A}$ is given by

$$\begin{aligned}\delta\mathcal{A} &= \Big[\int_M \langle \boldsymbol{v}, \boldsymbol{\xi}\rangle\,\rho\,\mathrm{d}V\Big]_{t_0}^{t_1} + \int_{t_0}^{t_1}\mathrm{d}t\oint_S p\,\langle \boldsymbol{n}, \boldsymbol{\xi}\rangle\,\mathrm{d}S \\ &\quad -\int_{t_0}^{t_1}\mathrm{d}t\int_M \big\langle \big(\nabla_t\boldsymbol{v} + \rho^{-1}\mathrm{grad}\,p\big),\,\boldsymbol{\xi}\,\big\rangle\,\rho\,\mathrm{d}V, \end{aligned} \tag{13}$$

where p is the pressure. The first line on the right hand side vanishes owing to the boundary conditions (11) and (12). Thus, the action principle $\delta\mathcal{A} = 0$ leads to

$$\nabla_t\boldsymbol{v} + \frac{1}{\rho}\nabla p \;=\; 0\,, \tag{14}$$

for arbitrary variation $\boldsymbol{\xi}$. This is the *Euler's equation of motion.* Using (6),

$$\partial_t\boldsymbol{v} + (\boldsymbol{v}\cdot\nabla)\,\boldsymbol{v} = -\frac{1}{\rho}\nabla p\,. \tag{15}$$

By using (5) and $(1/\rho)\nabla p = \nabla h$ (h: enthalpy), this is equivalently written as

$$\partial_t\boldsymbol{v} + \boldsymbol{\omega}\times\boldsymbol{v} + \nabla(\tfrac{1}{2}\,v^2) = -\nabla h\,. \tag{16}$$

The equation, either (14), (15) or (16), must be supplemented by the equation of continuity (7) and the isentropic equation (8).

4 SUMMARY AND DISCUSSIONS

Guided by the gauge principle in the quantum field theory, we have successfully presented a gauge-covariant variational formulation of ideal fluid flows.

With respect to displacements of material particles, it is required that the Lagrangian should be invariant under transformations of both *parallel translation* group and *rotation* group, and in addition that the variation field of the translational transfromation must be irrotational. The action principle applied first to the variations of the translation group resulted in the equation for potential flows. However, general local gauge transformation of the velocity field $\boldsymbol{v}(x)$ includes rotational components, *i.e.* the *vorticity* $\boldsymbol{\omega}$. The gauge principle requires invariance with respect to both the translation group and the rotation group. In complying with the local gauge invariance (with respec to both transformations), a gauge-covariant derivative is defined in terms of gauge fields. The gauge-field terms $A\boldsymbol{v}$ and $\Omega\boldsymbol{v}$ imply existence of a background *material* field [5].

Using the gauge-covariant derivative, the variational principle is formulated by means of *isentropic material variations*, and the Euler's equation of motion has been derived from the Hamilton's principle, where the Lagrangian density consists of a kinetic energy term and an internal energy term representing the background field. This formulation is considered to unify traditional approaches.

There are byproducts in the present formulation. The global gauge invariances of the Lagrangian with respect to two transfomations (both translation and rotation groups) imply *Noether's conservation laws*, which are the conservations of *total momentum* and *total angular momentum.* In addition, the Lagrangian has an internal symmetry with respect to particle permutation, which leads to the *vorticity equation* [4, 5]. Thus, it is found that all the equations familiar in fluid mechanics are related to various symmetries of the Lagrangian.

The form of Lagrangian (2) is compact with no constraint term, and the variation is carried out adiabatically by following particle trajectories. In the conventional variations [8, 9], the Lagarangian has additional constraint terms which are imposed to obtain rotational component of velocity field[3]. The present variational formulation is nothing but the Hamilton's principle (of a system of point masses) extended to a continuous distribution of massive particles, *i.e.* an ideal fluid.

Present material variation may look similar to that of Bretherton [7] in some respects. However there is an essential difference with the fact that the present covariant derivative (5) has been derived from the gauge principle, whereas Bretherton [7] defines the particle acceleration by (6) in an intuitive way as is always done in fluid dynamics. In the conventional approaches, the formula $\nabla_t \boldsymbol{v} = \partial_t \boldsymbol{v} + (\boldsymbol{v} \cdot \nabla)\boldsymbol{v}$ is taken as a trivial relation for the rate of change of the velocity vector $\boldsymbol{v}$ (acceleration of a material particle). On the other hand, it is not clearly said what principle governs the rate of change of the vorticity vector $\boldsymbol{\omega} = \nabla \times \boldsymbol{v}$, and how the rate of change $\partial_t \boldsymbol{\omega}$ is expressed by the current fields $\boldsymbol{v}$ and $\boldsymbol{\omega}$. Although both of $\boldsymbol{v}$ and $\boldsymbol{\omega}$ are vector fields in $\mathbb{R}^3$, there is some difference between $\partial_t \boldsymbol{v}$ and $\partial_t \boldsymbol{\omega}$ in the expressions in terms of $\boldsymbol{v}$ and $\boldsymbol{\omega}$, which is explained, in the traditional formualtion, only by the procedure that the rate of change of $\boldsymbol{\omega}$ is derived by taking curl of the equation of motion. The present gauge theory provides a theoretical ground for physical analogy between the aeroacoustic phenomena associated with vortices and the electron and electromagnetic-field interactions.

REFERENCES

[1] Frankel, T., 1997. *The Geometry of Physics* (*An Introduction*), Cambridge University Press, Cambridge.

[2] Quigg C., 1983. *Gauge Theories of the Strong, Weak and Electromagnetic Interactions*, Massachusetts: The Benjamin/Cummings Pub. Comp. Inc.

[3] Kambe, T., 2003. Gauge principle for flows of a perfect fluid. *Fluid Dyn. Res.* 32, 193-199.

[4] Kambe, T., 2003. Gauge principle and variational formulation for flows of an ideal fluid. *Acta Mechanica Sinica* **19** (5), 437-452.

[5] Kambe, T., 2003. Gauge-covariant variational formulation of ideal fluid flows. (submitted to *Fluid Dynamics Research*).

[6] Landau L.D. and Lifshitz E.M., 1987. *Fluid Mechanics* (2nd ed), Pergamon Press.

[7] Bretherton F.P., 1970. A note on Hamilton's principle for perfect fluids. *J. Fluid Mech.* **44**, 19–31.

[8] Serrin J., 1959. Mathematical principles of classical fluid mechanics. *Encyclopedia of Physics* (Ed: Flügge, CoEd: Truesdell, Springer-Verlag), 125–263.

[9] Salmon R., 1988. Hamiltonian fluid mechanics. *Ann. Rev. Fluid Mech.* **20**, 225–256.

---

[3] Although the Lin's constraint yields a rotational component, it is shown that the helicity of the vorticity field for a homentropic fluid in which grad $s = 0$ vanishes [7]. Such a rotational field is not general because the knotted vorticity field is excluded.

Proceedings of the Tenth Asian Congress of Fluid Mechanics
17-21 May 2004, Peradeniya, Sri Lanka

ENTRANCE REGION FLOWS OF NON-NEWTONIAN FLUIDS WITH TEMPERATURE DEPENDENT VISCOSITY THROUGH VARIOUS CROSS SECTIONAL DUCTS

S. Gh. Etemad
Chemical Eng. Dept., Isfahan University of Technology, Isfahan, 84155, IRAN

ABSTRACT: This paper deals with a numerical treatment of the laminar entrance region heat transfer of temperature dependent viscosity of power law model non-Newtonian fluids flowing through circular and equilateral triangular channels. The consistency index was assumed to vary exponentially with temperature. Constant wall temperature and constant wall heat flux both axially and peripherally were used as thermal boundary conditions. The effects of variable viscosity on local Nusselt number for Newtonian and non-Newtonian fluids have been investigated and discussed. Results showed the viscosity variation with temperature has significant effects on the local Nusselt number.

1. INTRODUCTION

Pseudoplastic fluids are commonly encountered in various industries such as chemical, biomedical, petrochemical, food, etc. These fluids are usually processed under laminar flow conditions, owing to their high viscosities and the small hydraulic diameter of heat exchangers. The prediction of the laminar heat transfer coefficient and friction factor in circular and non-circular ducts is important to design heat transfer apparatus for different industries. The entrance region has significant effects on the hydrodynamic and heat transfer characteristics and the pressure drop and the Nusselt number in this region is higher than that for fully developed sections.

Most of the pressure drop and heat transfer analysis available in the literature are generally restricted to constant viscosity of the fluids. For most liquids viscosity (μ for Newtonian and *k*, consistency index, for pseudoplastic fluids) vary markedly with temperature. The rheological properties are independent of temperature and can cause serious effects on fluid flow and heat transfer characteristics. Variable viscosity leads to a strong coupling between the motion and energy equations. For constant property Newtonian fluids, Shah and London [1] and Shah and Bhatti [2] have published excellent reviews on laminar flow and heat transfer through various cross sectional ducts. Fluid flow and heat transfer problems involving non-Newtonian fluids have been reviewed by Metzner [3], Skelland [4], Cho and Hartnett [5], Irvine Jr. and Karni [6] and Lawal and Mujumdar [7]. Shin and Cho [8] considered numerically the heat transfer through a rectangular channel with aspect ratio 0.5 when the top plate was heated while the other sides were insulated. They considered viscous non-Newtonian fluids and temperature dependent viscosity and proposed correlation for apparent friction factor and local Nusselt number. Recently, Etemad et al. [9] solved the simultaneously developing entry problem using Galerkin finite element technique for viscous non-Newtonian fluids flowing through non-circular ducts. Etemad et al. [10, 11] and Etemad and Mujumdar [12] presented results which includes the effects of temperature dependent viscosity and viscous dissipation in parallel plates, square ducts and semi-circular channels respectively.

This study was designed to examine at a fundamental level the simultaneously developing flow and heat transfer of temperature dependent, purely viscous, non-Newtonian fluids in circular and equilateral triangular ducts.

2. METHOD

Circular and equilateral triangular cross sections were used as the computational test channels. All fluid properties except viscosity are assumed to be constant. The fluid obeys the power law shear stress shear rate relation given by:

$$\tau = k_o f(T) \left| \frac{1}{2} \left(\Delta : \Delta \right) \right|^{\frac{n-1}{2}} \Delta \tag{1}$$

The temperature dependence of consistency index, *f(T)*, is formulated as:

$$f(T) = e^{B'(T - T_o)} \tag{2}$$

Neglecting effects of viscous dissipation, the governing equations for steady incompressible flow in nondimensional form are:

Continuity:
$$\frac{\partial U}{\partial X} + \frac{\partial V}{\partial Y} + \frac{\partial W}{\partial Z} = 0 \tag{3}$$

x-Momentum:
$$U\frac{\partial U}{\partial X} + V\frac{\partial U}{\partial Y} + W\frac{\partial U}{\partial Z} = -\frac{\partial P}{\partial X} + \frac{1}{\mathrm{Re}}\left(\frac{\partial C}{\partial X} + \frac{\partial D}{\partial Y} + \frac{\partial E}{\partial Z}\right) \tag{4}$$

y-Momentum:
$$U\frac{\partial V}{\partial X} + V\frac{\partial V}{\partial Y} + W\frac{\partial V}{\partial Z} = -\frac{\partial P}{\partial Y} + \frac{1}{\mathrm{Re}}\left(\frac{\partial F}{\partial Y} + \frac{\partial D}{\partial X} + \frac{\partial G}{\partial Z}\right) \tag{5}$$

z-Momentum:
$$U\frac{\partial W}{\partial X} + V\frac{\partial W}{\partial Y} + W\frac{\partial W}{\partial Z} = -\frac{\partial P}{\partial Z} + \frac{1}{\mathrm{Re}}\left(\frac{\partial H}{\partial Z} + \frac{\partial G}{\partial Y} + \frac{\partial E}{\partial X}\right) \tag{6}$$

Energy:
$$U\frac{\partial \theta}{\partial X} + V\frac{\partial \theta}{\partial Y} + W\frac{\partial \theta}{\partial Z} = \frac{1}{Pe}\left(\frac{\partial^2 \theta}{\partial X^2} + \frac{\partial^2 \theta}{\partial Y^2} + \frac{\partial^2 \theta}{\partial Z^2}\right) \tag{7}$$

where:

$$C = 2\left(\frac{\Pi}{2}\right)^{\frac{n-1}{2}} \frac{\partial U}{\partial X} F(\theta) \quad ; \quad D = \left(\frac{\Pi}{2}\right)^{\frac{n-1}{2}} \left(\frac{\partial U}{\partial Y} + \frac{\partial V}{\partial X}\right) F(\theta)$$

$$E = \left(\frac{\Pi}{2}\right)^{\frac{n-1}{2}} \left(\frac{\partial U}{\partial Z} + \frac{\partial W}{\partial X}\right) F(\theta) \quad ; \quad F = 2\left(\frac{\Pi}{2}\right)^{\frac{n-1}{2}} \frac{\partial V}{\partial Y} F(\theta) \tag{8}$$

$$G = \left(\frac{\Pi}{2}\right)^{\frac{n-1}{2}} \left(\frac{\partial V}{\partial Z} + \frac{\partial W}{\partial Y}\right) F(\theta) \quad ; \quad H = 2\left(\frac{\Pi}{2}\right)^{\frac{n-1}{2}} \frac{\partial W}{\partial Z} F(\theta)$$

$$\frac{\Pi}{2} = \left\{ 2\left[\left(\frac{\partial U}{\partial X}\right)^2 + \left(\frac{\partial V}{\partial Y}\right)^2 + \left(\frac{\partial W}{\partial Z}\right)^2\right] + \left(\frac{\partial U}{\partial Y} + \frac{\partial V}{\partial X}\right)^2 + \left(\frac{\partial W}{\partial Y} + \frac{\partial V}{\partial Z}\right)^2 + \left(\frac{\partial U}{\partial Z} + \frac{\partial W}{\partial X}\right)^2 \right\}$$

The dimensionless parameters in the preceding equations are defined as:

$$U = \frac{u}{u_e}, V = \frac{v}{u_e}, W = \frac{w}{u_e}, X = \frac{x}{D_h}, Y = \frac{y}{D_h}, Z = \frac{z}{D_h}$$

$$P = \frac{p - \rho g z}{\rho u_e^2}$$

$$Re = \frac{\rho u_e^{2-n} D_h^n}{k_0}, \quad Pr = \frac{k_0 C_p \left(\frac{u_e}{D_h} \right)^{n-1}}{K} \tag{9}$$

For the constant wall temperature boundary condition (T):

$$\theta = \frac{T - T_w}{T_e - T_w} \qquad F(\theta) = e^{B\theta(T_e - T_w)} = e^{B\theta} \tag{10}$$

For the constant wall heat flux boundary condition (H2):

$$\theta = \frac{T - T_e}{\frac{qD_h}{K}} \qquad F(\theta) = e^{B'\theta q\frac{D_h}{K}} = e^{B\theta} \tag{11}$$

In the solution and analysis of the governing equations the following dimensionless groups are of most interest:

Dimensionless axial distance:
$$x^* = \frac{x}{D_h \, Re \, Pr} = \frac{x^+}{Pr} \tag{12}$$

The velocity profile as well as temperature profile at the entrance are uniform, so that the boundary conditions are:

$$X = 0 \quad \begin{cases} U = 1, V = 0, W = 0 \\ \theta = 1 \quad \textit{for T boundary condition} \\ \theta = 0 \quad \textit{for H2 boundary condition} \end{cases} \tag{13}$$

At the walls of the ducts the velocities are set at zero. For T boundary condition the dimensionless temperature at the walls is zero and for H2 boundary condition the dimensionless heat flux is unity. Due to the long length of the channels outflow boundary conditions are assumed at the exit section.

Equations 3-7 were solved numerically employing Galerkin finite element method using FIDAP (a fluid dynamic and heat transfer analysis package). The flow domain was discretized and the governing equations were converted to algebraic equations using appropriate grids which were based on the requirement of mesh independence of the solutions. For the pressure, the penalty approach was chosen with the penalty parameter set at 10^{-9} . The velocity and temperature gradients in the entrance region and close to walls are high, and therefore a finer mesh distribution were used in this region. The streamline upwinding formulation was used to improve numerical instability. The iteration was ended when the relative error was less than 10^{-4} . A combination strategy used to solve the algebraic equations which starts with the fixed iteration method and then switches to the quasi-Newton-Raphson approach. The results of fully developed and constant viscosity conditions obtained from this investigation were compared with available analytical data in the literature and showed excellent agreement.

3. RESULTS

Figure 1 (a-d) presents $Nu_{T,x}$ and $Nu_{H2,x}$ for $n=0.5$ for two duct geometries. For both T and H2 boundary conditions considering temperature-dependent viscosity enhance Nusselt number which is due to the higher velocity close to the walls.

For the T boundary condition, a large difference between the wall and the bulk fluid temperature exists close to the entrance, therefore considering temperature-dependent viscosity induces significant changes in the velocity gradient close to the wall. On the other hand, the axial velocity profile in the entrance region is quite flat and the velocity and velocity gradient close the wall are rather high; therefore the temperature-dependence of viscosity does not produce large effects on the velocity profile. Competition between these two factors affects both the pressure drop and the Nusselt number. For example at $x^*=0.0002$ the enhancement of $Nu_{T,x}$ for $n=0.5$ and $B=1.5$ is about 18.8 % and 11.5 % relative to the constant viscosity condition for circular and triangular ducts, respectively.

For the H2 boundary condition by reason of small temperature difference between the channel walls and the bulk temperature and also because of the relatively flat velocity profiles at locations close to the entrance, the effect of variable viscosity is negligible in this section. Further downstream the increase in ($\theta_{w,x} - \theta_{b,x}$) and development of the velocity make these effects more notable. At $x^*=0.0002$ for $n=0.5$ and $B=-1.5$, $Nu_{H2,x}$ increases by only 1.4 % relative to constant viscosity condition for the triangular duct among all studied geometries, while at $x^*=0.01188$ increases of 4.9 % and 10.6 % are observed for circular and triangular ducts, respectively. Comparison of the $Nu_{T,x}$ and $Nu_{H2,x}$ results show smaller effect of temperature-dependent viscosity for the H2 boundary condition.

4. CONCLUSION

The numerical simulations considered the effects of temperature dependent viscosity on simultaneously developing flow and heat transfer of power law model non-Newtonian fluid flowing through circular and equilateral triangular ducts. Results are given for T and H2 boundary conditions and for fluids of different power law indices. Viscosity variation with temperature affects the local Nusselt number. For heating, the increase in the local Nusselt number for constant temperature boundary conditions in noticeably higher than that for the constant heat flux boundary conditions.

4. REFERENCES

[1] Shah R. K. and London A. L.: Laminar flow forced convection in ducts. *Advances in Heat Transfer* ed. by Irvine, Jr. T.F. and Hartnett J.P., Academic press, New York, 1978.

[2] Shah R. K. and Bhatti M. S.: Laminar Convection Heat Transfer in Ducts. *Handbook of Single-Phase Convective Heat Transfer* ed. by Kakac S., Shah R.K. and Aung W., John Wiley & Sons, 1987.

[3] Metzner A. B.: Heat Transfer in Non-Newtonian Fluids. *Advances in Heat Transfer* edited by Irvine,Jr. T. F. and Hartnett J. P. Academic press, New York, 1965.

[4] Skelland A. H. P.: *Non Newtonian Flow and Heat Transfer.* John Wiley & sons Inc., 1967.

[5] Cho Y. I. and Hartnett J. P.: Non-Newtonian Fluids. *Handbook of Heat Transfer Applications* ed. by Rohsenow W.M., Hartnett J.P. and Gonic E.N., McGraw Hill Book Co., 1985.

[6] Irvine Jr. T. F. and Karni J.: Non-Newtonian Fluid Flow and Heat Transfer. *Handbook of Single-Phase Convective Heat Transfer* Edited by Kakac, S., Shah, R. K., and Aung, W. , John Wiley & Sons, 1987.

[7] Lawal A. and Mujumdar A. S.: Laminar Duct Flow and Heat Transfer to Purely Viscous Non-Newtonian Fluids. *Advances in Transport Processes.* Edited by Mujumdar, A. S. and Mashelkar, R. A. Wiley Eastern, New Dehli,1989.

[8] Shin S. and Cho Y.I.: Laminar Heat Transfer in a Rectangular Duct with a Non-Newtonian Fluid with Temperature-Dependent Viscosity. *Int. J.Heat Mass Transfer,* 1994, **37**, Suppl, 19-30.

[9] Etemad S. Gh., Mujumdar A. S. and Nassef R.: Simultaneously Developing Flow and Heat Transfer of Non-Newtonian Fluids in Equilateral Triangular Duct. *Appl. Math. Modelling*, 1996, **20**, 898-907.

[10] Etemad S. Gh., Mujumdar A. S. and Huang B.: Viscous Dissipation Effects in Entrance Region Heat Transfer for a Power law Fluid Flowing between Parallel Plates. *Int. J. Heat and Fluid Flow,*1994, **15**, 122-131.

[11] Etemad S. Gh., Mujumdar A. S. and Huang B.: Laminar Forced Convection of a Non-Newtonian Fluid in the Entrance Region of a Square Duct with Different Boundary Conditions. *Proceeding of 10th Int. Heat Transfer Conference,* Brighton, U.K.,1994, **4**, 231-236.

[12] Etemad S. Gh. and Mujumdar A. S.: Effects of Variable Viscosity and Viscous Dissipation on Laminar Convection Heat Transfer of a Power Law Fluid in the Entrance Region of a Semi-Circular Duct. *Int. J. Heat Mass Transfer*, 1995, **38**, 2225-2238.

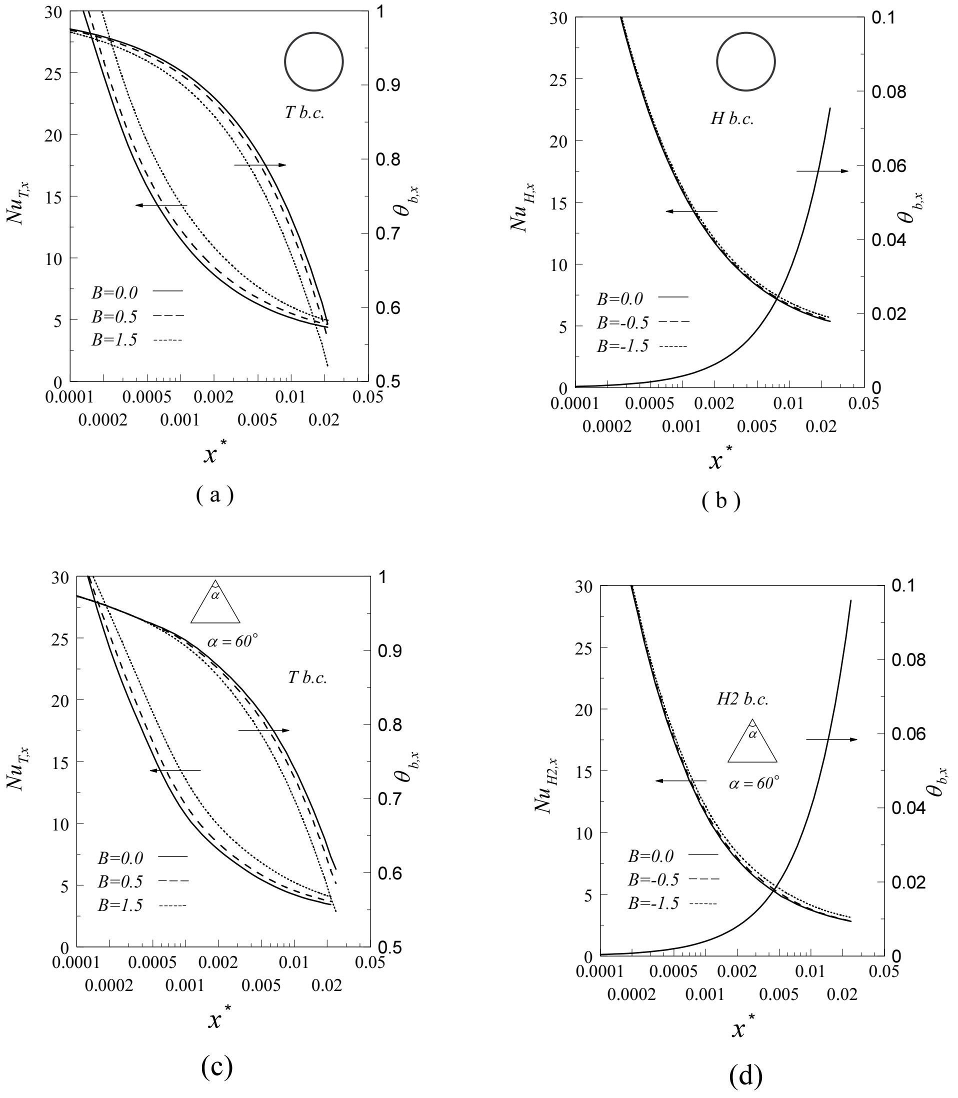

(a) (b) (c) (d)

Figure 1(a - d) Effect of temperature-dependent viscosity on the Nusselt number for circular and triangular duct, *Re=500, Pr=10.*

Proceedings of the Tenth Asian Congress of Fluid Mechanics
17-21 May 2004, Peradeniya, Sri Lanka

A NUMERICAL STUDY ON INJECTION SYSTEM IN SUPERSONIC FLOW

Rafiqul Hoque
Institute of Information and Communication Technology, BUET, Dhaka 1000, Bangladesh

Mohammad Ali
Department of Mechanical Engineering, BUET, Dhaka 1000, Bangladesh

ABSTRACT: The present study involves the investigations of supersonic flow and mixing fields with the injection. Numerical simulations are performed by the two-dimensional Navier-Stokes equations. The focus of this paper is to study the means of increasing the penetration and mixing efficiencies. The distance of injector position from left wall is varied. The investigations show that shorting the distance of the injector from the wall increases the mixing efficiency but decreases the flame holding capability. For a moderate distance of 20 mm, the configuration could act as a good flame holder and efficient in mixing. With long distance both the mixing efficiency and flame holding capability are reduced.

1. INTRODUCTION

Mixing of fuel with oxidizer and their combustion are encountered in many engineering applications. Particularly, the fuel injection in both supersonic and hypersonic streams requires special attention for efficient mixing and stable combustion. Though considerable volume of research has been carried out on mixing and combustion of fuel with supersonic air stream, still it faces many unresolved problems. The main problems that arise in this regard concern mixing of reactants, ignition, flame holding, and completion of combustion. Investigations are required to overcome these problems. In fact, in supersonic combustion, high penetration and mixing of injectant with main stream is difficult due to their short residence time in combustor. In an experimental study, Brown et al. [1] showed that the spreading rate of a supersonic mixing layer decreased drastically with increasing free stream Mach number. A similar conclusion was drawn by Papamoschou et al. [2] on the basis of a theoretical analysis of shear-layers. These investigations showed that difficulty exists in achieving a high degree of mixing in high Mach number flows. There exist several methods of fuel injection in supersonic stream. Perpendicular injection causes rapid mixing of injectant with main stream and is used to some degree at all flight Mach numbers to promote mixing particularly in upstream portion of the combustor. This study is a part of the M.Sc. research done of Hoque [4] where the effect of injector position from left boundary is investigated for a constant Mach number. The geometric configuration of the calculation domain and the inlet conditions of main and injecting flows is shown in Fig. 1. In all cases, the left boundary of domain consists of a backward facing step of height 5 mm, a main

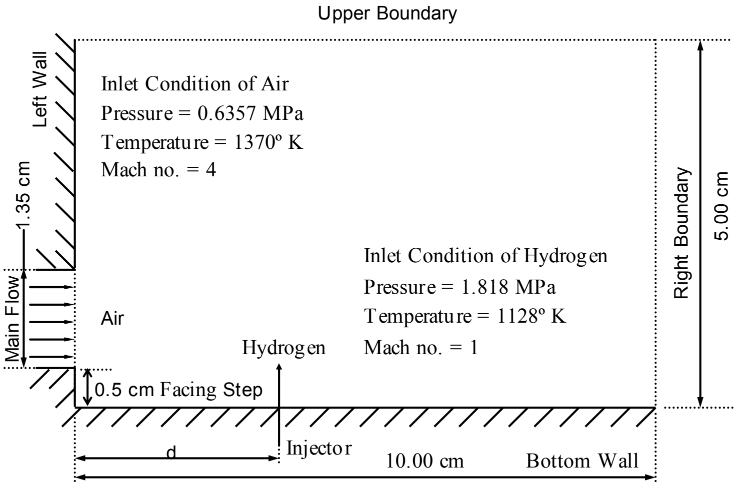

Fig. 1 Geometric Configuration

flow inlet of height 1.35 cm and a solid wall of height 3.6 cm. The backward facing step of 5 mm was used because it was found to be most efficient in mixing for the conditions considered by Ali et al [5]. In this study the parameter is injector distance. The inlet conditions of air are as in Weidner et al [6]. A Mach number of 4 was used while the distance of the injector was varied from left boundary (2, 3, 4, 5 cm) as variable and investigated the penetrating and mixing efficiency. The inlet widths of air and side jet are as, in Ali et al [7], which showed good performance in mixing. Throughout the study, a grid system of 194 nodes in the longitudinal direction and 121 in the transverse direction was used.

2. MATHEMATICAL DESCRIPTION

The flow field is governed by the unsteady, two-dimensional Navier-Stokes and species continuity equations. The body forces are neglected. With the conservation-law form, these equations can be expressed by

$$\frac{\partial U}{\partial t}+\frac{\partial F}{\partial x}+\frac{\partial G}{\partial y}=\frac{\partial F_v}{\partial x}+\frac{\partial G_v}{\partial y} \qquad (1.1)$$

Where

$$U=\begin{pmatrix}\rho\\ \rho u\\ \rho v\\ E\\ \rho Y_i\end{pmatrix},\ F=\begin{pmatrix}\rho u\\ \rho u^2+p\\ \rho u v\\ (E+p)u\\ \rho Y_i u\end{pmatrix},\ G=\begin{pmatrix}\rho v\\ \rho u v\\ \rho v^2+p\\ (E+p)v\\ \rho Y_i v\end{pmatrix}$$

$$F_v=\begin{pmatrix}0\\ \sigma_x\\ \tau_{xy}\\ \sigma_x u+\tau_{yx}v-q_x\\ -\dot{m}_x\end{pmatrix},\ G_v=\begin{pmatrix}0\\ \tau_{yx}\\ \sigma_y\\ \tau_{xy}u+\sigma_{yv}-q_y\\ -\dot{m}_x\end{pmatrix}$$

$$p=\sum_{i=1}^{ns}\rho_i R_i T=\sum_{i=1}^{ns}\rho_i\frac{R}{W_i}T, \qquad (1.2)$$

$$E=\sum_{i=1}^{ns}\rho_i h_i-\sum_{i=1}^{ns}\rho_i\frac{R}{W_i}T+\frac{\rho}{2}\left(u^2+v^2\right),$$

$$E=\sum_{i=1}^{ns}\rho_i C_{pi}T-\sum_{i=1}^{ns}\rho_i\frac{R}{W_i}T+\frac{\rho}{2}\left(u^2+v^2\right), \qquad (1.3)$$

$$\sigma_x=\lambda\left(\frac{\partial u}{\partial x}+\frac{\partial v}{\partial y}\right)+2\mu\left(\frac{\partial u}{\partial x}\right), \qquad \sigma_y=\lambda\left(\frac{\partial u}{\partial x}+\frac{\partial v}{\partial y}\right)+2\mu\left(\frac{\partial v}{\partial y}\right),$$

$$\tau_{xy}=\tau_{yx}=\mu\left(\frac{\partial u}{\partial y}+\frac{\partial v}{\partial x}\right), \qquad \lambda=-\frac{2}{3}\mu \qquad (1.4)$$

3. RESULTS AND DISCUSSION

Results of varying distance are to be analyzed and discussed under the following subsections; (i) the physics of fluid dynamics in both upstream and downstream of the injector (ii) penetration and mixing of hydrogen under the variation of these parameters.

3.1 The Physics of Fluid Dynamics

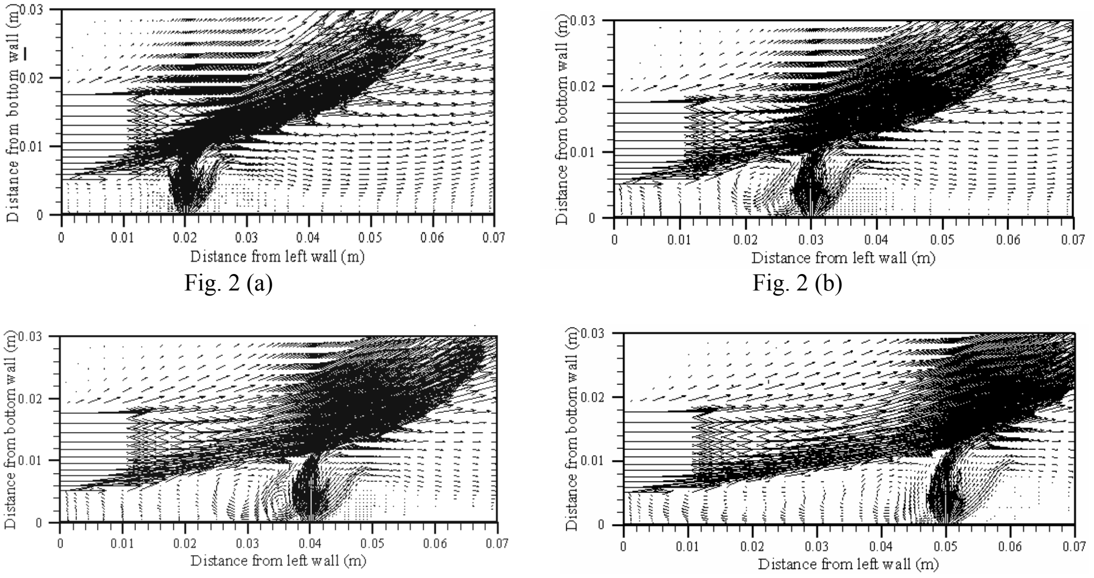

Fig. 2 (a)

Fig. 2 (b)

Fig. 2 (c)

Fig. 2 (d)

Fig. 2 Velocity vector near injector; (a) case -1 (d=20mm), (b) case -2 (d=30mm) , (c) case -3 (d=40mm), (d) case -4 (d=50mm)

The physics of flow is important to understand the penetration and mixing of hydrogen, which is the special interest of this study. Figure 2(a~d) shows the velocity vector in both upstream and downstream of injector. Strong interaction is occurring between the main and injecting flows in case 1 shown in Figure 2(a). The strength of interaction can be understood from the slope of vectors at the top of injector. For long distance of injector position both main and injecting flows lose their strength due to viscous action and upstream recirculations. There are two recirculations in upstream of the injector observed in figure 2(b), (c) and (d). Due to small space in upstream, two very small recirculations (one is primary and the other is secondary) exist. With the increase in distance of injector the recirculations are increasing in areas and the primary one expands towards the left though the pattern of expansion is different. In case 1, recirculations are not strong and the upstream region is seemed to be stagnant, whereas cases 2 ~ 4 have strong recirculations due to wide space in upstream. In the downstream no strong recirculation exists.

3.2 Penetration and Mixing of Hydrogen

Figure 3(a~d) shows the penetration and mass concentration of hydrogen in the flow field. There are various definitions of penetration in literature. In this paper the term penetration refers to the edge of mixing region in the vertical direction where the mole fraction of hydrogen is 5%. Accordingly figure 3 shows that there is little difference in penetration at both upstream and downstream of the configurations. Two competing phenomena are activated in this regard; (i) due to strong interaction in small distance of injector, high gradient of hydrogen mass concentration exists causing high penetration of hydrogen, and (ii) in longer distance of injector, large and elongated upstream recirculation causes high penetration dominated by convection of recirculation. The mass concentration of hydrogen in upstream and that in downstream can be explained separately. For short injector distance, most of the upstream region contains high concentration of hydrogen. It can be pointed out that the flame holding requires longer residence time of flame in the burning range and this residence time strongly depends on the geometric expansion

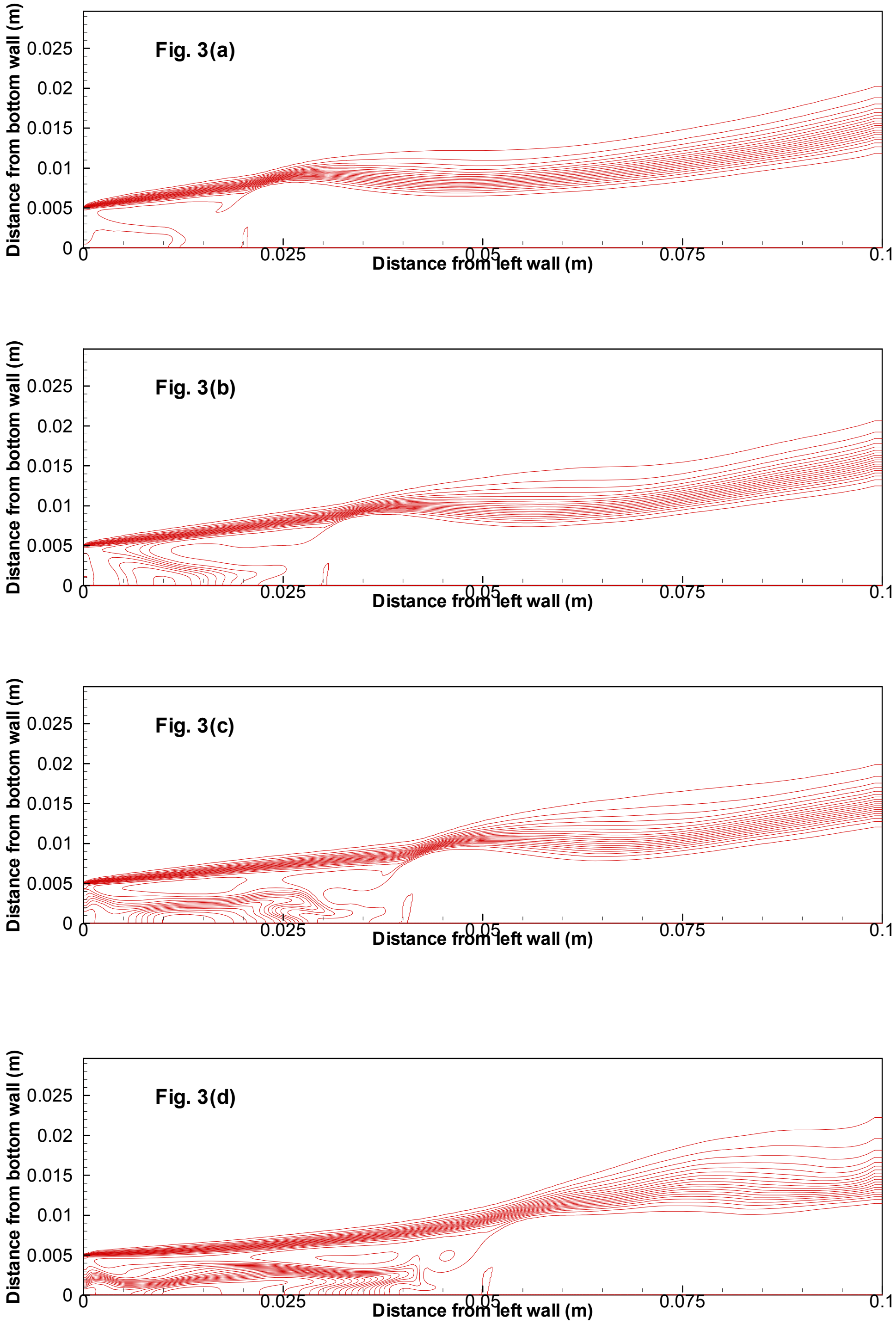

Fig. 3 Mole fraction counter of Hydrogen, Φ(0.05, 1.0, 0.05); (a) case -1 (d=20mm), (b) case -2 (d=30mm), (c) case -3 (d=40mm), (d) case - 4 (d=50mm)

of the recirculation zone [8]. Also the equivalence ratio of fuel and oxidizer in mixture is an important factor for burning because among the mixture, the stoichiometric strength is good for combustion. Therefore, longer recirculation zone containing stoichiometric mixture strength results in a longer residence time and leads to a more stable flame. The cases having injector distance d = 20, 30 and 40 mm can produce larger and elongated upstream recirculation where most of the region contains good proportion of hydrogen and oxygen (mole fraction is about 0.4~0.7) exists. Again for d = 50 mm, far upstream (d = 0~17.5 mm) contains lower mass concentration of hydrogen which is not good for flame holding. In far downstream the hydrogen distribution is seemed to be better (more uniform) in cases 3 ~ 4 than that in cases 1 ~ 2. This uniform distribution of hydrogen is caused by higher expansion of side jet. However, the uniform distribution does not mean higher mixing efficiency, which will be discussed later. The performance of different cases is evaluated by calculating mixing efficiency. Mathematically, the mixing efficiency is defined by

$$\eta_m = \frac{\int_A \left(f_H \ \rho \vec{u} \ d\vec{A} \right) / \phi'}{\dot{m}_H / \Phi}$$

Where,

A = arbitrary section plane

f_H = local mass fraction of hydrogen

ρ = total density

$\vec{u}$ = velocity vector

$d\vec{A}$ = small area normal to velocity vector

$\dot{m}_H$ = total mass flux of hydrogen

$\phi' = \text{local equivalence ratio} = \begin{cases} 0.25 & \phi' < 0.25 \\ \phi' & \phi' \geq 0.25 \end{cases}$

$\Phi = \text{global equivalence ratio} = \begin{cases} 0.25 & \Phi < 0.25 \\ \Phi & \Phi \geq 0.25 \end{cases}$

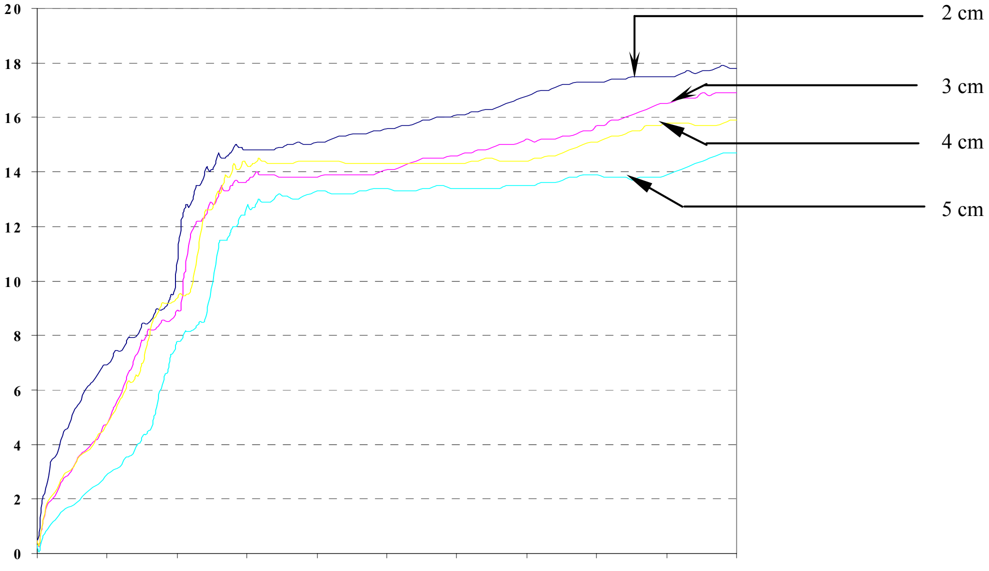

Figure 4 Mixing efficiency

Figure 4 shows mixing efficiency along the length of physical model for different cases. In upstream region, the increasing rate of mixing is moderate and in downstream it is very slow. Individually, case 1 has the highest increment of mixing efficiency at injector position due to strong interaction of main and injecting flows as discussed earlier. Besides, case 4 shows that in upstream the overall mixing efficiency (about 14.7%) is lower than the other cases. The mixing efficiency of case 1 is higher than that of cases 2 ~ 4 on the top of injector. In downstream, the increasing rate of mixing is slower for all cases caused by the supersonic nature of flow.

4. CONCLUSION

It has been found that in case of varying injector distance, strong interaction between the main and injecting flows occurs for short injector distance. For long injector distance both main and injecting flows lose their strength due to viscous action and upstream recirculation. Short injector distance does not have strong recirculation but long injector distances have strong recirculations due to wide space in upstream. Short injector distance increases the mixing efficiency but decreases the flame holding capability. In conclusion, the range of setting the injector is 20~30mm, preferably near 20mm, by which the configuration might act as a good flame holder and become efficient in mixing. For very long distance of injector position (40 mm or more), the configuration reduces both the mixing efficiency and flame holding capability.

REFERENCES

[1] Brown, G. L. and Roshko, A.: On Density Effects and Large Structure in Turbulent Mixing Layer, *J.Fluid Mechanics,* Vol. 64, No. 4, pp.775-816, (1974).

[2] Papamoschou, D. and Roshko, A.: Observation of Supersonic Free Shear Layers, AIAA Paper 86-0162, January (1986).

[3] Ragab, S. A. and Wu, J.L.: Instabilities in the Free Shear Layer Formed by Two Supersonic Streams, AIAA Paper 88-0038, January, 1988.

[4] Hoque, M. R.: A Numerical Study on Mixing and Injection Systems in Supersonic Combustors, M.Sc. Engineering thesis (January, 2004), Department of Mechanical Engineering, BUET, Dhaka, Bangladesh.

[5] Ali, M., Fujwara, T. and Leblance J. E.: “The Effects of Backward-facing step on Mixing and Flame holding in Supersonic Combustor”, Journal of Energy, Heat and Mass Transfer, Vol. 23, 2001, pp.319-338.

[6] Weidner, E.H. and Drummond, J.P.: A Parametric Study of Staged Fuel Injector Configurations for Scramjet Applications, AIAA Paper 81-11468, (1981).

[7] Ali, M. and Islam, A.K.M.S.: Effect of Main flow Inlet Width on Penetration and Mixing of Hydrogen in Scramjet Combustor, Proceedings of the Eighth Asian Congress of Fluid Mechanics, pp. 647–650, December 6-10, Shenzhen, China, (1999).

[8] Tabejamaat, S. J. Y. and Niioka, T.: Numerical Simulation of Secondary Combustion of Hydrogen Injected from Preburner into Supersonic Airflow, AIAA Journal, Vol.35, no.9, September, (1997).